

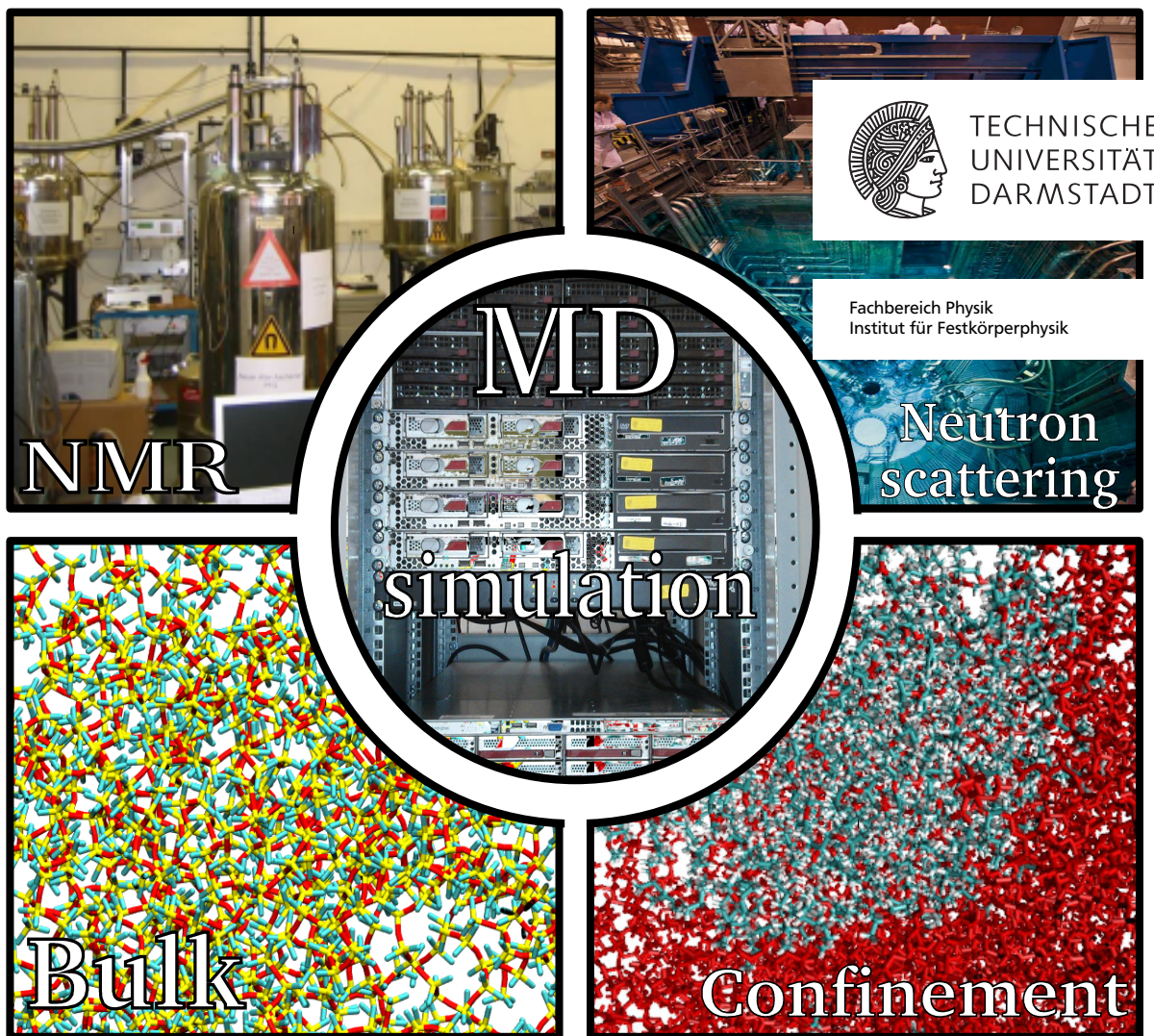
A Molecular Dynamics Simulation Study of Dynamic Processes in Molecular Glass-Forming Liquids

Dynamischer Prozesse in molekularen, glasbildenden Flüssigkeiten studiert mit Hilfe von molekulardynamischen Simulationen

Zur Erlangung des Grades eines Doktors der Naturwissenschaften (Dr. rer. nat.)

genehmigte Dissertation von Patrick Henritzi, M.Sc. aus Frankfurt am Main

Mai 2014 – Darmstadt – D 17



A Molecular Dynamics Simulation Study of Dynamic Processes in Molecular Glass-Forming Liquids

Dynamischer Prozesse in molekularen, glasbildenden Flüssigkeiten studiert mit Hilfe von molekulardynamischen Simulationen

Genehmigte Dissertation von Patrick Henritzi, M.Sc. aus Frankfurt am Main

1. Gutachten: Prof. Dr. Michael Vogel
2. Gutachten: Prof. Dr. Bernd Stühn

Tag der Einreichung: 7.5.2014

Tag der Prüfung: 23.6.2014

Darmstadt – D 17

Erklärung zur Dissertation

Hiermit versichere ich, die vorliegende Dissertation ohne Hilfe Dritter nur mit den angegebenen Quellen und Hilfsmitteln angefertigt zu haben. Alle Stellen, die aus Quellen entnommen wurden, sind als solche kenntlich gemacht. Diese Arbeit hat in gleicher oder ähnlicher Form noch keiner Prüfungsbehörde vorgelegen.

Darmstadt, den 7.5.2014

(Patrick Henritzi)



**“Achtung! Jetzt gibt es nur zwei Möglichkeiten:
Entweder es funktioniert oder es funktioniert nicht.”**

Lukas in "Jim Knopf und Lukas, der Lokomotivführer"

Abstract

In this molecular dynamics simulation study we ascertain the dynamics of the glass transition for polymer melts and ionic liquids. Moreover, we systematically investigate changes of dynamical behavior by varying the molecular weight of the polymers and investigate the interpretation of experimental results, in particular of nuclear magnetic resonance data.

The glass transition occurs in a wide range of systems and upon, e.g., cooling and increasing pressure. Its description is thereby commonly kept universal so that the understanding of the glass transition is closely connected to the understanding of common features for the different systems and control parameters. We find that various scaling approaches, which incorporate different control parameters, e.g., temperature, volume and entropy, describe the dramatic slowdown of dynamics approaching the glass transition for an ionic liquid and four polymer systems. The breakdown of the Stokes-Einstein relation is found for a variety of glass formers and related to other features of the glass transition, e.g., the properties of spatially heterogeneous dynamics. Thereby, the fractional Stokes-Einstein exponent, obtained as a result from the breakdown, is found to be a temperature-independent key feature of glass formers.

The growth of regions with spatially heterogeneous dynamics has inspired the most promising theories of the glass transition. Length scales are thereby a critical component and not clearly defined. Recent studies discuss a description of length scales for confinement systems, where region sizes and confinement sizes intersect. In further analyses we, hence, test the Adam-Gibbs and Random First Order Transition (RFOT) theory via a determination of dynamic and static length scales. For this purpose we study poly(propyleneoxide) in a neutral confinement of four geometries and find length scales, which describe the evolution of bulk dynamics approaching the glass transition. These results and findings in a complementary study of water carried out by F. Klameth [1] support the predictions of the RFOT theory.

Experimental measurements of the diffusion and structural relaxation is a fundamental prerequisite for the study of the glass transition. Recent studies have developed new approaches to study diffusion coefficients and

structural relaxation times by way of nuclear magnetic resonance spectroscopy for wide time ranges and long times. Hence, the key aspects in the interpretation of spin-lattice relaxation times from nuclear magnetic resonance experiments are evaluated from a molecular dynamics simulation perspective. Therein, we find the investigated approaches to determine diffusion coefficients and relaxation times acceptable within sometimes more stringent criteria. Furthermore, we provide a detailed analysis on the origin of deviations between the theoretic framework of polymer dynamics and experimental results. We find that intermolecular contributions, inherent to the method, and fast end groups may result in deviations of the experimental data from theoretical predictions. The simulation approach enables us to identify contributions unaccounted for in common interpretation and theoretic consideration and quantify them.

The present study provides new insight into differences and similarities between a wide range of glass formers, the application of theoretic models of the glass transition, application of confinements to investigate the glass transition, methodical understanding of NMR observables, and deviations from predicted regimes in polymer dynamics.

Zusammenfassung

Die vorliegende Studie untersucht das Phänomen des Glasüberganges anhand von Molekulardynamiksimulationen von Polymeren und einer ionischen Flüssigkeit. Zusätzlich erfolgt eine systematische Untersuchung der Veränderungen der Dynamik durch Veränderung der Kettenlänge, ergänzt durch eine Untersuchung der Interpretationskonventionen experimenteller Daten am Beispiel von magnetischer Kernspinresonanz-Spektroskopie (NMR).

Der Glasübergang tritt bei einer Reihe verschiedener Systeme und unter z.B. Abkühlung oder Erhöhung des Drucks auf. Die Beschreibung des Glasübergang erfolgt daher universell für alle Umstände unter denen er auftritt, weshalb das Verständnis gemeinsamer Eigenschaften der Systeme und der Kontrollparameter von großer Bedeutung ist. Die dramatische Verlangsamung der Dynamik unter Abkühlung der ionischen Flüssigkeit und der vier Polymere bei verschiedenen Temperaturen, Drücken und Kettenlängen lässt sich durch Skalierungen verschiedener Kontrollparameter, z.B. Druck, Volumen und Entropie, gut beschreiben. Dabei wird für eine Reihe von Glasbildnern ein Zusammenbruch der Stokes-Einstein Relation gefunden und mit anderen Eigenschaften des Glasübergangs, z.B. örtlich heterogener Dynamik, in Verbindung gebracht. Als Resultat des Zusammenbruchs finden wir den fraktionalen Stokes-Einstein Exponent, welcher eine temperaturunabhängige Charakteristik des Glasübergangs darstellt.

Aus dem Anwachsen von Regionen örtlich heterogener Dynamik wurden die zurzeit vielversprechendsten Theorien zum Glasübergang abgeleitet. Dabei werden vor allem Längenskalen diskutiert, für die es bisher noch keine eindeutige Definition gibt. Neueste Studien ziehen die Beschreibung von Längenskalen in Confinements in Betracht. Hier können Längenskalen beobachtet werden, wenn die Größe des Confinements und der Regionen vergleichbar werden. Analysen in Confinement Systemen erlauben die Definition dynamischer und statischer Längenskalen, welche zum Test der Adam-Gibbs und Random First Order Transition (RFOT) Theorie herangezogen werden. Dazu untersuchen wir Poly(propylenoxid) (PPO) in einem neutralen Confinement mit vier verschiedenen Geometrien. Es zeigt sich eine gute Beschreibung der Bulk Dynamik des Glasübergangs durch die resultierenden Längenskalen. Diese Resultate und Ergebnisse aus einer

vergleichbaren Studie zur Wasserdynamik von F. Klameth [1] deuten dabei auf eine erfolgreiche Beschreibung der Dynamik des Glasübergangs durch die RFOT Theorie hin.

Die experimentelle Messbarkeit von Eigenschaften wie der Diffusion und der Strukturrelaxation ist Grundlage für das Studium des Glasübergangs. In neuesten Studien wurden neue Ansätze zur Bestimmung des Diffusionskoeffizienten und der Strukturrelaxationszeit mit Hilfe von magnetischer Kernspinresonanz-Spektroskopie entwickelt. Diese bieten die Möglichkeit einen großen Zeitbereich sowie Langzeitverhalten zu untersuchen. Deshalb untersuchen wir einige Grundannahmen und Interpretationskonventionen aus Spin-Gitter Relaxationsexperimenten der magnetischen Kernspinresonanz-Spektroskopie aus Sicht von Molekulardynamiksimulationen. Dabei können die Methoden zur Bestimmung des Diffusionskoeffizienten und der Relaxationszeit im wesentlichen verifiziert werden, wobei teilweise der Geltungsbereich neu gefasst wird. Eine detaillierte Analyse unserer Daten erlaubt weiterhin die Bestimmung der Ursprünge verschiedener Abweichungen zwischen Theorie, Experiment und Simulation. So können die schnellen Endgruppen eines Polymers und die intermolekularen Beiträge, impliziert durch die Methode, Abweichungen hervorufen. Aus den Simulationsdaten können dann die genauen Beiträge und Auswirkungen aus deren Vernachlässigung quantifiziert und eingeordnet werden.

Die vorliegende Studie ergänzt Bisherige durch neue Einsichten bzgl. Unterschieden und Gemeinsamkeiten verschiedener Glasbildner, Anwendung theoretischer Modelle des Glasübergangs, Anwendung von Confinements zur Untersuchung des Glasübergangs, Verständnis der Observablen in der NMR Methodik und Abweichungen zu vorhergesagten Regimen in der Polymerdynamik.

Contents

| | |
|--|-----------|
| 1. Introduction | 11 |
| 2. Current State of Research and Theoretic Principles | 15 |
| 2.1. The Glass Transition | 15 |
| 2.1.1. Phenomenological Description | 15 |
| 2.1.2. Mode-Coupling Theory | 19 |
| 2.1.3. Adam-Gibbs Theory | 20 |
| 2.1.4. Random First Order Transition Theory | 22 |
| 2.1.5. Dynamic Facilitation | 24 |
| 2.1.6. Comparison of Models | 25 |
| 2.2. Polymer Dynamics | 27 |
| 2.2.1. Simple Models | 28 |
| 2.2.2. Rouse Model | 30 |
| 2.2.3. Tube-Reptation Model | 33 |
| 2.2.4. Experimental Findings | 34 |
| 3. Methods | 37 |
| 3.1. Molecular Dynamics Simulations | 37 |
| 3.1.1. Description of the Method | 37 |
| 3.1.2. Force Field Parametrization | 40 |
| 3.1.3. Critical Comments on the Method | 43 |
| 3.2. Systems | 43 |
| 3.2.1. Polymers | 43 |
| 3.2.2. Ionic Liquid | 47 |
| 3.3. Observables | 48 |
| 3.3.1. Pair Correlation Function $g(r)$ | 48 |
| 3.3.2. Incoherent Scattering Function $F_s(q,t)$ | 50 |
| 3.3.3. Translational Diffusion Constant D | 53 |
| 3.3.4. Non-Gaussian Parameter $\alpha_2(t)$ | 54 |
| 3.3.5. Four-Point Density Correlation Function $\chi_4(t)$ | 56 |
| 3.3.6. Dynamic Cluster Analysis $S_w(t)$ | 59 |
| 3.3.7. Dynamic String Analysis $L_w(t)$ | 61 |
| 4. Bulk | 63 |
| 4.1. Volume Scaling | 68 |

| | |
|--|------------|
| 4.2. Adam-Gibbs Scaling | 72 |
| 4.3. Hyperscaling | 76 |
| 4.4. The Breakdown of the Stokes-Einstein Relation | 82 |
| 4.5. Dynamic Facilitation | 89 |
| 4.6. Summary | 93 |
| 5. Confinement Systems | 95 |
| 5.1. Confinement Details | 97 |
| 5.2. Definition of Correlation Lengths | 99 |
| 5.2.1. Dynamic Correlation Length | 100 |
| 5.2.2. Static Correlation Length | 103 |
| 5.3. Description of the Bulk | 108 |
| 5.4. SHD in RP Confinement | 110 |
| 5.5. Summary | 114 |
| 6. Relation to Experimental Methods using the Example of NMR | 115 |
| 6.1. Theoretical Principles of NMR | 117 |
| 6.1.1. ¹ H NMR Observables | 117 |
| 6.1.2. ² H NMR Observables | 121 |
| 6.2. Results | 122 |
| 6.2.1. Interchangeability of Correlation Functions $G^{(m)}(t)$ | 122 |
| 6.2.2. Contributions to $G(t)$ and their Relevance | 125 |
| 6.2.3. Comparison of NMR Correlation Functions to other Methods | 127 |
| 6.2.4. Conventional Spin-Lattice Relaxation Analysis | 128 |
| 6.2.5. Field-Cycling Relaxometry | 133 |
| 6.2.6. Studying Translational Diffusion by Field-Cycling NMR | 136 |
| 6.2.7. Comparison of Computed and Experimental Data | 140 |
| 6.2.8. Dangling Ends Masking Regime II: Protracted Rouse | 144 |
| 6.3. Summary | 146 |
| 7. Summary | 149 |
| A. Potential parameters | 151 |
| A.1. Polymers | 151 |
| A.2. Ionic Liquid | 156 |
| B. Complementary data | 159 |
| B.1. Bulk: Hyperscaling for Various Chain Lengths and Pressures | 159 |
| B.2. Confinement: Hyperscaling of Characteristic SHD Times | 160 |

| | |
|------------------------------|------------|
| Bibliography | 161 |
| List of Abbreviations | 181 |
| List of Symbols | 183 |
| Curriculum Vitae | 187 |
| List of Publications | 188 |
| Acknowledgments | 191 |



1 Introduction

Glasses are a so far not completely understood class of systems. The glass state is not a well-defined phase because the properties of a glass depend on the thermodynamic path which is chosen for vitrification. Thus, understanding the approach to the glass, the glass transition, is of fundamental importance. The phenomenology is long-known, yet only phenomenologically described. As a process leading to a thermodynamically multivalent state, it is like a slippery fish regularly escaping the scientists net in the sea of theoretical considerations. With the nets seemingly getting finer and finer, this study will determine, if our test fish which are polymer melts and an ionic liquid, are caught by some of these state of the art nets.

We are more interested in the glass transition than in the glass state itself because this feature is very important for applications in material science. An advanced understanding of the glass transition would allow one a design of smart materials, which are currently not fully understood and mostly found by a trial and error procedure. Polymers are of great importance in the class of glass formers because they experience complex dynamics, specifically, glass, Rouse, and entanglement dynamics. For each of the known regimes in polymer dynamics theories (Rouse, reptation) have been developed. Additionally, other theories (Mode-Coupling Theory, Adam-Gibbs Theory, Random First Order Transition Theory) deal with the glass transition. Thereby, all theories of the glass transition claim that it is an universal feature for the class of glass formers. This means a wide range of systems is discussed to share some universal features, e.g. molecular glass formers, polymers and charged as well as uncharged molecules. Hence, we will cover the whole range of systems. Specifically, we take a look at different chain lengths of polymers to cover molecular glass formers and polymer melts. Additionally, in contrast to the uncharged polymers we investigate an ionic liquid comprised of two charged components.

The basic observation of the glass transition is the Vogel-Fulcher-Tammann law. The Vogel-Fulcher-Tammann law as a phenomenological description of the glass transition has been associated with cooperativity and heterogeneity of dynamics as well as a growth of length scales. Specifically, these key features of the glass transition can be found in a variety of systems such as bulk systems, thin films and confinements. Thereby, similar length scales

are found in confinements so that they represent an additional possibility to learn about length scales. It is due to the immense importance of the glass transition that a variety of experimental studies has been conducted in glass forming systems. In addition molecular dynamics simulations have become of growing importance in the last two centuries because of their differentiated insights. At first only bead and spring models described polymer melts, yet today chemically realistic models, which reach the onset of reptation dynamics are available. In Fig. 6.1 we see the results of an experimental nuclear magnetic resonance study in comparison to calculations from molecular dynamics simulation data. Both nicely illustrate the transition from molecular glass formers to polymers with the characteristic Rouse and reptation regimes. The indicated power law t^{-1} matches the predicted Rouse dynamics associated with dynamic modes of the model. While Rouse dynamics do not occur for chains shorter than ten monomers, reptation dynamics associated with motion along the contour length are only found for large chains, here, indicated by a second power law with $t^{-0.25}$, which is discussed in Sec. 6.

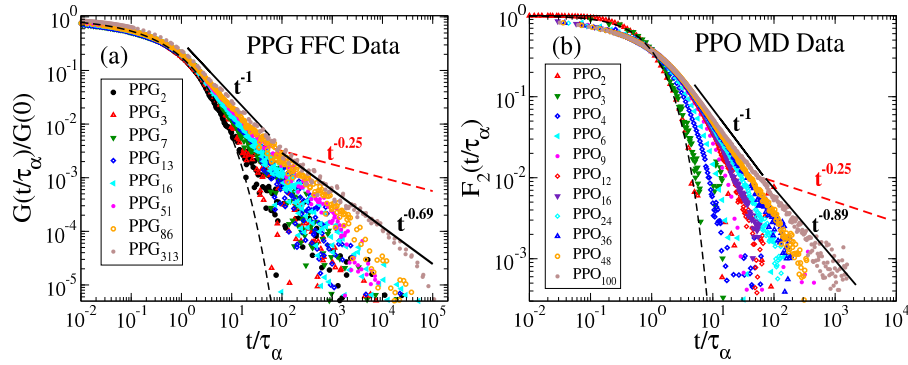


Figure 1.1.: Example for the reproduction of polymer dynamics from molecular dynamics (MD) simulations. In the left panel nuclear magnetic resonance (NMR) measurements and in the right panel MD calculations. Adapted from Bormuth et. al. [2].

In the present study we will characterize dynamic heterogeneities and cooperative motion and their relevance for structural relation. Thereby, consideration of molecular fluids, polymers, charged and uncharged molecules along with variant temperature and pressure gives us the possibility to ascertain the universality of the glass transition. Specifically, through the observations of heterogeneities growing length scales are found. Subsequently, length scales are studied in further detail in confinements. In con-

finements it is found that dynamics change as a function of the distance to the confining wall and length scales can be obtained. Here, MD simulations enable us to conduct simulations in neutral confinements¹, which is impossible in experiments. Analyses of the bulk and the confinements yield growing length scales, which are then compared to theoretic models.

Nuclear magnetic resonance spectroscopy is a powerful experimental tool, which is utilized to investigate diffusion, relaxation, and dynamic regimes. With a very broad time range it is a good tool to study long-time dynamics such as Rouse, reptation, and diffusion. We investigate the information content of the experimental results based on calculations from molecular dynamics simulation data. A lot of assumptions need to be made for the evaluation of the dynamics. With molecular dynamics simulations it is possible to test all these assumptions and contribute improvements to the analysis methods.

On our journey to understand and characterize the glass transition and its universality we will thus take a big tour around all state of the art methods as illustrated in Fig. 1.2. In the bulk we characterize cooperativity and heterogeneities, finding a characteristic growth of length scales. Then we compare these results to length scales obtained in a new approach incorporating “neutral” confinements. In experimental reality it is often challenging to find a method which can measure the relevant quantities in the meaningful range. Hence, we ascertain the expressive strength of NMR, which has lately made some major steps in the determination of diffusion coefficients and structural relaxation.

We will start this study and give an introduction into the relevant theoretical approaches combined with an overview of the state of the current research. Thereby, we will take a closer look at models of the glass transition² and polymer dynamics³. We proceed with an introduction into the basics of molecular dynamics simulations along with the definition of the simulated polymers and the ionic liquid. After that, the chosen force fields are validated and the most important observables used throughout the study are motivated and defined. In the following, we start presenting the results of the present study, which are organized in a modular way. We

¹ i.e., filling and confinement are of the same chemical structure so that the interactions are the same

² Mode-Coupling Theory, Adam-Gibbs, and Random First Order Transition

³ Freely-jointed chain, Rouse model, and reptation model

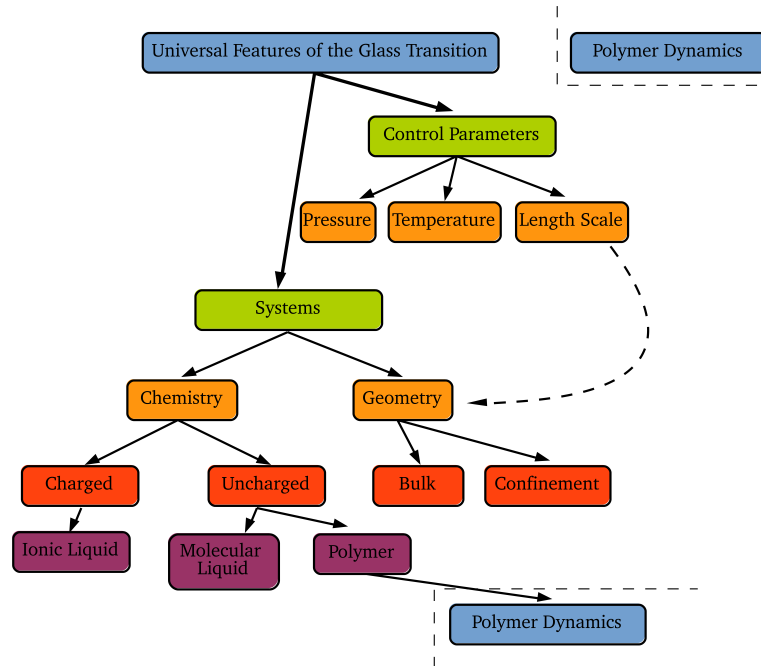


Figure 1.2.: Illustration of the parameters investigated in this work to check the universality of the glass transition.

discuss investigations of bulk dynamics, confinement dynamics and analyses within an experimental framework. Each of these sections contains a separate introduction and summary so that the reader may notice the relevance and context within the chapters. In the section on bulk dynamics we ascertain the relevant control parameters for the glass transition and specifically focus on a temperature-volume scaling, temperature-entropy scaling and the correlation between various characteristic times. Along with these scalings the breakdown of the Stokes-Einstein relation is investigated with respect to its potential as a control parameter. Secondly, we determine different types of length scales in various types of confinements and test their relevance for the bulk dynamics. Furthermore, we introduce the basic ideas of nuclear magnetic resonance and check its assumptions for data analysis. Thereby, we ascertain the chosen analysis procedure through our unique insight into the ensemble and calculate appropriate observables to explain observed deviations between nuclear magnetic resonance and the reptation model. Finally, we provide a conclusion, which summarizes the study and connects the loose ends between the modularized results.

2 Current State of Research and Theoretic Principles

In this chapter we will introduce the relevant theoretical models of the glass transition along with those of polymer dynamics. Furthermore, we will review the relevant literature and name the questions of interest.

2.1 The Glass Transition

The glass transition is a well-known feature of molecular liquids, polymer melts, and ionic liquids. It is characterized in contrast to crystallization by an absence of long range ordering. In this section we will describe the phenomenon itself and give a short overview of the relevant theoretical approaches.

2.1.1 Phenomenological Description

Glasses are amorphous systems of condensed matter that do not crystallize at their melting temperature T_m . The approach of the glass state, e.g., upon cooling, may generally be referred to as the glass transition. Since the actual point of the transition is quite arbitrary defined via a structural relaxation time τ_α of 100s or a viscosity η of 10^{12} Pa·s, the transition is continuous. Thus, all liquid systems below the melting temperature but above the glass transition temperature are either denoted as glassy or supercooled. Specifically, the attribute supercooled is commonly used for systems below the melting temperature T_m which remain in a liquid state. Moreover, supercooled systems do not necessarily continue to build a glass upon cooling but might still reach a crystalline state as in water.

It is well-known that water forms ice crystals when cooled below 273 K, yet it requires seed nuclei for crystallization. Considering pure water, the probability for the formation of seed nuclei is very low so that water may be cooled down to about 233 K preventing a first-order phase transition. The thermodynamic minimum of the system is still defined via the crystalline state, yet the kinetically suppressed formation of seed nuclei leaves the system in a supercooled state. While for water the crystalline state always remains one option, many polymer system consisting of long organic chains are not organized in a macroscopic crystal, because the

entropy forces push the chain in a spherical cluster and crystallization is kinetically blocked.

When the supercooled liquid is cooled further, it eventually reaches a kinetic point T_g , where all particles are trapped in a cage formed by their neighbors and only local motion is possible. This state is then referred to as a glassy state, which has the properties of a solid phase with amorphous order. Depending on the cooling rate, the glass configuration varies in entropy and volume as illustrated in Fig. 2.1. In principle, the glass transition occurs when the time scale of the experiment intersects with the time scale of the system, i.e., if the time scale of the experiment is longer or shorter we see a fluid or glass, respectively. The faster a system is cooled the earlier a certain structure of cages is fixed, whereas a low cooling rate allows for the particles to rearrange and keep their fluid properties. In an imaginary experiment this behavior has motivated W. Kauzmann [3] to postulate the intersection of the infinitesimally slowly-cooled glass with the crystalline state. Moreover, Kauzmann's considerations would allow a glass to reach an entropy lower than the entropy of the crystal. This phenomenon is commonly referred to as the Kauzmann paradox and has motivated various speculations about the physical reality among the scientific community. Furthermore, the proposed intersection has been named in his honor as the Kauzmann temperature T_K .

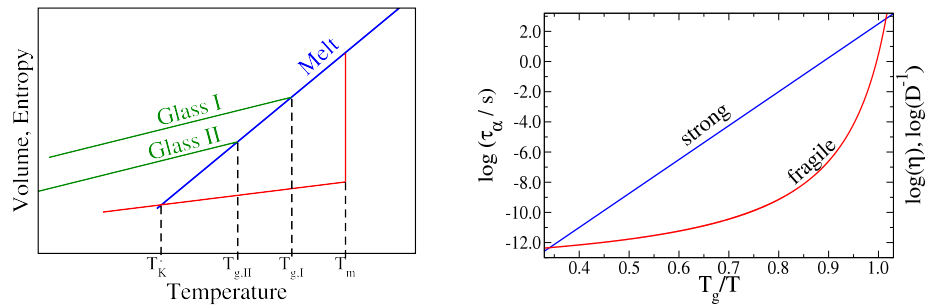


Figure 2.1.: Left panel: Entropy and volume change upon cooling of a glass former. Depending on the cooling rate the system reaches a different characteristic glass configurations. Right panel: Relaxation time τ , viscosity η and inverse diffusion constant D as a function of scaled inverse temperature T_g/T . Upon cooling, a dramatic slowdown of dynamics over many decades is observed. (Details see text)

Along with a change in volume and entropy it is very common to characterize the dynamics of the glass transition. A common definition therein involves the structural relaxation time τ_α ,

$$\tau_\alpha(T_g) = 100 \text{ s.} \quad (2.1)$$

Alternatively, the viscosity or the inverse diffusion coefficients are consulted to define the glass transition. In Fig. 2.1 we illustrate the quantities in an Arrhenius representation over T_g/T , which is a widely accepted form of representation also known as Angell plot [4]. Note that for the logarithmic y-axis and inverse temperature on the x-axis a straight curve already implies a dramatic slowdown of the dynamics in a narrow temperature range. Upon cooling, the slowdown of the three mentioned quantities occurs with a constant slope or with an increasing slope commonly referred to as strong or fragile behaviors.

Structural relaxation is often described as a jump between two local minima of the potential energy surface (PES) overcoming an energy or free energy barrier [5]. Considering such a barrier the relaxation time is given by

$$\tau_\alpha \propto \exp\left(\frac{\Delta F}{k_B T}\right) \quad (2.2)$$

so that strong behavior is associated with a constant activation barrier and fragile behavior is associated with increasing barriers. Phenomenologically, it has thereby proven successful to describe the fragile behavior via

$$\tau_\alpha = \tau_\infty \exp\left(\frac{B}{T - T_0}\right) \quad (2.3)$$

commonly referred to as the Vogel-Fulcher-Tammann (VFT) relation [6–8], which diverges at the Vogel temperature T_0 often found about 50 K below the measured T_g .

The phenomenological findings of the VFT law are often associated with growing cooperatively rearranging regions (CRRs) to explain growing free energy barriers [5, 9–24]. Along with the physical form of these regions their size and therefore a length scale ξ is discussed. Derived from these considerations, critical phenomena [25]

$$\tau_\alpha \propto \xi^z \quad (2.4)$$

with the critical exponent z or free energy related equations [5, 26]

$$\tau_\alpha \propto \exp\left(\frac{\xi^\Psi}{k_B T}\right), \quad (2.5)$$

where Ψ denotes the dimension of a surface or volume, are discussed along with analogies to spin glass models such as the Ising model [27].

Apart from the temperature-dependent change of dynamics, the relaxation itself has a characteristic shape, which is observable in time-correlation functions or mean-squared displacements. In the supercooled state, where particles are on the verge of forming permanent cages, particles feel the existence of the cage only on short time scales and hence perform a structural relaxation at longer times. This movement may be observed as an usually non-exponential decay of auto-correlation functions, e.g., the second Legendre polynomial of the vector auto-correlation function $F_2(t)$. As long as the system has not reached the glass transition temperature the cage's life time is finite and the particles may escape on a time scale τ_α . The decay of any correlation functions is usually preceded by an exponential decay with a temperature-dependent amplitude which reflects the cage size.

The structural relaxation, however, is characteristically stretched with the stretching parameter β ($0 < \beta < 1$) motivating the consideration of a distribution of relaxation times.

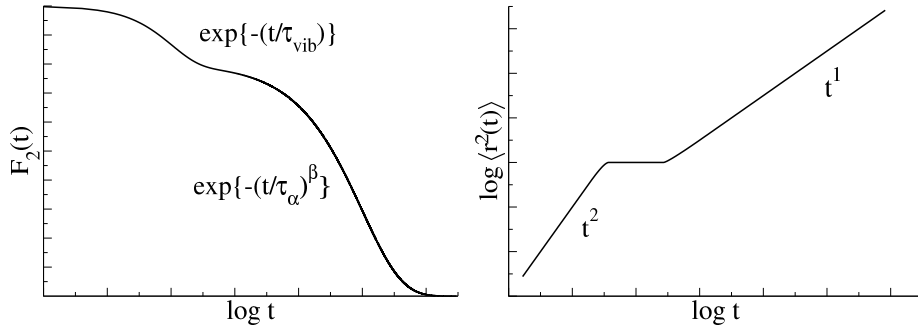


Figure 2.2.: Schematic representations of the auto-correlation function $F_2(t)$ of a supercooled system exhibiting a two-step decay (left panel) and of the mean-squared displacement of a glassy system exhibiting two dynamic regimes and an intermediate plateau (right panel). For more details please refer to the text.

A complementary picture is drawn via the mean-squared particle displacement $\langle r^2(t) \rangle$. Here, we observe a short-time regime of ballistic motion $\langle r^2 \rangle \sim t^2$ marking the free path in the cage and the exploration of the cage. Within the life time of the cage the particle may not leave it so that a plateau is observed. On a long-time scale, where the energy barrier caused by the cage is finally overcome, the particle performs a random walk-like diffusive motion $\langle r^2 \rangle \sim t^1$. Of course, the curves presented here are rather idealized and in real observations the regimes are not necessarily separated so accurately. Furthermore, realistic glass formers often exhibit intermediary, subdiffusive regimes due to the nature of the specific system, e.g., polymers as we will see in the next chapter.

In the subsequent sections we will give a short introduction to the basic concepts of the relevant models of the glass transition widely inspired by a very interesting review by A. Cavagna [28].

2.1.2 Mode-Coupling Theory

The Mode-Coupling Theory (MCT) aims at deriving a set of self-consistent equations for the dynamical correlation function of the density fluctuations [28–30]. The only input used in this set of equations is the static structure in the form of the structure factor $S(q)$. For each q-vector a differential equation may then be derived in a density formalism. For a detailed review of the relevant equations please refer to the reviews [31, 32].

The model yields a bifurcation at a critical density ρ_c even though the structure $S(q)$ is not significantly changed upon cooling. This divergence is discussed as a description for the glass transition because it also includes the correct prediction of a two-step correlation function and a dynamic transition at temperature T_C . Description of the phenomenon via

$$\tau_\alpha \propto \frac{1}{(T - T_C)^\gamma} \quad (2.6)$$

on the other hand, has been proven inaccurate close to T_C [28]. Furthermore, assessment of the glass transition temperature T_g yields values far off, $T_C \gg T_g$, systematically overestimating the transition temperature.

The analytical form of the theory allows to calculate any kind of observables, e.g., scattering functions and non-Gaussian parameters, as long as they may be derived from a density functional. Hence, various studies have

proven that MCT is a powerful tool to describe hard sphere systems [33] well above T_g . Furthermore, the MCT results are often used as a very simple benchmark system, which we will also use in this study to compare it with the realistic, complex systems.

2.1.3 Adam-Gibbs Theory

The Adam-Gibbs (AG) theory [5] has its foundation on the idea of CRRs motivated by the observation of fragility as in Fig. 2.1. The AG theory derives a temperature-entropy dependence of the glass transition and applies a configuration entropy (S_{conf}) to describe the size of the CRRs. S_{conf} has later been connected with the minima of the potential energy surface (PES), which made it accessible to simulation works [21]. Furthermore, the AG theory has been found to describe the glass transition in a variety of different liquids [34–37]. In recent years several simulation works on realistic and model liquids [10–12, 38–40] have found the formation of highly mobile clusters and developed the picture of spatially heterogeneous dynamics (SHD). SHD is discussed to resemble CRRs, yet so far the concrete link is missing. Moreover, it has been found that cluster shapes vary, while their size may characterize S_{conf} [21].

Considering a free energy barrier for a whole region that performs a cooperative relaxation, it is intuitive to assume that the energy barrier is proportional to the number of constituents n

$$\Delta F = n\Delta f, \quad (2.7)$$

where Δf shall refer to the free energy barrier for a single particle. The question to be answered here, is how many regions there are or equivalently how many particles there are in one region. For the AG theory this question is answered by the number of states accessible within the system [28]. The AG theory assumes the different CRRs interact just weakly with each other so that the number of CRRs N/n describes the number of locally stable configurations associated with the configuration entropy S_{conf} . Here, the vibrational part of the configuration is disregarded. An illustration of the configuration entropy as the difference between the entropy of the crystalline state and the glassy/supercooled state is given in Fig. 2.3. Consequently,

$$S_{\text{conf}} \sim \frac{N}{n} \quad (2.8)$$

and

$$n \sim \frac{1}{S_{conf}} \quad (2.9)$$

so that we may describe the relaxation time τ via

$$\tau = \tau_0 \exp\left(\frac{B}{TS_{conf}(T)}\right). \quad (2.10)$$

Here, all single particle interactions have been summed up into the constant B and n was inserted into the free energy barrier in Eq. 2.7 and subsequently into Eq. 2.2. Given

$$\Delta F \sim n \sim \frac{1}{S_{conf}} \sim \xi^d, \quad (2.11)$$

where d denotes the dimension of the system, we have derived a relation between a characteristic length scale and the size of CRRs. In the upcoming chapters we will see this result is debatable.

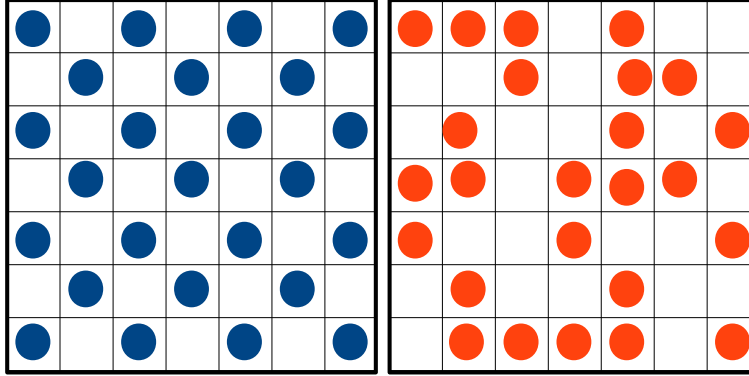


Figure 2.3.: Illustration of the concept of configuration entropy. In the perfectly ordered crystal there is obviously only one configuration available (left), for the disordered or amorphous system however the particles may arrange in many and above all distinguishable configurations. Vibrational contributions need not be included in these considerations because motion about the equilibrium position does not define a new state.

From this result we may also derive the functional form of VFT, which

describes experimental data very well. The thermodynamic relation with the heat capacity yields

$$\frac{dS_{conf}}{dT} \sim \frac{c_p^{LQ} - c_p^{CR}}{T} \equiv \frac{\Delta c_p}{T}. \quad (2.12)$$

Integration ¹ finally gives us

$$\tau = \tau_\infty \exp\left(\frac{T_0}{\Delta c_p T(T - T_0)}\right), \quad (2.13)$$

which resembles the VFT known from Eq. 2.3 for $T \gg T_0$.

2.1.4 Random First Order Transition Theory

The Random First Order Transition (RFOT) theory combines the ideas of Adam-Gibbs' free energy barrier and the density-functional approximation from MCT with the idea of a surface tension between entropic droplets, which are similar to CRRs. Lubchenko et. al. describe RFOT's main idea with the sentence "A supercooled liquid is a mosaic of aperiodic crystals!" or a supercooled liquid is a "mosaic of cooperatively rearranging regions or entropic droplets" [30, p. 249].

RFOT is functionally comparable to MCT well above T_C , where a transition from non-activated to activated dynamics occurs. At T_C however MCT predicts a divergence and all dynamics come to a rest. Here, RFOT allows a second, activated mechanism to take over and continue the relaxation process. Thereby, RFOT solves the problem of MCTs early divergence at higher temperatures.

RFOT was formulated in the late 80s by Kirkpatrick, Thirumalai and Wolynes [41–45]. Its goal was to combine liquids and spin glasses on a theoretical level. RFOT's basic idea is, if we have a system that is in various distinguishable amorphous states, where each state is associated with a CRR, there must be transitional barriers separating the amorphous states. If there were no such barriers, the amorphous states were not distinguishable and therefore equivalent. Furthermore, these amorphous states have

¹ Integral from the transition temperature T_0 to $T \rightarrow \infty$, then expansion of the logarithm for $T \sim T_0$ see. Ref. 28

to be clearly separated via an interface between them. Building an interface is always linked with a certain energy cost so that we may define a region size R dependent free energy cost from the surface

$$\Delta F_{cost} = YR^\theta, \theta < d - 1. \quad (2.14)$$

Here, we have chosen a generalized surface exponent θ in order to take into account that the exact dimensions and characteristics of a CRR are not trivial.

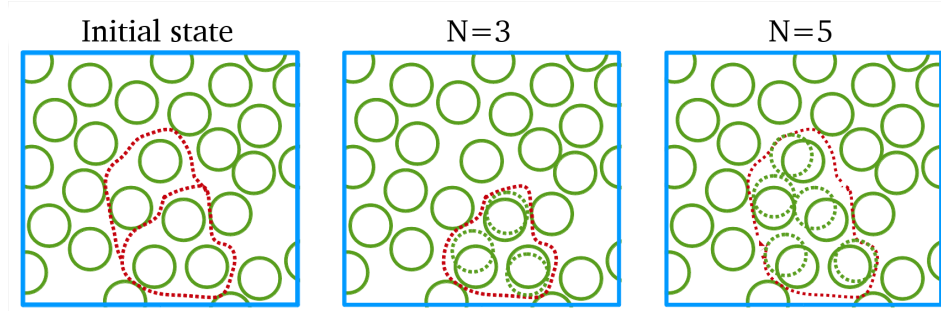


Figure 2.4.: Illustration of entropic droplets consisting of $N=3$ or $N=5$ particles. Depending on the region size N more configurations within the droplet are accessible, while the energy costs of the surface interface increase with N . The equilibrium region size ξ allows cooperative rearrangements impossible for a single particles. Adapted from Ref. 46.

Furthermore, following classic nucleation theory [28] RFOT defines the size of a CRR via a balance between energy cost and gain. Here, AG and RFOT clearly deviate, because AG only considers region sizes in a combinatorial way. Since we are in a liquid state the energy gain cannot be exclusively of energetic nature, but must be entropic as well. The principle of entropy maximization results in a free energy gain

$$\Delta F_{gain} = -TS_{conf}(T)R^d \quad (2.15)$$

with increasing region size along with surface energy cost. The principle is also illustrated in Fig. 2.4. Depending on how many particles are included in one droplet more configurations become available and finally, when the region is big enough, it can equilibrate into a thermally available state of

minimal energy. We define the equilibrium region size ξ , where gain and loss outweigh each other and derive [41]

$$\xi = \left(\frac{Y(T)}{TS_c(T)} \right)^{\frac{1}{d-\theta}}. \quad (2.16)$$

In AG's theory the energy barrier was clearly defined, for RFOT on the other hand we apply once more the concept of classic nucleation theory, where the free energy maximum represents the barrier. The maximum of

$$\Delta F = YR^\theta - TS_{conf}R^d \quad (2.17)$$

varies from ξ in Eq. 2.16 just by a factor $(\theta/d)^{1/(d-\theta)}$ so that the barrier reads

$$\Delta = \frac{Y(T)^{\frac{d}{d-\theta}}}{[TS_{conf}(T)]^{\frac{\theta}{d-\theta}}}. \quad (2.18)$$

When the surface exponent $\theta = d/2$ is chosen it is easy to see that the resulting RFOT relation scales in the same way as the AG relation and therefore also resembles the VFT law.

Finally, we have defined a mosaic of dynamic regions, which are in distinguishable states separated by a surface tension. The regions may perform a local relaxation at the cost of surface energy and explore a wide range of possible configurations. Within the mosaic, the local relaxation times may be up to 5 orders of magnitudes faster than the longest relaxation time [47]. This is possible because each entropic droplet can explore only a limited part of the potential energy surface so that each region explores the available states on different time scales, thereby nicely capturing observed SHD.

2.1.5 Dynamic Facilitation

The concepts of CRR along with SHD have sparked the idea that the question how mobility spreads throughout the system should be addressed. The Dynamic Facilitation (DF) theory [9, 48–51] applies Frederickson-Anderson (FA) model [52] and East Model [53] for Ising spins to glasses. Most importantly, it stands in complete contrast to all the other models we have introduced so far. DF theory sees the glass transition from a strictly dynamic point of view, hence neglecting all ideas of a mean-field theory,

potential energy surface (PES) and the resulting AG, MCT and RFOT theories.

DF promotes an idea originating in the 1960s [52, 54, 55] that a few mobile particles in a deeply supercooled liquid represent islands of mobility, which kinetically will not stay isolated. This means, the probability of relaxation is closely correlated with spatial proximity to a mobile neighbor. Discussion and success of these models are mainly founded on the Frederickson-Anderson (FA) model [52] and East model [53], which perfectly incorporate the idea for spin glasses. Mobility or immobility are here simply coded through the spin states up and down.

Along with the inherent proclamation of spatially heterogeneous dynamics, DF yields optionally strong behavior within FA model

$$\tau \propto e^{(A/T)} \quad (2.19)$$

or fragile-like behavior within the East model

$$\tau \propto e^{(A/(T^2 \ln 2))}. \quad (2.20)$$

The model predicts a growth of the domain sizes with $\sqrt{(\tau_\alpha)}$ [9], where previous studies have found growing domain sizes with other functional dependence [23, 56]. Furthermore, DF predicts the breakdown of the Stokes-Einstein relation [57], which we will also address in the present study.

DF overcame its time of major impact at the beginning of the century. Today RFOT is discussed in a larger context, yet for a sufficient overview we have included it here and also briefly address it in the result section.

2.1.6 Comparison of Models

In the previous sections of this chapter we have discussed four of the most interesting glass transition models presently available.

The Dynamic Facilitation (DF) theory is harshly criticized for its strictly dynamic approach and has been losing ground for the past years. Nevertheless, the rather simple approach captures the main features of the glass transition and simulation works on SiO₂ [23] and a Dzugutov system [56]

could show that an enhanced relaxation in the vicinity of mobile particle actually exists. The significance of these findings regarding the value of DF however remains questionable. In this context, we will also present some examples for our systems.

The temporary success of MCT has mostly passed on to the RFOT theory, which includes the transition from non-activated to activated dynamics making MCT as a comprehensive theory obsolete. Yet, the analytical form of MCT still represents a very nice framework for the calculation of many observables in hard sphere systems and in moderately supercooled liquids, thereby setting benchmarks for other studies [29, 33].

The Adam-Gibbs theory and its rather intuitive picture of activated dynamics has also been overcome by the generalized approach of RFOT. However, AG remains to be the picture scientists most easily think in. Despite many indications that the free energy barrier scales with a reduced surface exponent [28], direct use of configuration entropies also yields a very good description of the evolution of relaxation times [58, 59]. Altogether, difficulties in the definition of dynamic length scales ξ will keep the AG model in the game for a little longer.

We have seen the differences between AG and RFOT in AG's combinatory choice of region sizes, in contrast to RFOT's balance between surface energy cost and entropic energy gain. The resulting length scales yield different temperature scalings

$$\xi_{RFOT} = \alpha \left(\frac{1}{T - T_0} \right)^{\frac{1}{d-\theta}} \quad (2.21)$$

$$\xi_{AG} = \alpha \left(\frac{1}{T - T_0} \right)^{\frac{1}{d}} \quad (2.22)$$

and barrier differences concerning the exponent $\Delta_{AG} \propto n \propto \xi^d$, $\Delta_{RFOT} \propto \xi^\theta Y$. RFOT today represents the best alternative because it includes all the most prominent theoretical ideas and describes the relevant observations. Determination of the exact dimension of the regions and their physical observation, however, remains a formidable task.

At present, strategies to define length scales within supercooled liquids are being widely discussed. Recently, simulation works [58–65] of model

liquids have tackled the task with the implementation of confinements and specifically neutral confinements with equivalent interactions between liquid and solid. Observation of the confinement influences on the liquid is utilized to define length scales, which may or may not be a good observable to test the presented theories. The findings within recent studies are, however, not clear and the modest number of studies and systems investigating the new approaches does not allow a definite conclusion so far.

In this work we will complement previous simulation studies on rather simple systems with our complex polymer, ionic liquid and water systems.² Hence, we provide further indications for the mentioned models and expand the number of investigated systems significantly.

2.2 Polymer Dynamics

Polymers and specifically their dynamics are of high value for the application of smart materials in modern material science. While polymers like other glass formers show a dramatic slowdown of dynamics approaching the glass transition, they also have viscoelastic properties. This means, depending on temperature and time or frequency scale, polymer melts may behave like viscous fluids, elastic polymers or a solid. Engineering these properties via the choice of repeat unit, terminal group and chain length is a formidable task, so far achieved only on a trial and error basis. Of course, the scientific community has also come up with some chain models to describe the difference between molecular glass formers and polymers.

In the following sections, we will introduce the most relevant models for polymer melts. First, we will consider the rather simple models including the freely-jointed chain. Next, the Rouse model [66] is described as one of the most successful models and finally, we present the basic ideas of the tube-reptation model [67], which also applies to very long chains.

Of course, these models have all been described several times by other authors and similarities with the standard literature are both intended and inevitable. In this context, the well-known books on polymer physics by de Gennes [67], Doi and Edwards [68], and Strobl [69] have to be mentioned.

² water data is provided by F. Klameth from our joint publication [1]

2.2.1 Simple Models

Under the term simple models we introduce models which incorporate the fundamental properties of any chain molecule. Here, monomers are substituted by single points of mass or beads neglecting all substructure. In simulations the concept of simplification of chemical substructures is also applied and known as coarse-graining. In this study however simulations of realistic models will be conducted.

Freely-Jointed Chain

In the model of a freely-jointed chain the consecutive beads are jointed via bonds of fixed length. Other than that, no further assumptions are made. For a single bond vector of length b it is clear that it may point in any direction on a sphere of radius b , hence the probability to reside in any state is

$$P(\vec{r}) = \frac{1}{4\pi b^2} \delta(|\vec{r}| - b) \quad (2.23)$$

for any single bond state. Subsequently, the complete chain of length N is then described by

$$P(\{\vec{r}\}) = \prod_i^N P(\vec{r}_i). \quad (2.24)$$

The freely-jointed chain furthermore predicts the structural property of the end-to-end vector

$$\vec{R}_E = \vec{R}_N - \vec{R}_0 = \sum_i^N \vec{r}_i \quad (2.25)$$

which can also be expressed as the sum of all vectors in between. As usual, we consider the ensemble average of the squared end-to-end vector

$$\langle \vec{R}_E^2 \rangle = \sum_i^N \sum_j^N \langle \vec{r}_i \vec{r}_j \rangle \quad (2.26)$$

which yields a very simple result

$$\langle \vec{R}_E^2 \rangle = \sum_i^N \langle \vec{r}_i^2 \rangle = N b^2, \quad (2.27)$$

because the orientations of the bond vectors $\langle \vec{r}_i \vec{r}_j \rangle$ are statistically not correlated for $i \neq j$. This result agrees with predictions from random walk models, since it obviously applies the same assumptions without actually applying a dynamic equation.

In order to incorporate volume exclusions via fixed angles between bonds, the next step is the so-called freely-rotating chain. However, its basic result

$$\langle \vec{R}_E^2 \rangle = Nb^2 \frac{1 + \cos(\theta)}{1 - \cos(\theta)}. \quad (2.28)$$

resembles the freely-jointed chain and the Gaussian chain for $\theta = 90^\circ$ so that we will not discuss it in further detail here.

Kuhn Segments

Kuhn segments enable application of the introduced simple model to real systems. Naturally, assumptions like uncorrelated bond orientations and simplified mass centers are a long way off the experimental reality. The idea of the Kuhn segment is to alter the actual number of monomers and their respective bond lengths so that the assumptions are valid. The method may also be called a coarse-grained model of the initial ideas of one monomer per bead.

First, we define the persistence length l_{ps} of the polymer, as the distance between two beads necessary to lower the orientational correlation significantly

$$\langle \vec{e}(l) \vec{e}(l + \delta l) \rangle = \exp\left(-\frac{\delta l}{l_{ps}}\right), \quad (2.29)$$

where \vec{e} denotes the orientation between two segments within the chain. Specifically, for MD simulations this task is quite simple to accomplish. The bond length between two beads fulfilling the above relation is as an upper limit half the Kuhn length [69]

$$b_K = 2l_{ps} = C_\infty b, \quad (2.30)$$

which is linked to the original bond length b by the parameter C_∞ . This parameter is to be determined for each chain length and polymer so that the models can be tested. Apart from a larger length scale b_K it also yields a reduced number of beads $N_K = N/C_\infty$.

2.2.2 Rouse Model

The Rouse model by P. E. Rouse [66] was published in 1953 to describe polymer dynamics with a simple bead and spring model often also referred to as a necklace model. Studies of polymer melts had shown that the dynamics of these complex fluids cannot be described by the theoretical model of colloidal fluids. While short polymer chains act like a fluid, longer chains have to be described by the Rouse model.

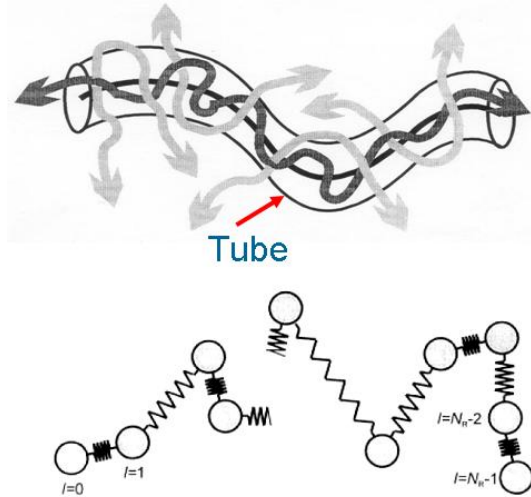


Figure 2.5.: The basic assumptions of the Rouse model and the reptation model in a visual illustration. Extracted from Science Net [70].

The Rouse model again ascribes all mass to beads, but connects them with springs with a spring constant k_R . The spring constant k_R is assumed to be of entropic origin, leading to $k_R = \frac{3k_B T}{b^2}$, where b is the average distance between two beads. In order to include inter-chain interactions in addition to the intra-chain interactions represented by beads and springs, Rouse introduced the chain friction coefficient ζ_R . The friction coefficient is defined as $\zeta_R = k_B T / N D_{cm}$ with the number of Rouse segments N and the center of mass diffusion coefficient D_{cm} . Rouse explicitly neglects excluded volume interactions and hydrodynamic interaction. The next theoretical step is known as the Rouse-Zimm model [66, 71] and would include hydrodynamic interactions. Depending on the system this extension is necessary, for example, for solutions. For a simple melt on the other hand the Rouse model is absolutely sufficient.

Starting with these assumptions one can set up Newton's equations of motion. The force acting on a single bead i depends on the distance to the adjacent beads at \vec{r}_{i-1} , \vec{r}_{i+1} :

$$\vec{F}_i(t) = -k_R[\vec{r}_i(t) - \vec{r}_{i+1}] + k_R[\vec{r}_{i-1}(t) - \vec{r}_i(t)] \quad (2.31)$$

completed by the frictional force $\vec{F}_{\zeta,i}$ and an uncorrelated external Gaussian white noise $g_i(t)$ also known as a Wiener process.

$$\vec{F}_{\zeta,i} = \zeta * \frac{\partial \vec{r}_i(t)}{\partial t}, \quad \langle g_{i,\alpha}(t) g_{j,\beta}(t') \rangle = 2\zeta k_B T \delta_{\alpha\beta} \delta_{ij} \delta(t - t'). \quad (2.32)$$

Altogether, the equation of motion reads

$$m \ddot{\vec{r}}_i = k_R * [\vec{r}_{i+1}(t) - 2\vec{r}_i(t) + \vec{r}_{i-1}(t)] + \vec{g}_n(t) - \zeta_R * \frac{\partial \vec{r}_i(t)}{\partial t}. \quad (2.33)$$

The first part on the right hand side of the equation can, for $N \rightarrow \infty$, be substituted by a differentiation leading to

$$m \ddot{\vec{r}}_i = k_R \frac{d^2 \vec{r}_i(t)}{d^2 x} + \vec{g}_n(t) - \zeta_R * \frac{\partial \vec{r}_i(t)}{\partial t}. \quad (2.34)$$

Here, one needs to see the index i as a spatial coordinate so that the first part of Eq. 2.33 is regarded as the central difference quotient³ of the second derivative in x . This special form of a differential equation is called a Langevin equation and can be solved using Eigenmodes and a transformation into normal coordinates. The analytical solution hence is in normal coordinates and reads

$$\vec{X}_p(t) = \frac{1}{N} \sum_{n=1}^N \cos\left(p\pi \frac{n-1/2}{N}\right) \vec{r}_n(t), \quad (2.35)$$

with the mode p and the number of beads N . The self-correlation function then reads

$$\langle \vec{X}_p(t) \vec{X}_p(0) \rangle = \frac{\langle R^2 \rangle}{8N(N-1) \sin^2\left(\frac{p\pi}{2N}\right)} \exp\left[-\frac{p^2 t}{\tau_R}\right]. \quad (2.36)$$

³ the central difference quotient is given by $f''(x) = \frac{f(x+\Delta x) + f(x-\Delta x) - 2f(x)}{\Delta x^2}$

In order to predict scattering functions or other correlations, we need to perform a back transformation from normal coordinates into real space, which yields time-dependent Cartesian coordinates

$$\vec{r}_n(t) = \vec{X}_0(t) + 2 \sum_{p=1}^N \cos\left(\frac{p\pi n}{N}\right) \vec{X}_p(t). \quad (2.37)$$

The bead mean-squared displacement $\langle r(t)^2 \rangle = \langle (\vec{r}_n(t) - \vec{r}_m(0))^2 \rangle$ is then given as

$$\langle r(t)^2 \rangle = 6D_{cm}t + \frac{4Nb^2}{\pi^2} \sum_{p=1}^N \frac{1}{p^2} \cos^2\left(\frac{p\pi n}{N}\right) \left[1 - \exp\left(-\frac{t}{\tau_p}\right) \right]. \quad (2.38)$$

For long times $t \gg \tau_1$ the first, linear part will dominate the equation and the well-known relation for the diffusive regime

$$\langle r(t)^2 \rangle = 6D_{cm}t \quad (2.39)$$

results. For $t \ll \tau_1$, however, diffusion hardly contributes. Hence, we neglect it and focus on the second part. With a transition from the sum to an integral it can be shown that the second part is

$$\langle r(t)^2 \rangle = \frac{4Nb^2}{\pi^{3/2}} \sqrt{\frac{t}{\tau_1}} \quad (2.40)$$

so that we expect a third regime in the mean-squared displacement succeeding the ballistic regime $\sim t^2$ and preceding the diffusive regime $\sim t^1$.

The Rouse time τ_R and $\tau_p = \tau_R/p^2$ describing the characteristic time of the Rouse modes are given by

$$\tau_R = \frac{\zeta N^2 b^2}{3\pi^2 k_B T}, \quad D_{cm} = k_B T / N\zeta \quad (2.41)$$

yielding

$$\tau_R = \frac{Nb^2}{3\pi^2 D_{cm}}. \quad (2.42)$$

Finally, we see how the Rouse model enables us to predict the dynamics of a polymer chain based only on the basic chain parameters and the diffusion coefficient D or friction coefficient ζ . The Rouse model can also be applied to predict vector auto-correlation functions and scattering functions in the same way [66–69, 72]. Here, we have only shown the basic concept since we will not discuss the model in great detail in this study.

2.2.3 Tube-Reptation Model

In the previous section we have seen how dynamics may change when chain connectivity is added to the simple fluid behavior. For long chains with more than 40 monomers however it was observed [2, 73–80] that another dynamic regime emerges. De Gennes [67] was the first to connect this behavior with inter-chain entanglements, which later on resulted in the revised tube-reptation model formulated by Doi and Edwards in their time-honored book [68].

The concept is based on the emergence of entanglements, which hinder the chains dynamically. We have to consider that neighboring chains may provide entanglements constructing a temporal kind of confinement. On an intermediate time scale the thereby formed tube a chain resides in, is observed as static from the point of view of the chain. It may therefore perform all its short-time relaxations but no chain relaxations and no diffusion. In order to allow these final movements, the chain needs to leave the constructed tube, which it can only do by way of translational motion along its contour length. De Gennes calls this type of movement reptation with reference to the movement of a snake.

Following the idea of a one dimensional diffusion along the contour length, the model applies the boundary condition

$$\vec{R}(s, t + \Delta t) = \vec{R}(s + \Delta s, t), \quad (2.43)$$

which implies that each segment will move through the locations of the other segments in the course of time. The displacement Δs is then like any other displacements in a diffusive regime described by a Gaussian distribution

$$P(\Delta s) = (4\pi D_R \Delta t)^{1/2} \exp\left(-\frac{\Delta s^2}{4D_R \Delta t}\right) \quad (2.44)$$

where the basic assumptions of a random walk are applied

$$\langle \Delta s \rangle = 0; \quad \langle \Delta s(t)^2 \rangle = 2D_R t \quad (2.45)$$

and D_R denotes the reptation diffusion coefficient in one dimension, not to be confused with the final diffusion coefficient D .

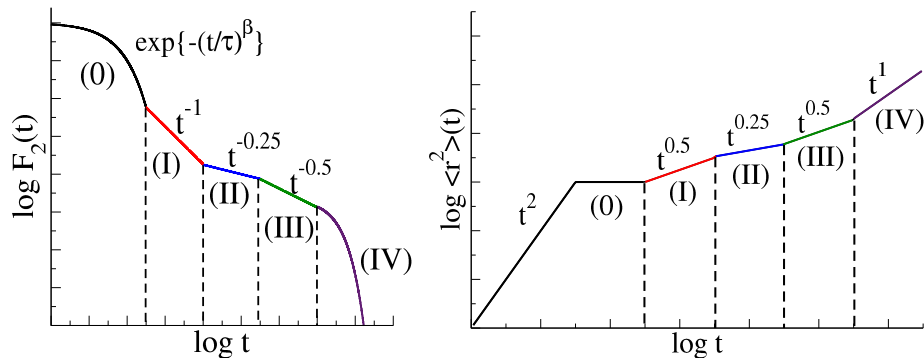


Figure 2.6.: Orientational autocorrelation function $F_2(t)$ (left) and mean-squared displacement (MSD) (right) for the tube-reptation model and its five regimes. Details see text.

Without further proof we present the results of this concept in Fig. 2.6, showing that the model predicts two dynamic regimes we had not found in the Rouse model, while still incorporating the previous ones.

On small length scales, segments may perform a stretched exponential decay often denoted as glassy (regime 0). The vibrational relaxation is not visible anymore in $F_2(t)$, because of the logarithmic scale. Here, it is not of specific interest and hence incorporated into regime 0. Regime 1 is the Rouse regime as we have found it in the previous section. Regime II is called the constrained Rouse regime, where the Rouse dynamics are affected by the existence of the tube. On even longer time scales in regime III only the one-dimensional diffusion along the contour length of the chain contributes, which furthermore hinders the relaxation. Finally, when the chain has left the tube, normal diffusion occurs and the correlation function exhibits its final exponential decay.

2.2.4 Experimental Findings

The Rouse model has been derived [81] and tested [2, 81, 82] for a variety of experimental observables⁴ [81–83]. In moderate temperature scenarios it was found that the model describes the experimental results quite well, whereas for high pressures and low temperatures deviations due to extreme packing density occur [84–86]. Especially, in MD simulations, where each step of the derivation can be tested, the Rouse model was extensively

⁴ nuclear magnetic resonance (NMR), neutron scattering (NS), Dielectric Spectroscopy (DS)

studied, yielding deviations specifically for very small chains [87]. Here, the assumptions of uncorrelated beads is often not given any more so that the model must fail. Various studies have reported findings of reduced Rouse exponents in the MSD of regime I. The most recent development in Rouse theory is therefore a modification, which includes hydrodynamic and viscoelastic effects in the model [88]. The modification yields a reduced exponent but is not considered in the present work.

Entanglement dynamics are a somewhat shy phenomenon, because they do not appear as prominently as Rouse dynamics. While the latter are often and clearly reported with the expected slope, entanglement dynamics are often protracted [77, 78], i.e., a slope ε between the predicted slopes for entanglement and the Rouse⁵ is observed $\varepsilon_I < \varepsilon < \varepsilon_{II}$ [2, 73–79]. It is a widely discussed, prevailing question why the entanglement regimes are hardly observed. Most studies, however, do not question the model itself but its experimentally accessible time and frequency ranges.

In the present study, in Sec. 6, we will contribute the first fully atomistic MD simulations, which exhibit entanglement dynamics [2] and provide a detailed comparison of MD data with experimental data from NMR [89]. We will not provide further detailed analyses of the Rouse model, as it has been done in the preceding PhD thesis by A. Bormuth in 2012 [87].

⁵ With Rouse regime I and constrained Rouse regime II.



3 Methods

This chapter gives an introduction to the method of MD simulations and contains all relevant specifications of the simulated systems. Additionally, we describe those observables which are of relevance throughout the complete study.

3.1 Molecular Dynamics Simulations

Molecular dynamics (MD) simulations are a versatile tool applied to a variety of different systems. With its incredibly detailed data on atom positions and velocities, it enables us to calculate any observable with origins in atomic particle placement. Even though MD simulations do not capture all known physical interactions, they give us a very good picture of dynamics on an atomic level.

In the following we will introduce the fundamental ideas of MD simulations and the force fields used in this particular study.

3.1.1 Description of the Method

MD simulations solve the Newtonian equation of motion for a classical many-body system. For a system of more than three particles this is not possible in a strictly analytical form so that a numerical approach is necessary. We hence assume all relevant interaction may be parameterized through a classical, two-body potential. Depending on the ensemble choice (NVT, NVE, NpT) we must only add boundary conditions for the finite size of the system and a coupling to external pressure and temperature or energy.

As already mentioned above, the basic idea of a molecular dynamics simulation is solving the Newtonian equations of motion. In their simplest description this refers to equations evaluating every atom's current position and speed. Additionally resulting from the atom position every atom will feel a different force or acceleration due to the effects taken into account. For the description of the algorithm we do not need to describe

the forces in detail at this point, because all forces can be described by the potential that creates the force.

$$\vec{F}_i(t) = m_i \frac{\partial^2 \vec{r}_i}{\partial t^2} = -\vec{\nabla}_i V_i \quad (3.1)$$

As an integrator we apply the leapfrog algorithm [90]. The algorithm calculates spatial coordinates for integer time steps, whereas velocities are determined for the exact time between two spatial steps, i.e., half-integer values, illustrated in Fig. 3.1.

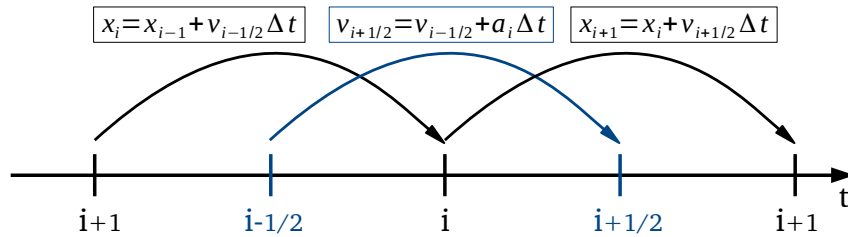


Figure 3.1.: Illustration of the leapfrog algorithm and the relevant equations.

As a barostat we utilized the Parrinello-Rahman algorithm [91, 92], which does not simply rescale the box size to alter the pressure, but may also change the shape of the box slightly. It has been shown that isotropic control of the volume does not allow good equilibration of a system. Therefore, often simple algorithms like the Berendsen [93] barostat are only used far from equilibrium. For the coupling to a heat bath we also apply a sophisticated algorithm, which is specifically designed to complement the chosen barostat. The Nosé-Hoover thermostat [94, 95] introduces an additional degree of freedom into the Hamiltonian so that it may rescale coordinates and time. The scaling parameter is then altered, to ensure the statistic distribution of velocities resembles a Boltzmann distribution of the desired temperature. The simpler algorithms here again simply scale all velocities by a certain factor, which does not describe the ensemble sufficiently.

Finally, the Particle-Mesh Ewald (PME) algorithm [96, 97] allows us to handle long-range Coulomb interactions due to the boundary conditions.

| Algorithm | GROMACS |
|---------------------|------------------------------|
| Integrator | leapfrog algorithm [90] |
| Barostat | Parinello-Rahman [91, 92] |
| Thermostat | Nosé-Hoover [94, 95] |
| Bond constrains | Harmonic |
| Periodic boundaries | Particle Mesh Ewald [96, 97] |

Table 3.1.: Summary of the relevant algorithms applied in the study.

Of course, particles interact with each other over periodic boundary conditions at the limits of the simulation box. For Coulomb interactions these interactions would result in an enormous amount of interaction partners. Thus, for the classic Coulomb interactions a cut-off is applied and the remaining interactions outside the cut-off are handled in Fourier space via an Ewald summation.

A more detailed description of all algorithms would exceed the size of this work, hence we ask the reader to consult the given references in the summary (see Tab. 3.1).

We conducted our simulation with a wide-spread simulation package called GROMACS [98–101], which is favored by a large portion of the scientific community due to its good documentation and relatively easy usage. The GROMACS project is constantly upgraded and there is a large number of developers all over the globe working on improvements. Features specifically valued for starters are preset packages of systems and forcefields the user can obtain directly from the developers. Regarding computing power we are especially interested in the parallelization capabilities of GROMACS, that are well implemented and tested.

For all systems presented in this work we have chosen the NVT ensemble with a constant number of particles in a constant box size coupled to a temperature bath of temperature T . In order to obtain the optimal properties for these “production” runs we have performed an equilibration in a NpT ensemble, where the box volume is variant to obtain the correct pressure. The equilibration was performed for at least 5 ns up to several hundred ns, where the structural relaxation time τ_α is very long for low temperatures. From the equilibrated NpT run we have chosen a mean box size and incorporated it into the NVT simulation so that the correct pressure is achieved.

3.1.2 Force Field Parametrization

The force field of the MD simulation is the most important and difficult part of the whole work. Besides the obvious problem of creating the force field, the question which effects should be taken into account must be answered. For a molecular system a force field in principle incorporates non-bonded interactions like Coulomb and van der Waals and bonded interactions like bonds, bends and torsions so that the potential reads

$$V^{TOT}(\{\vec{r}\}) = V^{NB}(\{\vec{r}\}) + \sum_{ij} V^{BOND}(r_{ij}) + \sum_{ijk} V^{BEND}(\Theta_{ijk}) + \sum_{ijkl} V^{TORS}(\phi_{ijkl}), \quad (3.2)$$

where i, j, k, l refer to different atoms and Θ, ϕ refer to bend and torsional angles. In the following we will give a short overview of underlying interactions within this equation.

Non-Bonded Interactions

Starting from one of the most basic systems known to the MD community, we introduce a repulsive-core potential for the Pauli principle complemented by an attractive potential representing van der Waals forces. This form of potential is essential for any of the systems, molecular and atomic. It has become a standard procedure to characterize these interactions by a Lennard-Jones (LJ) [102] or Buckingham (BK) [103] potential written as follows

$$V^{LJ}(\vec{r}) = \sum_{i,j} \epsilon_{\alpha\beta} \left[\left(\frac{r_{min,\alpha,\beta}}{r_{ij}} \right)^{12} - 2 \left(\frac{r_{min,\alpha,\beta}}{r_{ij}} \right)^6 \right] \quad (3.3)$$

$$V^{BK}(\vec{r}) = \sum_{i,j} A_{\alpha\beta} \exp(-B_{\alpha\beta} r_{ij}) - \frac{C_{\alpha\beta}}{r_{ij}^6} + \frac{q_{\alpha} q_{\beta}}{4\pi\epsilon_0 r_{ij}}. \quad (3.4)$$

Here, we have neglected the Coulomb term in the BK formula just for aesthetic reasons. In Fig. 3.2 we see the basic shape of the two potentials with their characteristic repulsive short-range interaction and attractive interaction at an intermediate distance. The BK potential contains the possibility to become attractive and non-physical if the barrier chosen is too small or the temperature too high an unwanted attractive force at sort distances could influence the system.

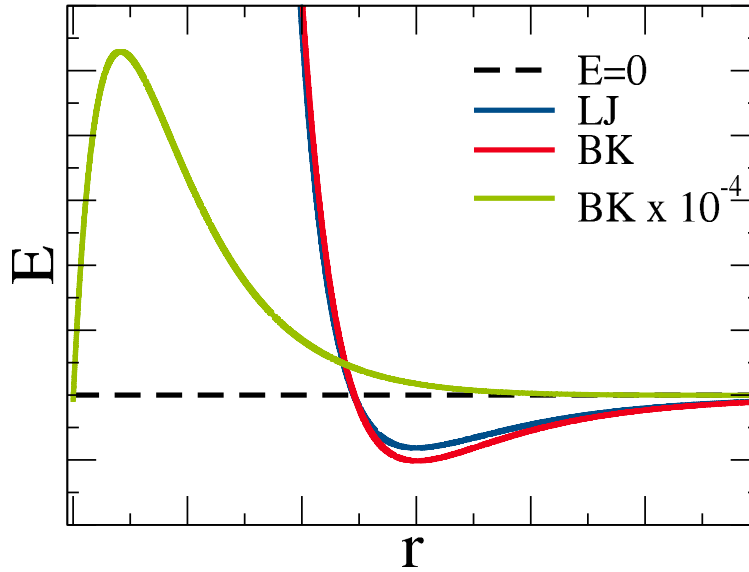


Figure 3.2.: Non-bonded potentials by way of example. Both LJ and BK yield a comparable form about the resting point, whereas at short times LJ diverges to $+\infty$ and BK has a maximum and diverges to $-\infty$.

Bonded Interactions

The bonded potentials in equation 3.2 are defined as:

$$V^{BOND}(r_{ij}) = \sum_{n=2}^4 k_{\alpha\beta}^{BOND}(n)(r_{ij} - r_{\alpha\beta}^0)^n \quad (3.5)$$

$$V^{BEND}(\theta_{ijk}) = \sum_{n=2}^4 k_{\alpha\beta\gamma}^{BEND}(n)(\theta_{ijk} - \theta_{ijk}^0)^n \quad (3.6)$$

$$V^{TORS}(\phi_{ijkl}) = -\frac{1}{2} \sum_n k_{\alpha\beta\gamma\delta}^{TORS}(n)[1 + \cos(n\phi_{ijkl})] \quad (3.7)$$

The bond potential only contributes in case of deviation from the desired mean bond distance $r_{\alpha\beta}^0$, which may differ for any combination of atom types α, β . Following the same logic the equilibrium bend angle between atom type α, β and γ is $\theta_{\alpha\beta\gamma}^0$. The angle ϕ_{ijkl} describes the periodicity of the torsional barrier. For the present study bonds and bends are well defined taking into account only the first, harmonic part of the sum. Definition of the torsional barrier on the other hand needs up to six summands.

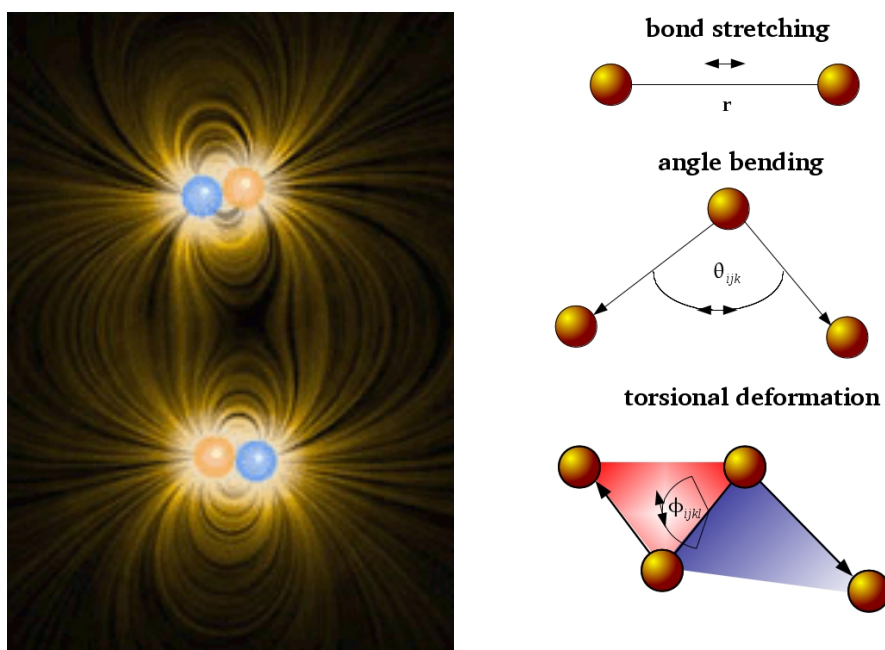


Figure 3.3.: Illustration of an electric field adapted from [104] (left) and bonded interactions (right).

In Fig. 3.3 we illustrate the three bonded interactions. The detailed parameters can be found in the original literature PDMS [105], PB [106], PPO [107], PEO [108], IL [109–112], water [113, 114] and are also given in Appendix A.

Simplifications: United Atom - Explicit Atom

The application of MD simulations is often hindered by finite computing power, which yields only about 2-10 ns of trajectory per day. When long times or big structures such as proteins or even viruses are simulated, a fully-atomistic, Explicit-Atom (EA) simulation is not possible. Here, a coarse-graining approach is chosen so to reduce the number of interacting particles. Groups of atoms, e.g., CH_3 and sometimes even whole amino acids are then comprised to a single particle, which yields a so-called United-Atom (UA) model.

For the present study the presented PB and PDMS systems are such UA systems, i.e., the CH_3 groups in PDMS are represented by a single atom CU and the CH and CH_2 groups in PB are also replaced by dummy atoms (see

Fig. 3.4). While technically the systems, hence, are not fully-atomistic we still denote them as chemically realistic in contrast to real coarse-grained models with much bigger UA structures.

3.1.3 Critical Comments on the Method

We have seen that MD simulations are a sophisticated method to calculate the atomic trajectory of many-body systems including several interactions. Unfortunately, MD simulations never include all interactions, because their framework does not handle quantum mechanic principles. Conclusively, neither chemical reactions nor other electronic features are reproduced. The finite size of any simulation may yield non-physical results due to errors induced via the boundary conditions. The limited time frame accessible, within 1 fs - 1 μ s , and the limited number of particles <100,000 restricts the method to systems of intermediate complexity and to local observables.

For the connection between theory and experiment MD simulations contribute a valuable lesson about the numerical solution of many-body systems. The method enables testing of theoretical models along with experimental assumptions on an atomic level and contributes a sophisticated view on otherwise hidden details.

3.2 Systems

This section gives a short introduction to the polymers and the ionic liquid addressed in this work. It shall mainly show the relevant differences between the systems, the exact parameters can be found in the Appendix.

3.2.1 Polymers

Poly(dimethylsiloxane) (PDMS) is a polymer consisting of silicon, oxygen and methyl groups. It has a wide range of applications reaching from an additive in the food industry up to application in contact lenses. PDMS is known to be loosely packed, which is why it is also used in gas separation processes. The polymer generally does not dissolve and forms a glass at approximately 146 K [115, 116] depending on the molecular weight and decomposes at approximately 500 K [117]. PDMS as a glass former does not have a freezing temperature and decomposes before reaching its boiling point. As an industrial product it can also be found under the names

dimethicone and E900 [118].

Poly(butadiene) (PB) is a synthetic rubber that is polymerized by the connection of 1,3 butadiene and subsequently, builds a copolymer consisting of 1,4-cis 1,4-trans and 1,2-vinyl monomers. It is used in the manufacture of tires and many other industrial products. The usage in blends (mixtures with other polymers) is even more common than its pure composition. Regarding its structure, it is quite simple as it only consists of carbon and hydrogen, which leads to a small number of different interactions. Hence, in simulations it allows very good performance benchmarks.

Poly(propyleneoxide) (PPO) is also called poly(propylene glycol). The polymerization is often started with the glycol polymer, while it differs in its end group from the oxide which ends in a CH_3 group in contrast to the glycol ending in a hydroxy group. Some sources also distinguish the two terms regarding molecular weight. The polymer is referred to as an oxide, when the molecular mass is high enough so end groups hardly matter anymore. PPO is liquid at room temperature, flammable when heated and dissolves in water.

Poly(ethyleneoxide) (PEO) is also known as poly(ethylene glycol) or poly(oxyethylene) and under the trademark Carbowax [120]. Usage of the terms is again linked to molecular weight though there are no principal rules on that. PEO is mainly used as a medical substance, i.e., in laxatives, but can also be found in a variety of other products.

Structural differences

There are two basic structural differences between the polymers, the **backbone** and the **side groups**. In Fig. 3.4 we present an illustration of the four systems and their variations in the UA model and Tab. 3.2 shows the polymers structure formulas in direct comparison. Note that the PB system cannot sufficiently be described in this form as it consists of three different monomer configurations 40% 1,4-cis, 50% 1,4-trans and 10% 1,2-vinyl adapted from Smith et. al. [106, 121].

Details for the force field parameters of all systems can be found in Appendix A.

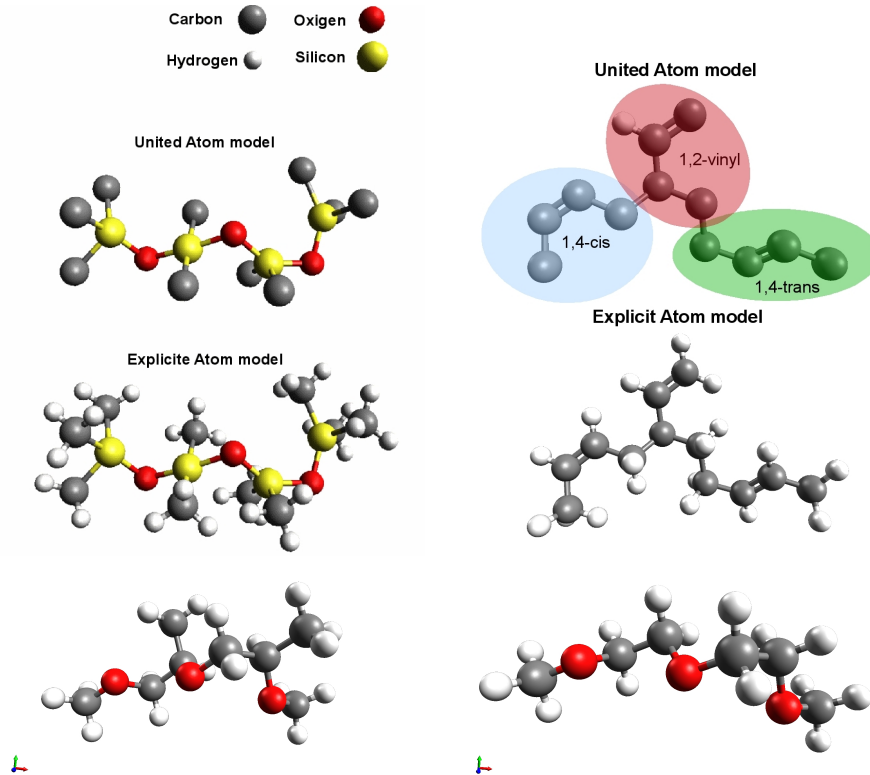


Figure 3.4.: UA and EA model for PDMS₂ and PB₃, along with EA models of PPO₂ and PEO₂ created with AVOGADRO [119]

| Polymer | backbone | sidegroup | structure formula |
|---------|--------------|---------------------|---|
| PDMS | Si-O-Si-O-Si | CH ₃ | Si(CH ₃) ₃ -O-[Si(CH ₃) ₂ -O] _N -Si(CH ₃) ₃ |
| PB | C-C-C-C-C | H, vinyl | H-[CH ₂ -CH=CH-CH ₂] _N -H |
| PPO | C-C-O-C-C-O | CH ₃ , H | CH ₃ -O-[CH ₂ -CH(CH ₃)-O] _N -CH ₃ |
| PEO | C-C-O-C-C-O | H | CH ₃ -O-[CH ₂ -CH ₂ -O] _N -CH ₃ |

Table 3.2.: Structural differences of the melts, chain length indicated by N, later used as in PPO_N

Parameter Range

For this study we have performed MD simulations for various chain lengths, temperatures, and pressures along with some carefully chosen confinements. Details on the confinements can be found in the respective Sec. 5.

The most extensive amount of data was simulated for PPO, where A. Bor-muth had already performed many simulation. Here, chain lengths starting with the dimer up to 100 monomers are available [87] for a temperature range from 150 K to 800 K, varying on the specific chain length. Additionally, the pressure for some systems has been varied in a range from 1 bar up to 10,000 bar.

Specifically for this work, the PPO data is complemented by PEO for $N=12, 50, 150, PB_{27}$ and PB_{276} in the same temperature and pressure range. In the following we will denote only the name of the presented systems along with the respective temperature and skip the pressure unless it differs from 1 bar.

For PDMS we have analyzed old data from a master's thesis [84] with chain length between 19 and 150 monomers, with sparse temperature and pressure variation. Unfortunately, this system could not be complemented with further simulations, because it was performed with an outdated simulation package [122] no longer available.

| System | Monomers N | Molecular weight M_W | No. of molecules |
|--------------------|------------|------------------------|------------------|
| PPO ₂ | 2 | 104 | 200 |
| PPO ₃ | 3 | 162 | 1024 |
| PPO ₉ | 9 | 511 | 48 |
| PPO ₃₆ | 36 | 2079 | 12 |
| PPO ₁₀₀ | 100 | 5796 | 4 |
| PEO ₁₂ | 12 | 530 | 32 |
| PEO ₅₀ | 50 | 2205 | 18 |
| PEO ₁₅₀ | 100 | 6610 | 8 |
| PB ₂₈ | 28 | 1563 | 40 |
| PB ₂₈₅ | 285 | 15630 | 18 |
| PDMS ₁₉ | 19 | 1574 | 80 |
| IL | - | - | 2x256 |

Table 3.3.: Overview of the system and their sizes.

We have summarized all available systems and their size in Tab. 3.3, where the ionic liquid (IL) system is indicated differently because we have not studied variant molecular weights here and it is the only system consisting of two components of equal number.

3.2.2 Ionic Liquid

The ionic liquid simulations in this study are conducted for 1-Butyl-3-methylimidazolium hexafluorophosphate (bmimPF₆) and were set up in the context of a Bachelor's thesis by N. Müller [123]. The ionic liquids (ILs) are of particular interest to the scientific community at the moment, because their application in batteries and solar cells is quite promising. They are low-melting salts of organic origin. At room temperature they are already fluid and due to their high polarizability good solvents. Upon cooling many IL systems exhibit a glass transition to a solid amorphous structure. The simulations performed here will complement the other systems specifically for the investigation of the glass transition, because we do not intend to describe any specific system, but rather the glass transition at its core.

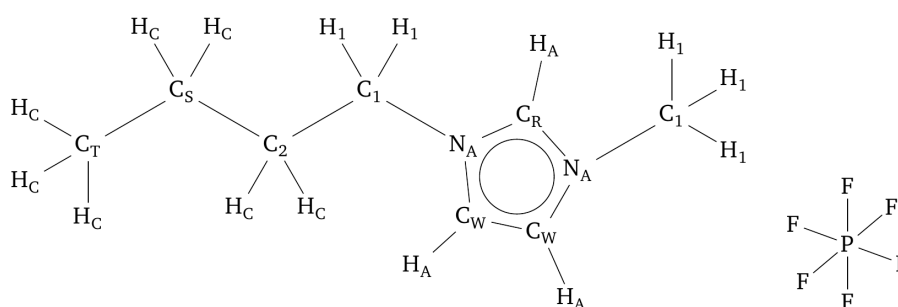


Figure 3.5.: Illustration of the structural properties of bmim-PF₆. The cation bmim is positively charged with the charge center at the left N_A atom and the anion PF₆ is negatively charged at its center.

For this purpose the simulations were conducted in a temperature range between 400 K and 200 K at atmospheric pressure. In our evaluation we will focus on three specific atoms in the IL system. When referring to the anion we evaluate the position of the phosphor atom. For the cation we distinguish two characteristic positions, we will denote a cation chain and cation ring corresponding to the carbon atoms CS and CR in Fig. 3.5.

The detailed force field is given in Refs. 109–112 and in Appendix A.

3.3 Observables

In contrast to the theory chapter this section shall give an overview of the relevant observables, which we have calculated as a characterization of the glass transition in glass forming liquids. In chapters 5 and 6 we will introduce and calculate rather specialized observables for the task at hand, whereas this section gives an overview of those observables which are relevant for the whole study.

Before we start the dynamic analysis we need to define some characteristic distances via the pair-correlation function $g(r)$. We will then start characterizing the general dynamics of our systems via the translational relaxation time τ_α extracted from the incoherent scattering function $F_s(q, t)$ and the translational diffusion coefficient D from the mean-squared displacement (MSD). Furthermore, we define four quantities to measure the nature of these dynamics, the non-Gaussian parameter $\alpha_2(t)$, 4-point density correlation function $\chi_4(t)$, dynamic cluster size $S_w(t)$ and dynamic string length $L_w(t)$.

3.3.1 Pair Correlation Function $g(r)$

Characteristic for the studied glassy systems is, besides the mentioned dramatic slowdown of dynamics, that they do not crystallize within the commonly available time frame. Thereby, glassy systems still exhibit a short-range order, which reaches about two to four neighbor distances. Naturally, these first and second neighbor shells represent a characteristic jump length in a picture of activated dynamics. Thus, it is of great importance to take potential structural differences of the systems into account.

We therefore define the pair correlation function¹

$$g(\vec{r}) = \frac{\langle \rho(\vec{r})\rho(\vec{r}_0) \rangle}{\tilde{\rho}}. \quad (3.8)$$

Here, $\tilde{\rho}$ refers to the average particle density and $\rho(\vec{r})$ to the local density at \vec{r} . For isotropic systems such as those in the present study the function may be written as a function of the scalar distance between the particles

$$g(\vec{r}) = g(r). \quad (3.9)$$

¹ sometimes referred to as radial pair-distribution function

The function determines the local particle density normalized to the average density with respect to the increasing spherical surface upon increasing distances r . It may be interpreted as the probability to find an atom in the distance r around any analyzed atom with respect to random structure.

For this study the pair correlation function $g(r)$ will always be evaluated for a specific species of atoms within the systems. Thereby, it is important to note that for molecular systems, such as the present, two contributions to the function are distinguished. Atoms within the same molecule contribute to an intramolecular structure, whereas atoms residing in other molecules contribute to the intermolecular structure evident also in atomic liquids.

In this study we will make an effort to compare the calculated data to experimental and simulation work, which mostly discusses intermolecular contributions². For the definition of relevant length scales, hence, only intermolecular contributions are considered.

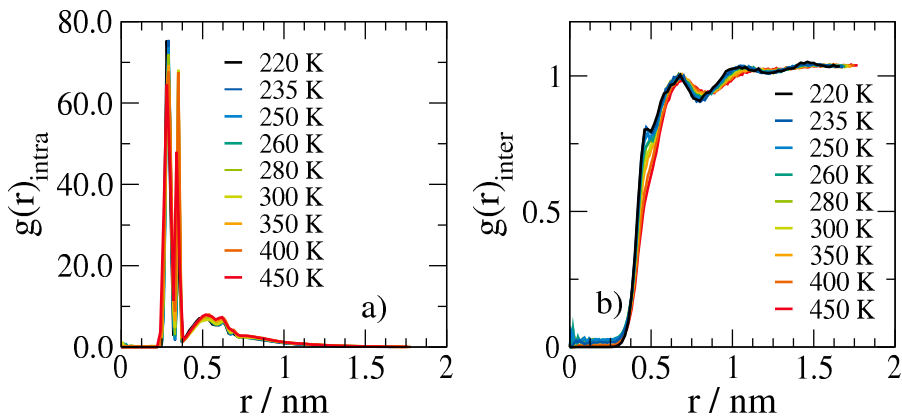


Figure 3.6.: Exemplary pair-correlation function $g(r)$ for oxygen atoms of PPO_9 , (a) intramolecular contributions (b) intermolecular contributions.

When we calculate the different kind of observables the length scales assumed are often referring to the intermolecular $g(r)$ as it is displayed for an exemplary system in Fig. 3.6. We have extracted all next neighbor distances for the different systems at a temperature of 450 K and ensured none of the systems experience a phase transition. In Fig. 3.6 the in-

² Specifically, for the atomic systems in simulations where no intramolecular contributions are defined.

tramolecular as well as intermolecular neighbor shells are not changed significantly within the considered temperature range, which allows us to assume constant characteristic length scales throughout the studied temperature range. The first, very high peaks in $g_{intra}(r)$ refer to the next neighbor atoms along the chain³. Further neighbors after that are found in a variety of distances due to the multitude of possible configurations. For the intermolecular part the primary and secondary neighbor positions are visible, while thereafter typical for an amorphous structure uniform distribution is found.

3.3.2 Incoherent Scattering Function $F_s(\mathbf{q},t)$

Scattering functions describe the change of the wave function of incoming projectiles to the new wave functions of the ejectile. They are a widely utilized method to investigate structural and dynamic properties from molecular to subatomic length scales.

Depending on the chosen projectile the cross section of the different nuclei may be of different value so that each atom species contributes according to its interaction with the projectile. For our simulations we may only apply projectiles with interactions governed by density, where the projectile is a particle mostly interacting through nuclear forces. Would the projectile be a charged particle such as a proton or electron, cross sections would reflect the electron density and interactions would be dominated by Coulomb interactions.

The here proposed calculated observables for incoherent and coherent scattering functions, may thus best be compared to neutron scattering experiments. More concretely, neutron scattering at, e.g., protons, corresponds to an incoherent experiment and at, e.g., deuterons corresponds to a coherent experiment. Of course, both probes yield both contributions yet the specific cross sections result in a dominance of one or the other. In order to simplify the formula work we will not discuss cross sections here and analyze a characteristic atom type for the specific molecules. For the polymers this will be the oxygen or carbon central in each monomer.

In scattering theory [69, 124] the resulting wave function may be de-

³ two peaks for the cis and trans configuration along the chain

scribed as a superposition of waves scattered at different scattering centers i at positions \vec{r}_i

$$C(\vec{q}, t) = \sum_{i=1}^N \exp(-\vec{q}\vec{r}_i t), \quad (3.10)$$

where t refers to a time interval in which the function is evaluated. The scattering function is then described as the time correlation of this function

$$S(\vec{q}, t) = \frac{1}{n} \langle C(\vec{q}, t_0 + t) C(\vec{q}, t_0) \rangle = \frac{1}{N} \sum_{i,j} \exp(-\vec{q}[\vec{r}_i(t_0 + t) - \vec{r}_j(t_0)]). \quad (3.11)$$

When the discrete form is given up in favor of the continuum integral, the expression depends on the particle density.⁴ Furthermore, the assumption of an isotropic probe is applied, which allows us to consider the scalar momentum transfer $q = |\vec{q}|$

$$S(q, t) = \int_0^\infty \frac{\sin(qr)}{qr} [g(r, t) - \tilde{\rho}] 4\pi r^2 dr. \quad (3.12)$$

The scattering function thus represents the Fourier transform of the pair-correlation function $g(\vec{r}, t)$. For the calculation in the present study we consider the discrete version of the function, since we really measure single particle positions⁵

$$S(q, t) = \frac{1}{N} \sum_{i,j} \frac{\sin(q\Delta r_{ij})}{q\Delta r_{ij}}. \quad (3.13)$$

Here, $\Delta r_{ij}(t) = |\vec{r}_i(t_0 + t) - \vec{r}_j(t_0)|$ is the relative displacement of the particles. Comparable to the distinguished contributions in the previous section we may here also differ between the coherent scattering function $S(q, t)$ as defined above and the incoherent scattering function $F_s(q, t)$ which includes only the self part $i = j$. For the incoherent scattering function Δr_{ii} is the mean particle displacement and $F_s(q, t)$ a measure of translational dynamics. As we do not only conduct a particle average in our calculations but a time average over all the possible time origins t_0 , it is customary to denote the ergodic average over time and ensemble via $\langle \dots \rangle$ yielding

$$S(q, t) = \left\langle \frac{\sin(q\Delta r_{ij})}{q\Delta r_{ij}} \right\rangle. \quad (3.14)$$

⁴ For the exact derivation review Refs. 69, 124

⁵ The common expression reads $\cos(q\Delta r_{ij})$, present term from isotropic assumption

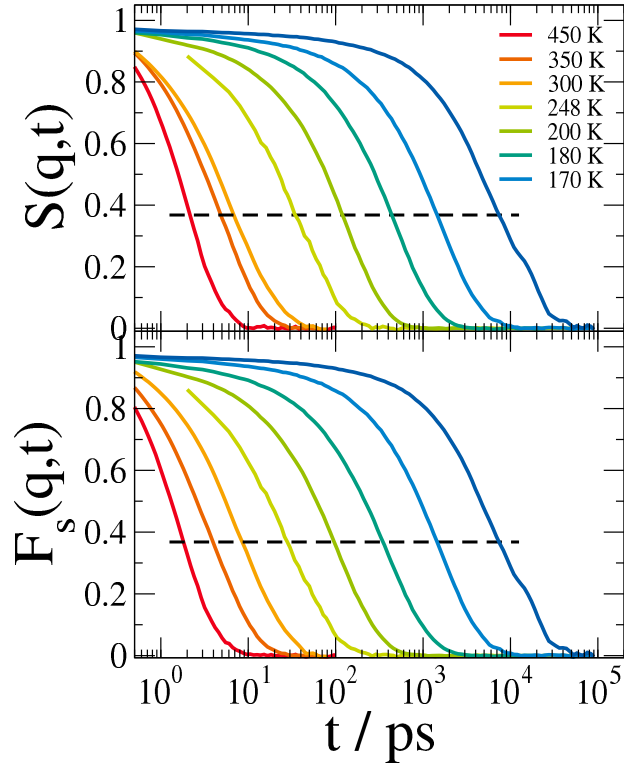


Figure 3.7.: Coherent scattering function $S(q, t)$ (top) and incoherent scattering function $F_s(q, t)$ (bottom) for the oxygen atoms of the exemplary system PPO₂ with scattering vector $q = 9.11 \text{ nm}^{-1}$. Dashed line $1/e$. The vibrational decay is of very small amplitude in this system but evident through a temperature-dependent starting value of all decays.

It is a well-established procedure to characterize the α -relaxation of glassy systems via the non-exponential decay of translational and rotational correlation functions. Here, we choose the incoherent scattering function with momentum transfer $q = \frac{2\pi}{l}$ and l as the characteristic next neighbor distance extracted from $g(r)$. The function is characterized by an exponential, short time, vibrational decay and a long time stretched exponential decay of Kohlrausch-Williams-Watts (KWW) form

$$C_{KWW} = A \exp \left[- \left(\frac{t}{\tau} \right)^\beta \right]. \quad (3.15)$$

From these stretched exponential decays we determine the decay to $1/e$ so that

$$F_s(q, \tau_\alpha) = 1/e, \quad (3.16)$$

where τ_α is the structural or α -relaxation time and the fit value β is called the stretching parameter since it is generally found to be $0 < \beta < 1$.

We have calculated both the coherent and incoherent part of the scattering function and found common behavior for the extracted quantities. In Fig. 3.7 coherent and incoherent scattering functions are shown for an exemplary system demonstrating a merely quantitative difference in time whereas the resulting evolution upon cooling is the same. Following the majority of studies, where most authors focused on the incoherent scattering function, we will restrict ourselves to $F_s(q, t)$.

3.3.3 Translational Diffusion Constant D

In order to characterize the particle diffusion we determine the mean-squared atom displacement (MSD)

$$\langle \mathbf{r}(t_0 + t) - \mathbf{r}(t_0) \rangle^2 = 6Dt \quad (3.17)$$

which is related to the translational self-diffusion coefficient (D) at long times, i.e., in the diffusive regime. The diffusive regime therein is typically indicated by a displacement bigger than the particle size itself. The diffusion constant D is extracted from the MSD via a fit of the function $6Dt$. The angular brackets, $\langle \dots \rangle$, here again denote the ergodic average.

In Fig. 3.8 we present the MSD by way of example for PPO₂. At high temperatures we observe a ballistic regime with characteristic exponent 2 and the diffusive regime with exponent 1 at longer times. Upon cooling the dynamic cage formed by each particles neighbors catches the particle for intermediate times, here represented by a plateau between ballistic and diffusive regime. Approaching the glass transition all systems presented in this study will exhibit these basic ballistic and diffusive regimes along with the caging plateau.

Diffusion constants are experimentally measured via radioactive tracers

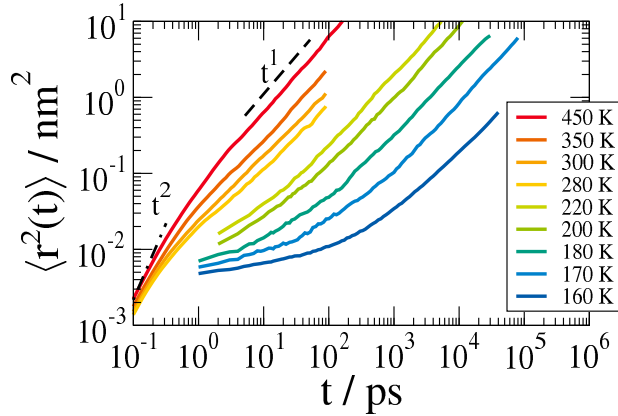


Figure 3.8.: Mean-squared displacement of oxygen atoms in the exemplary system PPO₂. The dashed line represents a slope of 1, marking the diffusive regime.

[125], NMR [126, 127] in a static-field gradient (SFG) or pulsed-field gradient (PFG), quasi-elastic neutron scattering (QENS) [128] and photon-correlation spectroscopy (PCS) [129]. A recently established new measurement will be discussed in chapter 6. It applies the field-cycling (FC) NMR [89, 130–133], which we ascertained regarding the information content of the experimental results in an MD simulation study. (see Ref. 89 and Sec. 6)

For simple liquids the diffusion coefficient (D) is linked with the structural relaxation time τ_α via the well-known Stokes-Einstein relation

$$D \propto \left(\frac{\tau_\alpha}{T} \right)^{-1}, \quad (3.18)$$

which has recently been reported to break down for glass formers at low temperatures [134–139].

3.3.4 Non-Gaussian Parameter $\alpha_2(t)$

Maybe the most basic assumption in dynamic models is a Gaussian distributed particle motion. On the basis of a random walk, a particle or, for polymers, a segment will perform random steps in any direction without a memory effect. Applied in one dimension it is clear that when a step to the right and left is of equal probability the mean displacement after any number of steps is 0. The probability of the displacement is then

given by a Gaussian distribution around 0. When the amount of steps increases the probability distribution widens. In simulations we can calculate the van Hove correlation function in three dimensions $G_s(r, t) = \langle \delta[|\vec{r}_i(t) - \vec{r}_i(0)| - r] \rangle$, which yields the probability of an atom i to travel the distance r in the time t . For a Gaussian motion it is given by

$$G_s(r, t) \equiv G_0(r, t) = \left(\frac{3}{2\pi \langle r_i(t) \rangle^2} \right)^{\frac{3}{2}} \exp \left(-\frac{3r^2}{2 \langle r_i(t) \rangle^2} \right) \quad (3.19)$$

Here, we see how the mean-squared displacement $\langle r_i(t) \rangle^2$ determines the width of the distribution increasing in time. Once the diffusive regime is reached we can describe the function via $6Dt$ and link it to the diffusion coefficient.

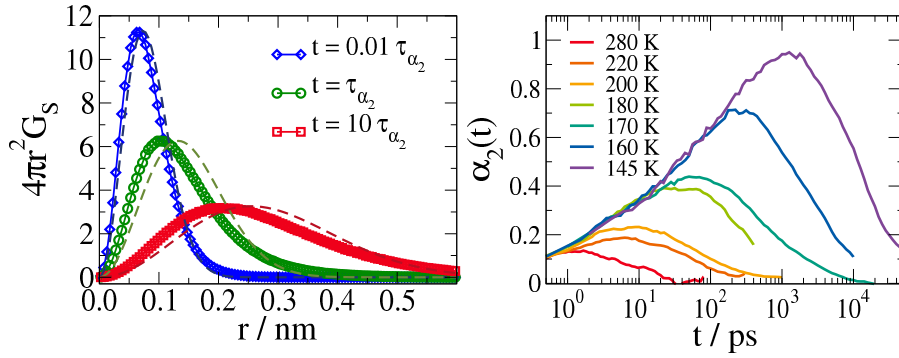


Figure 3.9.: (a) Van Hove correlation function integrated over a spherical surface represents the probability for the particle displacement r after a time interval t . Dashed lines correspond to the predictions of Gaussian distribution in Eq. 3.19. (a) Data for PPO₉ at 450 K calculated by A. Bormuth [87] for variations of the time interval t . (b) Non-Gaussian parameter for PPO₂ at variant temperature T .

In Fig. 3.9(a) we observe characteristic differences between the displacement probabilities calculated for different time intervals t compared to the corresponding Gaussian distributions obtained from Eq. 3.19. Evidently, the deviation from Gaussian behavior depends on the time interval t . Specifically, for the characteristic time τ_{α_2} the deviations are at maximum. Under close inspection it is important to notice the existence of unexpectedly slow and fast particles in comparison to the Gaussian assumption. Previous studies [38] have found that about 5-7% fast particles

exhibit higher displacements than expected for Gaussian statistics.

We mention these fast and slow particles here because we will pick up the topic in the upcoming sections. In Sec. 3.3.5 we will basically observe the slow particles while in Secs. 3.3.6 and 3.3.7 the 5% fastest particles are considered.

In order to quantify the deviations from Gaussian statistics the non-Gaussian parameter

$$\alpha_2(t) = \frac{3}{5} \frac{\langle [r_i(t_0 + t) - r_i(t_0)]^4 \rangle}{\langle [r_i(t_0 + t) - r_i(t_0)]^2 \rangle^2} - 1$$

is defined. This parameter is 0 for homogeneous Gaussian motion. For glass formers, however, it depends on temperature and time. While $\alpha_2(t)$ shows only weak time-dependence at high temperatures it builds up a maximum when cooled down [38, 39, 140]. From the resulting bell-shaped curve we can determine a characteristic time τ_{α_2} corresponding to the maximum of non-Gaussian motion along with its maximum value in the following denoted as $\alpha_{2,max}$. Height and position of $\alpha_2(t)$ are well-known parameters to characterize the occurrence of heterogeneities in dynamic systems. When dynamics are non-Gaussian, theoretic models based on an uncorrelated single dynamic species fail and at least two dynamic species or a backwards correlation must be considered. Non-Gaussian statistics also mean that the simple model of a random walk process fails. This may occur to heterogeneities in the dynamics or to forward-backward correlations, which require a memory kernel in the theoretic model. The following sections will introduce quantities that show these heterogeneities are spatially correlated, which is why they are commonly referred to under the term of spatially heterogeneous dynamics (SHD). Forward-backward correlations were also found in some studies, though with minor significance [38].

3.3.5 Four-Point Density Correlation Function $\chi_4(t)$

A possibility to measure heterogeneous dynamics is a higher-order density correlation function [141] or also called generalized susceptibility and therefore χ . The susceptibility is based on a four-point (2 times, 2 positions) correlation and accordingly named 4-point density correlation function ($\chi_4(t)$). It was introduced as an indicator for SHD at the glass

transition. In previous studies applied to model liquids [50, 142–144] we will now apply it to complexer systems. The theoretical framework was originally introduced to describe critical phenomena in spin glasses and can be found in Refs. 143 and 50.

This short introduction into the basic ideas of a generalized susceptibility is based on an article by Vogel and Glotzer [39]. We want to use a correlation that is taking spatial correlations into account as well as time correlations. Therefore two densities at different times t_i and positions r_i are compared to one another. In other words χ_4 describes the probability to find an atom i at position r_j of the atom j after a time interval t . As this is a very hard criterion a cut-off is usually applied, which smears out the instantaneous location of the particle. Another approach is assuming a smooth transition, so that larger overlaps are contributing in a reduced manner with a weighted factor

$$\frac{\sin[q\Delta r_{ij}(t)]}{q\Delta r_{ij}(t)} \quad (3.20)$$

adapted from Berthier [50]. Here, $\Delta r_{ij}(t)$ is defined as in the previous section.

The density correlations may be characterized with an order parameter counting all overlapping particles.

$$Q(t) = \int d^3r_1 d^3r_2 \rho(\vec{r}_1, t_0) \rho(\vec{r}_2, t_0 + t) \frac{\sin[q\Delta r_{ij}(t)]}{q\Delta r_{ij}(t)} \quad (3.21)$$

$$= \sum_{i=1}^N \sum_{j=1}^N \frac{\sin[q\Delta r_{ij}(t)]}{q\Delta r_{ij}(t)} \quad (3.22)$$

where ρ corresponds to the atom density and therefore the integrator over the whole space denotes the number of atoms in the system. Hence we can describe the order parameter by a sum (see Eq.3.22). Finally, the susceptibility is defined as the variance or fluctuation of the order parameter

$$\chi_4(t) = \frac{\beta V}{N^2} [\langle Q^2(t) \rangle - \langle Q(t) \rangle^2] \quad (3.23)$$

where $\beta = 1/k_B T$. Here, we follow Berthier [50] and drop the original criterion of a cut-off. The observant reader may have noticed that the chosen overlap criterion resembles the scattering function.

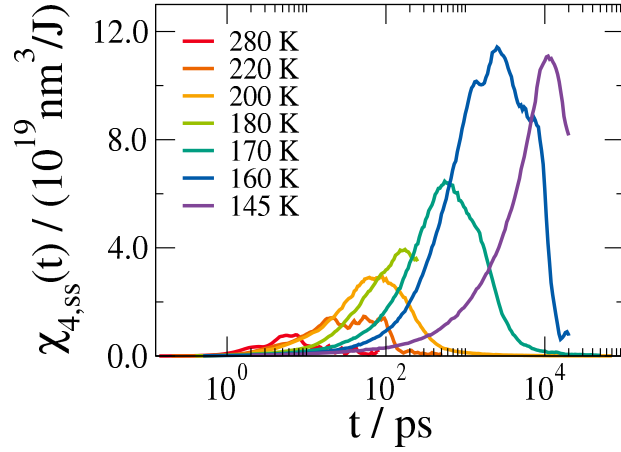


Figure 3.10.: Self-Self part of the 4-point density correlation function ($\chi_4(t)$) for PPO₂ for various temperatures.

Fluctuations in the order parameter as measured by $\chi_4(t)$ are usually found as an indicator for a non-equilibrium state, phase separation or spatial heterogeneity. Our glassy liquids should be in equilibrium though. Nor is a phase separation an option so that changes in the order parameter origin from heterogeneous dynamics in an equilibrium melt. Of course, a glass transition itself is sometimes discussed in terms of an underlying phase transition.

We can split the contributions in the sum of Eq. 3.22 into self and distinct parts. This leaves us with the possibility to define three different types of four-point-density correlations. Much like the difference between coherent and incoherent scattering functions we can take into account only $i=j$, $i \neq j$ or all contributions to the sum. As it has been shown in previous studies [142–144], χ_4 is dominated by the contribution of the self-self part. Subsequently, the present study primarily evaluated this part. Hence, in the following we will always refer to the self part in this work yielding

$$Q_S(t) = \sum_{i=1}^N \frac{\sin[q\Delta r_{ii}(t)]}{q\Delta r_{ii}(t)} \quad (3.24)$$

and

$$\chi_{4,ss}(t) = \frac{\beta V}{N^2} [\langle Q_S^2(t) \rangle - \langle Q_S(t) \rangle^2] \quad (3.25)$$

Cut down to the self-self part of the susceptibility, χ_4 now describes the fluctuations in the typical amount of particles that reside inside their cage

and do not move very far. In contrast to the observables in the following sections $\chi_{4,SS}$ is hence sensitive to immobile particles. Specifically, when the modulus of the scattering vector $q = |\vec{q}|$ is chosen in company with the scattering function in the previous section, $\chi_{4,SS}$ describes the heterogeneity of the structural relaxation.

In Fig. 3.10 we observe that $\chi_4(t)$ much like $\alpha_2(t)$ exhibits a distinct peak at a characteristic time τ_{χ_4} of height $\chi_{4,max}$. Obviously, the occurrence of a peak already states that particles do not escape their cage at any random time as expected for a constant jump rate. The peak implies that slow or immobile particles stay immobile for a rather long time until at a quite well-defined time most particles escape and the final decay of the α -relaxation takes place.

3.3.6 Dynamic Cluster Analysis $S_w(t)$

In order to ascertain the spatial correlation of a special subset of fast particles, we identify the 5% particles of highest mobility in a time interval t and study their spatial distribution performing a cluster analysis. The 5% limit was thereby chosen along with previous works [38, 87], which have demonstrated significantly enhanced mobility for the 5-7% most mobile particles compared to the expected Gaussian distribution of mobility⁶. In the cluster analysis, neighboring, highly mobile particles are grouped into the same cluster. Thereby, neighboring particles reside within their regular intermolecular distance, i.e., up to the first minimum of the intermolecular pair correlation function (see Tab. 3.4).⁷ The result is a probability distribution $p_s(n, t)$ which corresponds to the probability of finding a cluster of size n for a time interval t .

In Fig. 3.11(a) we see how the probability distribution $p_s(n, t)$ varies with time and exhibits an enhanced clustering at a time $t = \tau_s$. Characteristically, the distribution follows a power law, which is, in agreement with other studies [10–12, 38–40], cut off by an exponential decay. Consequently, we calculate the weight-averaged mean cluster size

$$S_w(t) = \frac{\sum_n n^2 p_s(n, t)}{\sum_n n p_s(n, t)}, \quad (3.26)$$

⁶ see also Sec. 3.3.4 and Fig. 3.9

⁷ see also Sec. 3.3.1, Fig. 3.6

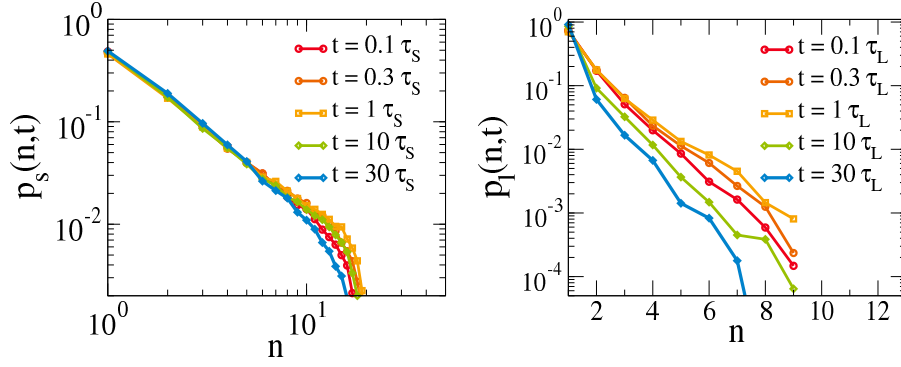


Figure 3.11.: Probability distributions (a) $p_s(n, t)$ to find a cluster with n members for a time interval t measured in units of the peak time τ_s (b) $p_l(n, t)$ to find a string with n members for a time interval t measured in units of the peak time τ_L . Both distributions depend on a specific time scale where cluster/string formation is most likely. Data calculated for PPO₂ at T=180 K.

a quantity that reflects the size of the cluster in which a randomly selected particle most likely resides. Analyses of $S_w(t)$ clearly show significantly larger clusters of mobile particles, than is expected for randomly selected particles [38, 80]. An example of the resulting weight averaged dynamic cluster size $S_w(t)$ is shown in Fig. 3.12(a). Here, the cluster size S_{rand} , representing the number of constant clusters, is used as a normalization to the curve, showing statistic significance.

| System | Atom | δ_s / nm | δ_L / nm |
|--------|------|------------------------|------------------------|
| PPO | O | 0.84 | 0.38 |
| PEO | O | 0.78 | 0.27 |
| PB | C | 0.79 | 0.33 |
| PDMS | O | 1.03 | 0.48 |
| IL | P | 1.1 | 0.55 |
| | CR | 1.14 | 0.43 |
| | CC | 0.705 | 0.26 |
| Water | O | 0.35 | 0.11 |

Table 3.4.: Chosen cut offs for the evaluation of the cluster sizes δ_s and δ_L for the evaluation of the string lengths. In the IL systems the anion atom P and cation atoms CR(ring) and CC(chain) are distinguished.

Following the previous procedure we may again define the peak time τ_s

and the respective height $S_{w,max}$ to characterize the curve.

In order to promote a picture of the principle of clusters we provide an illustration in Fig. 3.13.

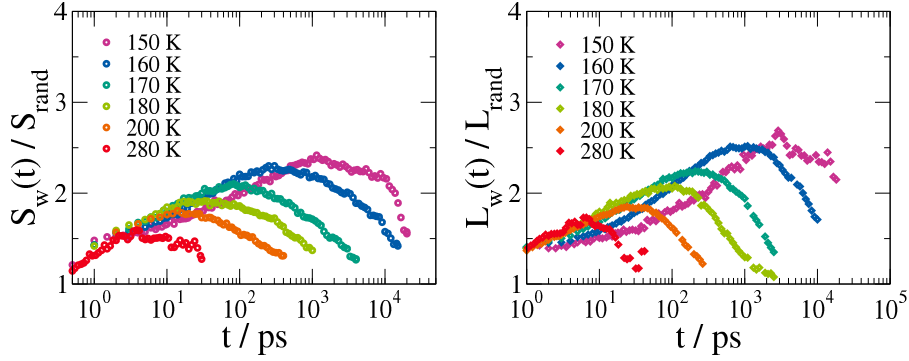


Figure 3.12.: (a) Dynamic cluster size $S_w(t)$ and (b) dynamic string length $L_w(t)$ of the 5% fastest particles for PPO₂. Both functions are normalized by their respective calculations for randomly chosen particles.

3.3.7 Dynamic String Analysis $L_w(t)$

For model glass-formers and polymers it has also been shown that cooperative string-like motion of highly mobile particles is an important relaxation channel [13, 17–19, 38]. Again we denote the 5% most mobile particles as “the mobile particles”. From those we construct strings by connecting any two mobile particles i and j if the condition

$$\min[|\mathbf{r}_i(t_0) - \mathbf{r}_j(t_0 + t)|, |\mathbf{r}_j(t_0) - \mathbf{r}_i(t_0 + t)|] < \delta_L \quad (3.27)$$

holds for the atomic positions at two different times and set δ to about 55% of the intermolecular atom distances⁸. The condition above then refers to one atom moving away while another atom jumps into its former position. It has been shown before [38], that conclusions are not altered when δ is varied in a meaningful range.

Applying the above criterion, we determine the probability that a string of length n is found in a time interval t $p_l(n, t)$. In analogy to the mean

⁸ see also Sec. 3.3.1, Fig. 3.6 and Tab. 3.4

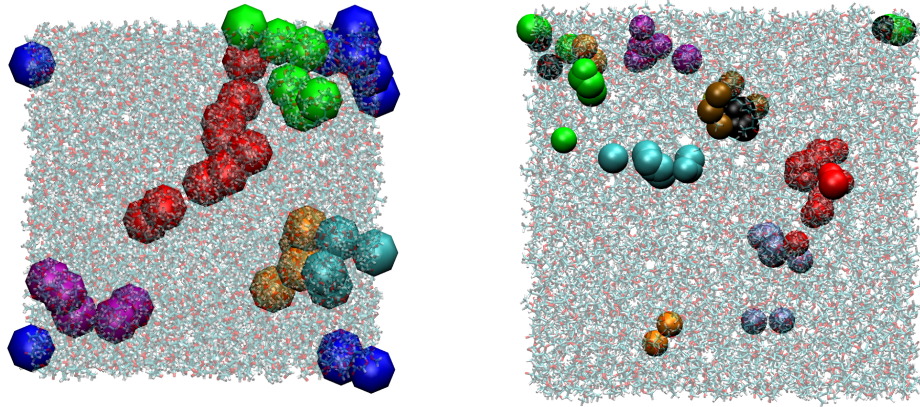


Figure 3.13.: Illustration of (left) clusters of highly mobile particles and (right) strings for PPO_3 at 200 K prepared with vmd [145]. Particles within the same cluster or string are marked in the same color. The bulk system is represented as a transparent background. Note that periodic boundary conditions have to be considered when interpreting these illustrations. The clusters are clearly visible because of their spatial correlation in the specific time frame. Particles within the same string on the other hand may reside further apart from each other. The string particles in this time frame merely occupy a position formerly occupied by another string member. The shown time frames for the cluster and string correspond to their characteristic peak times τ_S and τ_L , respectively.

cluster size in Eq. 3.26, we hence define the weight-averaged mean string size $L_w(t)$. Fig. 3.11(b) presents $p_l(n, t)$ and Fig. 3.12(b) presents $L_w(t)$ normalized by the randomly found strings within the complete ensemble. For $L_w(t)$ we again define the location of the peak via its height $L_{w,max}$ and time τ_L .

As seen in the three previous chapters all presented indicators for spatially heterogeneous dynamics (SHD) exhibit a peak at times about τ_α that shift with its evolution in temperature. Furthermore, the respective peak heights increase upon cooling. The underlying distribution of string lengths probability distribution to finding a string of length n at time t ($p_l(n, t)$) resembles the exponential decays found in previous studies [38, 39].

4 Bulk

Our main goal in this study is to investigate the nature of the glass transition. Beyond our rudimentary introduction in the previous chapters, where it occurred upon cooling, the glass transition is also observed when other control parameters are varied. Approaching the glass transition we have also seen that the volume decreases upon cooling.¹ Subsequently, we may also assume the volume as a relevant control parameter. Furthermore, high pressure [146] induces a similar glass transition, which is object of current research [34, 146–152] and debated as equivalent to the transition upon cooling. Assuming the observed transition with other control parameters exhibits the same fundamental physics, the control parameters are equivalent. Furthermore, it remains unclear, which of those parameters or their combinations is correct to describe the glass transition. Alternatively, pressure and volume effects may better be comprised within the concept of the configuration entropy S_{conf} . Assuming that spatially heterogeneous dynamics (SHD) characterize at least part of the concepts of cooperatively rearranging regions (CRRs) or entropic droplets, however, it is also of interest to describe the glass transition within SHD related observables.

In the search for relevant control parameters, scalings of the structural relaxation time τ_α are used as proof for a good description of the glass transition [146, 153, 154]. Unfortunately, all of these scalings introduce new fit parameters with a priori unknown physical meaning. In order to ascertain the relevance of a scaling approach and the underlying control parameter, it must be tested for a variety of systems. In this study we complement temperature and pressure variations of polymer systems and an ionic liquid. Thereby, we also investigate variations of the polymer chain length and provide benchmarks to interpret the evolution of the fit parameters for the different scalings.

Volume Effects

Intuitively, the ability of a glassy system to rearrange strongly depends on the amount of unoccupied space available for rearrangements. In other terms, a high density requires a certain cooperativity when particles cannot simply jump into voids but must wait for other particles to make room.

¹ see Fig. 2.1 in Sec. 2.1

Hence, previous works [150, 151] studied volume influences at constant temperature and vice versa, i.e., they implemented controlled pressurized systems. For OTP it could be shown that under high pressures interactions are prominently dominated by a soft sphere r^{-12} potential yielding a description via a single quantity $T^{-1}V^{-4}$. The $V^{-4} = r^{-12}$ term here describes the pressure in the system and its influence on the glass transition via a repulsive potential. Within a densely packed system the repulsive force between the particles due to the Pauli principle will surely influence dynamics and the glass transition. Previous studies later on introduced a flexible parameter γ into the quantity $T^{-1}V^{-\gamma}$, thereby generalizing the principle for the application to a wide range of systems. Here, 3γ describes the functionality of the Pauli repulsion for other, non-Lennard-Jones systems. Studies [155–159] on model liquids incorporating a generalized Lennard-Jones potential²

$$U(r) = \frac{A}{r^{3\gamma}} - \frac{B}{r^{1.5\gamma}} \quad (4.1)$$

supported this idea and were able to tune the needed exponent via the potential. In these studies it was also shown that the correlation between the

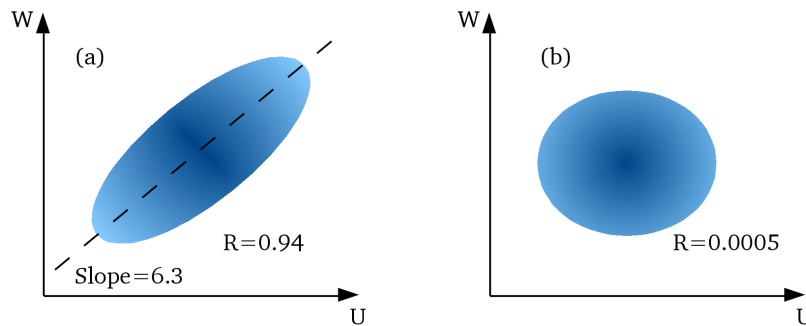


Figure 4.1.: Schematic representations of the findings of Bailey et. al. [156]. The virial W as a function of the potential energy U for (a) Lennard-Jones potential with strong correlation indicated by the correlation coefficient R and (b) TIP5P water with additional Coulomb interactions and insignificant correlation.

total potential energy U and the virial W are reflected by the exponent γ . The virial

$$W = -\frac{1}{2} \mathbf{r}_{ij} \mathbf{F}_{ij} \quad (4.2)$$

² an exemplary illustration of the classic Lennard-Jones potential can be found in Fig. 3.2 of Sec. 3

is used in simulations to calculate the pressure

$$P = \frac{2}{3V}(E_{kin} - W) \quad (4.3)$$

and thus holds information about the answer of the system to volume changes. For the model systems from above [155–159] it was shown that the potential energy U and the virial W are not only strongly correlated but the correlation coefficient resembles γ as is expected considering $U(r) = r^{-3\gamma}$

$$W \sim \mathbf{r}F \sim \mathbf{r}\vec{\nabla}U \sim -3\gamma U. \quad (4.4)$$

For the present study it remains unclear if complex systems with additional intramolecular interactions and a variety of different non-bonded potentials are effectively captured within this picture. For water [156] it has been shown that no correlation between U and W is found, while it is still possible to apply the scaling procedure (see Fig. 4.1). Apart from chemical differences in our systems we will also study the chain-length dependence of the effect.

Entropy Effects

The result of the AG theory

$$\tau = \tau_0 \exp\left(\frac{B}{TS_{conf}}\right). \quad (4.5)$$

reveals the configuration entropy S_{conf} as a possible control parameter that cannot be obtained trivially. For model systems and water [36, 37, 160–162] it was possible to define S_{conf} as the difference between the total and the vibration entropy³. These extensive thermodynamic calculations are quite complicated particularly for complex fluids. Hence, an alternative approach, which is obviously not as accurate, yet allows to perform similar evaluations, is required. It is given by Green’s entropy expansion [163]

$$S = S_{id} + S_2 + S_3 + \dots = S_{id} + \sum_{n=2}^{\infty} S_n, \quad (4.6)$$

which allows to determine the entropic deviations from the ideal gas entropy S_{id} . The entropy expansion divides the entropy into a simple ideal

³ For details please refer to Refs. 36 and 161

gas contribution and higher order contributions associated with pair correlations and higher order correlations involving more than two particles. For an ideal gas the pair correlation function yields a uniform distribution at all distances, whereas in glass forming liquids as discussed here we observe deviations from a uniform value at short distances. In a first order approximation it is therefore possible to assume that the entropy of the system is described by the ideal gas entropy in combination with the pair-correlation entropy S_2 . In contrast to the thermodynamically correct approach for model liquids this approach is clearly motivated from a high-temperature point of view, where the ideal gas entropy may be a valid reference point. Obviously, the two approaches are not equivalent, yet it is not a priori clear that S_2 does not represent a valid approximation of S_{conf} .

Spatially Heterogeneous Dynamics and the Stoke-Einstein Relation

SHDs have been found in various simulation works of model liquids and chemically realistic systems [10–12, 38–40]. They are part of the idea or an interpretation of CRR in the Adam-Gibbs (AG) and Random First Order Transition (RFOT) approaches. Specifically, it is possible to identify particles that show a significantly enhanced mobility and are spatially correlated. Thereby, time scales of SHD and their temperature dependence have been studied frequently [15, 17, 23, 38, 56]. Recently, A. Bormuth [87] found a power-law relation between the time scale of the non-Gaussian parameter and the structural relaxation for different chain lengths of PPO. A generalization of these finding has not been done to our knowledge so that a comparative study of other systems along with application of the scaling to data from previous studies is of great interest. A priori it is thereby unclear when SHD occur, and if they describe structural α -relaxation time defined via $F_s(q, t)$ (τ_α) or the other way around. Furthermore, SHD are discussed as a direct measure of the size of CRRs, which would enable indirect conclusions to the magnitude of S_{conf} [17, 164]. Moreover, it is not trivial that SHD necessarily are correlated to τ_α when the diffusion coefficient $D \sim 1/\tau_\alpha$ also measures the rate average of dynamics. Correlation between D and SHD are hence as much of interest as the relation to τ_α , where D is by definition more sensitive to fast dynamics and τ_α to slow dynamics. The two quantities are furthermore linked to each other by the Stokes-Einstein (SE) relation, which is therefore also of interest to us.

Previous studies with a variety of methods including nuclear magnetic

resonance (NMR) spectroscopy [134, 136], neutron scattering (NS) [136, 138], and MD simulations [134, 135, 137] found the SE relation

$$D = \left(\frac{\tau_\alpha}{T} \right)^{-1} \quad (4.7)$$

to break down at low temperatures and for water [134–136] to cross over to a fraction SE relation

$$D = \left(\frac{\tau_\alpha}{T} \right)^{\xi_{SE}}. \quad (4.8)$$

Further approaches already linked the breakdown of the Stokes-Einstein relation and its rotational counterpart the Stokes-Einstein-Debye relation to the non-exponential decay of the structural relaxation for ortho-terphenyl [165]. While a lot of data for D and τ_α has been published for a variety of model liquids [10, 13, 15, 17, 23, 33, 166–169], only some studies on water [134, 135, 137] have determined if and how a breakdown of the SE relation occurs. For water the breakdown and its corresponding exponent has been linked to possible phase transitions in supercooled water. For the present study it is hence of interest to study the SE breakdown as an indicator for the glass transition independent from possible phase transitions for the case of water.

The idea of SHD is an especially prominent part of the Dynamic Facilitation (DF) theory, which is completely founded on the idea of dynamic regions influencing neighboring particles and propagating relaxation through direct proximity between slow and fast particles. Within MD simulations a direct calculation of the relative contribution of DF mechanisms has successfully been applied to a Dzugutov system [56] and SiO_2 [23]. The available systems in this study will, hence, allow us to generalize these findings and contribute results from other complex systems such as the polymers, an ionic liquid and water from F. Klameth [1].

This section will test basic ideas for a generalized scaling including temperature and pressure variations. First, we introduce a volume scaling approach, which proposes a volume-temperature scaling. Then, we follow the AG approach and apply an entropy-scaling approach.⁴ Finally, we follow up on recent findings by A. Bormuth [87] and investigate several scalings between characteristic times of relaxation, diffusion and indicators for SHD extended by DF observations.

⁴ The details can be found in Sec. 2.1.3

4.1 Volume Scaling

In Fig. 4.2(a) we see the well-known Arrhenius representation of τ_α as a function of the inverse temperature for various pressures⁵. The data at higher pressures is shifted towards longer τ_α . If we assume the proposed scaling procedure to be valid, all data points of comparable τ_α must be shifted to agreement via the volume. When the exponent for the volume scaling γ is chosen correctly, a master curve as, e.g., in Fig. 4.2(b) is obtained.

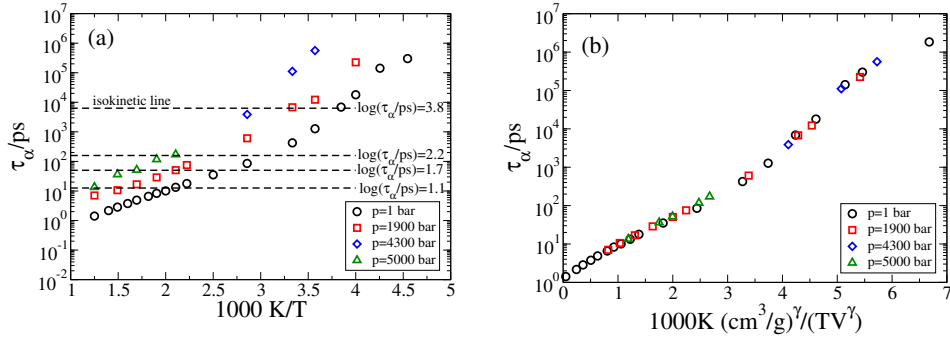


Figure 4.2.: (a) The structural relaxation time τ_α as a function of the inverse temperature in a typical Arrhenius plot for PPO₉ under different pressures. Each data set separately follows a VFT function indicated by slight fragile behavior at low temperatures and a strong, Arrhenius behavior at high temperatures. Dashed lines indicate isokinetic points of similar correlation time. (b) The scaled version of the Arrhenius plot including the specific volume $V = \rho^{-1}$ to the power of a characteristic exponent γ . Here, $\gamma = 3.45$ represents the systems specific exponent for PPO₉.

In detail, we determine the exponent γ via the indicated isokinetic lines in Fig. 4.2(a). Along an isokinetic line all data points are required to yield the same value for the scaled x axis $TV^\gamma = \text{constant}$. Conclusively, we may formulate the requirement along an isokinetic line as

$$\log(T) \propto -\gamma \log(V) \quad \text{or} \quad T = \exp(a - \gamma \log(V)). \quad (4.9)$$

When we pair up the data points and corresponding simulations identified in Fig. 4.2(a) in a plot of the temperature as a function of the volume

⁵ with τ_α defined via the incoherent scattering function ($F_s(q, t)$)

we obtain Fig. 4.3(a). Here, we determine the perfect value of the exponent γ for each dynamic point. If previous studies were correct and γ is a system property, we need to accumulate the obtained time-dependent γ values to one parameter. Therefore, we use the preliminary fit to obtain $T(V = 1 \text{ g/cm}^3)$ and shift all isokinetic lines from Fig. 4.3(a) onto one line. The combined curves displayed in Fig. 4.3(b) are then again fitted according to Eq. 4.9. We choose this two-step fit in order to take into account that the number of points along the isokinetic lines varies. With the applied procedure we make sure all points contribute in the same way.

In Fig. 4.3(b) we display the results for γ and its standard error for each of the polymer systems with a reasonable amount of data. Evidently, the differences of the analyzed polymers on a chemical level result in different exponents γ , while the chain length effect for the available systems is small. Due to the limited amount of data and systems it is not possible to draw conclusions regarding the chain length influences.

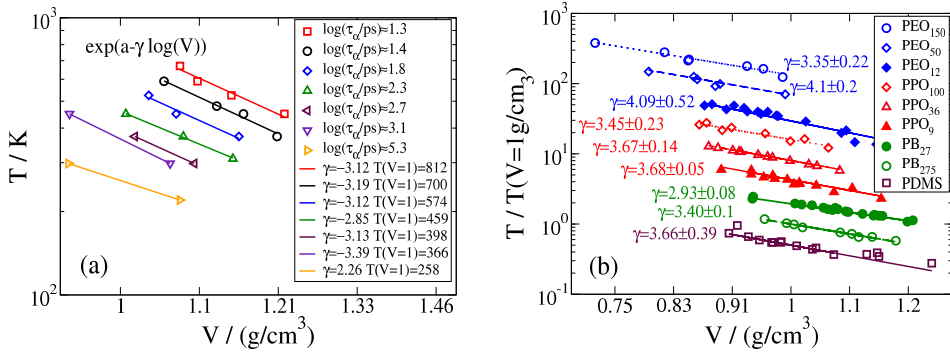


Figure 4.3.: (a) Temperature T as a function of the specific volume, i.e., inverse density $V = \rho^{-1}$ for several isokinetic points of PB_{27} , where $TV^\gamma = \text{const}$. The exponent γ can then be extracted by any power law function, e.g. the given $\exp(a - \gamma \log(V))$. Evaluation of all fit curves at $V = 1 \text{ g/cm}^3$ is given as a normalization factor to construct a master curve. (b) Master curves constructed by division with the calculated temperatures at $V = 1 \text{ g/cm}^3$ shifted by a factor 2^n to enable better visibility. Note the double logarithmic representation.

Applied to the relaxation times the scaling yields good agreement for systems of various pressures within one chain length. Furthermore, the data in Fig. 4.4(a) exhibit very similar curves for the different chain lengths of the polymers. Comparison of our MD simulation with experimental data

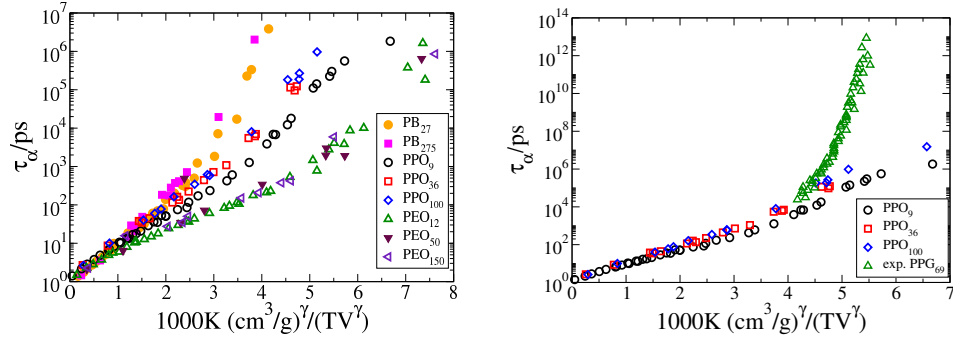


Figure 4.4.: (a) Scaled Arrhenius plot as a function parameter $T^{-1}V^{-\gamma}$ for indicated polymer systems and pressure $p = 1 - 10000$ bar. (b) PPO data in comparison to PPG₆₉ [170] with $\gamma = 2.5$. The considerably smaller exponent γ yields a significant deviation of the curves at small free volumes.

on PPG from DS [170] in Fig. 4.4(b) reveals significant differences between the two methods and polymers.

Many studies have shown differences in the correlation times obtained from the different methods, whereas fragility is commonly assumed to be a method-independent effect. The observed differences between PPO and PPG therefore are most likely due to hydrogen bonds forming between the O-H end groups of PPG, which cause a diverse slowdown of dynamics as exhibited in PPO.

| Material | Chain length N | γ | Reference |
|------------------------------|----------------|-----------------|--------------|
| Poly(ethylene oxide) | 150 | 3.35 ± 0.22 | * |
| Poly(propylene oxide) | 100 | 3.45 ± 0.23 | * |
| Poly(propylene glycol) | ≈ 69 | 2.5 | ^a |
| Poly(dimethylsiloxane) | 19 | 3.66 ± 0.39 | * |
| Poly(methylphenylsiloxane) | | 5.6 | ^b |
| Poly(methyltolylsiloxane) | | 5.0 | ^c |
| Poly(butadiene) ^d | 275 | 3.4 ± 0.1 | * |
| Poly(butadiene) ^e | ≈ 2000 | 1.8 | |

Table 4.1.: Master curve parameter γ from this work in comparison to previous studies of similar polymers. *this work, ^aRoland et al [170], ^bPaluch et al [149], ^cPaluch et al [148], ^d(40% cis, 50% trans, 10% vinyl), ^e(1,4 copolymer) Alba-Simionesco et al [171, 172].

In a series of four papers [156–159] Dyre and co-workers have linked the occurrence of $\gamma \neq 4$ with the correlation between the total energy of the system and the virial. Here, similar to findings in water [156] this is not the case neither for a system close to $\gamma = 4$ represented by PEO₁₂ nor with $\gamma \neq 4$ represented by PB₂₇. Similar findings previously indicated that Coulomb interactions and intramolecular interactions disturb the correlation best seen in Lennard-Jones (LJ) models [156]. In Fig. 4.5 we show the virial W as a function of the potential energy U and find a symmetric shape not indicating any linear correlation. In previous studies [156–159] with model systems the correlation was found to be so strong that the complementary representation yielded strongly correlated, cigar-shaped data with a linear slope 3γ as illustrated in the beginning in Fig. 4.1. The enhanced complexity of the intramolecular structure and mixture of interactions mask the trivial explanation from Ref. 156.

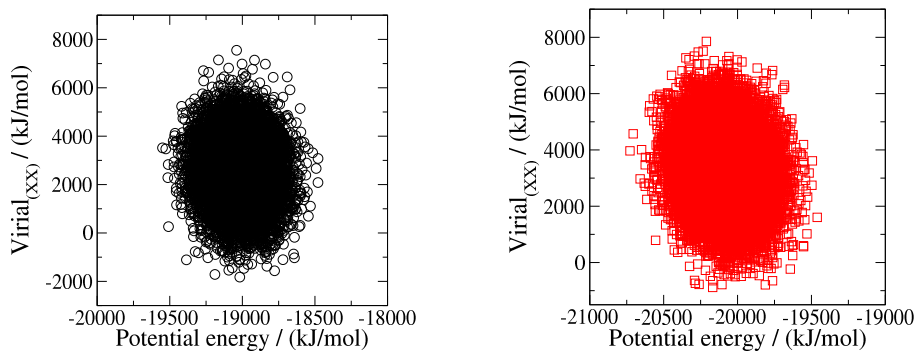


Figure 4.5.: The XX component of the virial matrix over the total energy of the system for PEO₁₂ at 250K (left) and PB₂₇ at 220K (right) calculated with the GROMACS [98–101] routine `g_energy`. The dot shape of the data reveals no correlation between the two quantities.

In this section we have found that a joint scaling of volume and temperature is a good control parameter, which incorporates both temperature and pressure variations into a single approach for the description of the glass transition. Thereby, the volume contributes similar to a repulsive potential yet with a reduced exponent $\gamma < 4$. The additional Coulomb and bonded interactions have thus softened the potential. Within the limited amount of available data we have not found significant influences of the chain length N . Our MD analysis to our knowledge has been the first to apply this temperature-volume scaling to chemically realistic force fields of polymers. Unfortunately, the available experimental data is not available

for the exact same polymers and typically at lower temperatures so that we cannot draw a clear conclusion from the comparison in Fig. 4.1. Yet, we have shown the procedure is applicable for the simulations at relatively high temperatures.

4.2 Adam-Gibbs Scaling

In order to ascertain the AG theory and to determine the configuration entropy S_{conf} we apply the approximation

$$S_{conf} \approx S_{id} + S_2, \quad (4.10)$$

where S_{id} is the ideal gas entropy in the high-temperature limit and S_2 the pair-correlation term of Greens entropy expansion. S_2 can be obtained by the pair-correlation function $g(r)$ defined in Sec. 3.3.1 and with particle density ρ and number of particles N by

$$S_2/Nk_B = -2\pi\rho \int_0^\infty \{g(r) \ln g(r) - [g(r) - 1]\} r^2 dr, \quad (4.11)$$

which essentially measures the deviations from the uniform correlation expected for the ideal gas.

The pair-correlation entropy is a negative quantity, which reduces the ideal-gas entropy, because it gives the glass a local structure and therefore locally an entropy closer to that of the crystal with $S_{conf} = 0$. With increasing temperature the local structure becomes less prominent and the entropy increases. Since the systems at hand are large chain molecules⁶ the pair-correlation entropy will clearly never reach a uniform value, because the covalent bonds always produce preferred next neighbor distances. Upon heating, these next neighbor distances become dominated by intramolecular effects by bonds and bends, whereas in the supercooled state cooperatively rearranging regions of particles within different chains contribute.

In Fig. 4.6(a) we see how this effect leads to small values of S_2 at low temperatures and higher values at high temperatures. In addition to the temperature dependence, S_2 exhibits a chain length dependence. For short

⁶ Polymers and a chain-like cation in the ionic liquid

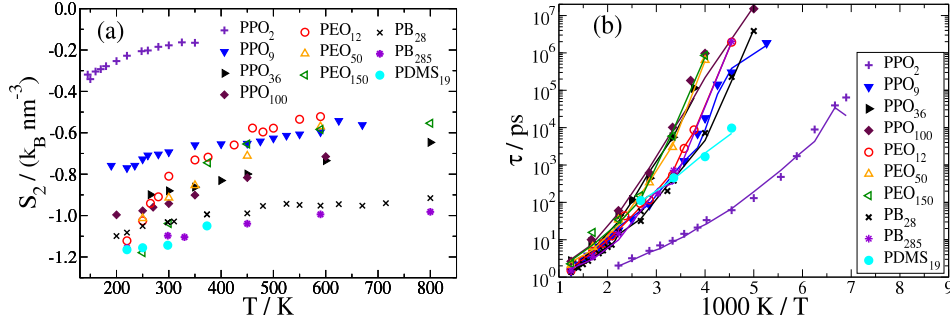


Figure 4.6.: Left: The temperature-dependent pair-correlation entropy S_2 calculated with Eq. 4.11. Right: Arrhenius plot of the correlation times τ for all polymer systems a pressure $p = 1$ bar. Symbols represent the calculated data points and solid lines represent the fit according to Eq. 4.12, where the values of S_2 are taken from Eq. 4.11. All system at pressure $p = 1$ bar

chains with minor influences of intramolecular pair correlation the deviations from the ideal gas or a uniform pair correlation are smaller than for long chains where a significant number of pair correlations are well-defined intramolecular contributions. Thus, for increasing chain length N the absolute value of S_2 increases.

With the temperature-dependent entropy S_2 known, it is possible to estimate the ideal gas entropy S_{id} through the fit of the Adam-Gibbs representation of the relaxation time

$$\tau = \tau_0 \exp\left(\frac{B}{T(S_2 + S_{id})}\right). \quad (4.12)$$

The relevant data along with the fit of the equation is displayed in Fig. 4.6(b). For each system the fit yields along with the other fit parameters the ideal gas entropy for the specific systems as given in Tab. 4.2. Of course, the ideal gas entropy is as the term says ideal and known for mono-atomic gases. Here, with the approximation of Eq. 4.10 we have incorporated higher order correlations and deviations from the mono-atomic gas into S_{id} . The fitted values for S_{id} are scattered about $S_{id}/Nk_B \approx 80 \text{ nm}^{-3}$. Within the PPO systems the fit values increase for longer chains, while for the other polymers no chain length effect is evident.

When the approximation of the configuration entropy $S_{id} + S_2^7$ is incorporated into the x-axis, as in Fig. 4.7 we observe all systems are converted

⁷ in some publications it is referred to as configurational entropy.

| System | p / bar | $S_{id} / (Nk_B \text{ nm}^{-3})$ | B / ($\text{J} \cdot 10^3 \text{ nm}^{-3}$) | τ_0 / ps |
|--------------------|---------|-----------------------------------|---|----------------------|
| PPO ₂ | 1 | 32.24 | 26.42 | 0.19 |
| PPO ₉ | 1 | 55.58 | 37.36 | 0.26 |
| | 1900 | 54.50 | 31.51 | 0.78 |
| | 5000 | 86.60 | 110.26 | 0.80 |
| PPO ₃₆ | 1 | 55.49 | 9.95 | 0.30 |
| | 5000 | 57.7 | 37.88 | 1.67 |
| PPO ₁₀₀ | 1 | 77.78 | 71.99 | 0.27 |
| PEO ₁₂ | 1 | 80.38 | 109.89 | 0.18 |
| | 1900 | 64.04 | 65.41 | 0.34 |
| | 5000 | 45.4 | 25.04 | 1.18 |
| PEO ₅₀ | 1 | 58.21 | 47.98 | 0.46 |
| PEO ₁₅₀ | 1 | 124.26 | 115.85 | 0.23 |
| PB ₂₈ | 1 | 69.93 | 25.89 | 0.22 |
| | 1900 | 68.66 | 84.35 | 0.1 |
| | 5000 | 66.43 | 108.02 | 0.07 |
| PB ₂₈₅ | 1 | 68.12 | 15.67 | 0.426 |
| PDMS ₁₉ | 1 | 49.78 | 41.42 | 1.0 |

Table 4.2.: Fit values of Eq. 4.12 with τ , S_2 and T as an input.

into linear representations with slope A from Tab. 4.2. This result illustrates the validity of the equation for relaxation by the AG theory. While, the curves in Fig. 4.7(a) are quite different due to chemical differences and variant chain lengths, pressure variation is supposed to be described within the theory. In Fig. 4.7(b) we therefore present data for various pressures, which is additionally rescaled by the fit parameter τ_0 . The data experience reasonable agreement for the different pressures considering that S_{conf} has been approximated by the pair-correlation entropy. Specifically, for moderate temperatures this scaling shows that the AG theory and consideration of the configuration entropy yields a good description of the glass transition.

Obviously, the explanatory strength of this scaling helps to combine temperature and pressure effects just like the volume scaling of the previous chapter. The combination of the ideas from AG and Mode-Coupling Theory (MCT) has led to RFOT theory, which proposes the surface energy between entropic droplets is a significant interaction of the glass transition. AG theory and its applicability in the present case are included in RFOT so that our findings can mark one case, where the surface exponent θ and dimension of the droplets d of RFOT resembles AG. Minor devia-

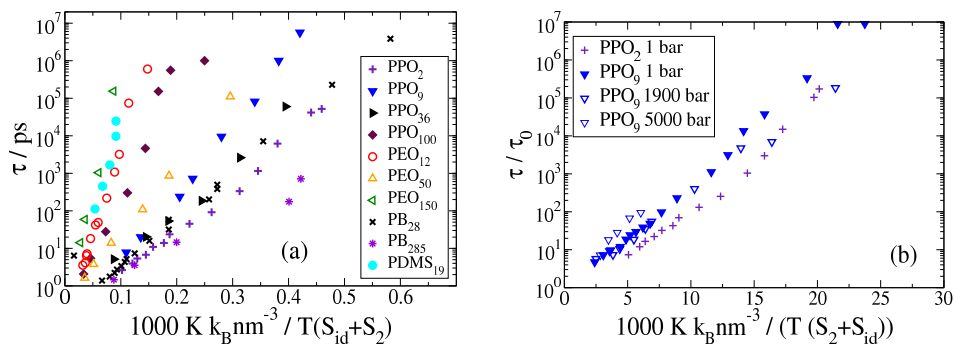


Figure 4.7.: Adam-Gibbs scaling with $T(S_{id} + S_2)$ for (a) all systems at $p=1$ bar and (b) PPO₉ at variant pressure. The scaling transforms the curves into a linear representation. For variant pressure in (b) the scaling comes close to yield a master curve.

tions within the methodical error as shown in Fig. 4.7 can origin from the simulations or from small deviations from AG, which support RFOT theory. Thus, we will present further investigations in order to distinguish between AG and RFOT theory.

4.3 Hyperscaling

In this section we will investigate SHD as a characteristic feature of the glass transition. For this purpose we evaluate the characteristic peak times of the non-Gaussian parameter τ_{α_2} , the 4-point density correlation function τ_{χ_4} , the weight-averaged dynamic cluster size τ_S , and weight-averaged dynamic string length τ_L .⁸ The characteristic peak times of the SHD indicators describe at which time the specific form of SHD is most prominent. They have been studied for various systems as a function of temperature [10, 15, 17, 23, 38], thereby exhibiting mostly weaker temperature dependence than the structural relaxation time τ_α .

In the present study we will act on the suggestion of A. Bormuth [87] to investigate the correlation of characteristic time of the non-Gaussian parameter ($\alpha_2(t)$) peak, τ_{α_2} , and structural α -relaxation time defined via $F_s(q, t)$ τ_α directly to observe the decoupling of the time scales. Furthermore, our study extends the original idea to a variety of systems and additional SHD indicators and proposes a scaling with the diffusion coefficient D as an alternative to τ_α .

Similar to the data by A. Bormuth in Ref. 87 we find that a logarithmic plot of τ_{α_2} over τ_α yields a power law $\tau_{\alpha_2} \sim \tau_\alpha^\nu$, where ν is about 0.75. The principal finding depends neither on the chain length of the polymer nor on the pressure of the system.⁹ In Fig. 4.8(a) we present our own data for the polymers and the ionic liquid along with water data from F. Klameth [1] and other literature data. The solid lines are guidelines for the eye indicating $\nu = 0.75$. In order to ensure that each curve is still visible, only data for 1 bar and one chain length for each polymer has been included. The data for higher-pressure systems, however, follows the same trend and do not change the results. As indicated in Tab. 4.3 all systems yield a fit value of ν close to 0.75. These findings have not been reported anywhere else but in Ref. 87 by A. Bormuth. The present study is therefore the first to show this scaling for more than one system. Furthermore, this study is the first to prepare data from older studies of liquids in this form. The presented data includes model liquids such as LJ, hard sphere (HS), and Dzugutov liquids along with the realistic molecular liquids water and SiO_2 , the ionic liquid, and the polymers. We have therefore found a

⁸ For a detailed explanation of the definition, please refer to Secs. 3.3.4 - 3.3.7

⁹ We demonstrate this behavior in Appendix B.1 for various pressures and chain lengths

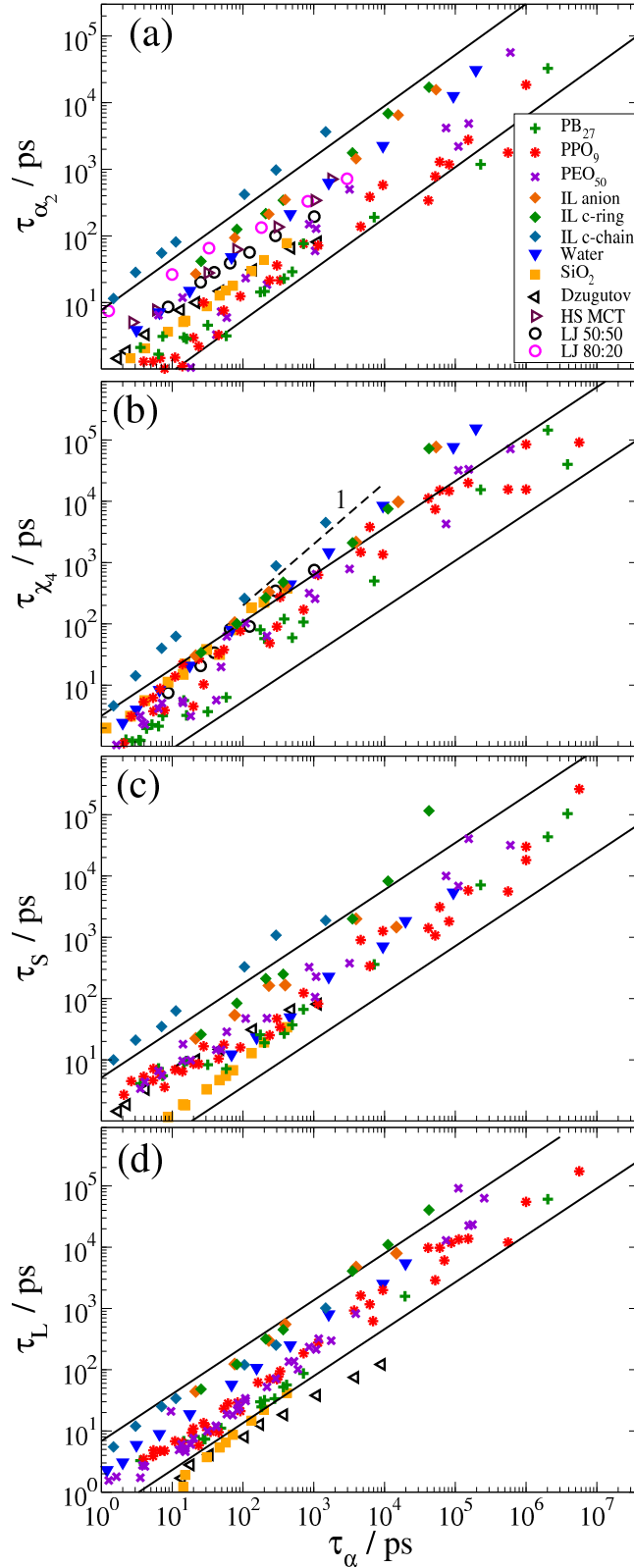


Figure 4.8.: The maximum times of SHDs a) non-Gaussian parameter α_2 , b) 4-point-density-correlation χ_4 , c) mean cluster size S_w d) mean string length L_w as a function of the structural relaxation time τ_α . Solid lines represent an exponent of $\nu = 3/4$ dashed $\nu = 1$.¹⁰

universal feature for a variety of glass-forming liquids. Where exponent $\nu = 0.75$ indicates that the time scales of τ_α and τ_{α_2} separate continuously.

Very similar to these findings for the non-Gaussian parameter are the results for τ_{χ_4} , τ_S and τ_L in Fig. 4.8(b), (c), and (d). While the characteristic times of the cluster and string analyses of the highly mobile particles basically experience similar behavior, the characteristic times of $\chi_4(t)$ are different. Specifically, in Fig. 4.8(b) for τ_{χ_4} we see two classes of systems. The small, simple molecules and IL, which experience “only” glassy dynamics follow an exponent $\nu = 1$, while the complex polymer systems stick to the exponent $\nu = 0.75$ as experienced in the other figures. Evidently, $\chi_4(t)$ as an indicator for SHD is different than the other values.

The findings in Fig. 4.8 suggest that SHD are not perfectly correlated with the structural relaxation, hence, it is of interest to investigate the correlation with the diffusion coefficient D . The structural relaxation time τ_α is defined as the characteristic time at which the incoherent scattering function has decayed to $1/e$. Thus, τ_α is not specifically sensitive to highly mobile particles but indicates when most particles have moved. The diffusion coefficient on the other hand describes the timescale on which the most mobile particles are able to perform free diffusion. The reason for the difference in sensitivity for fast and slow relaxation times lies within the difference between time and rate averages. The time average as in the relaxation time is dominated by long times, whereas a rate average of $1/\tau_\alpha$ as in D is dominated by short times. Subsequently, we have defined a timescale for rather immobile particles τ_α and rather mobile particles D .

Complementary to Fig. 4.8 we hence provide Fig. 4.9 for the characteristic times of SHD as a function of the inverse diffusion coefficient D^{-1} . Here, we again find a power law $\tau_{\alpha_2} \sim D^{-\nu}$. However, the fit yields $\nu \approx 1$ for most systems and characteristic times. The respective fit parameters for each system and characteristic time can be found in Tab. 4.3. Thus, we find that the indicators for SHD presented here experience a stronger correlation with D than with τ_α . Considering that D rather than τ_α is sensitive to particles of higher mobility, which were identified as the origin of SHD¹¹, one may expect an exponent closer to 1.

¹⁰ Literature data: SiO₂ [23], LJ(50:50) [15, 166], LJ (80:20) [10, 13, 167, 168] {with Argon parameter $t = 0.3$ ps [15]}, Dzugutov [17, 169], HSS MCT [33]

¹¹ We have shown this in Sec. 3 along with complementary studies [23, 38, 87].

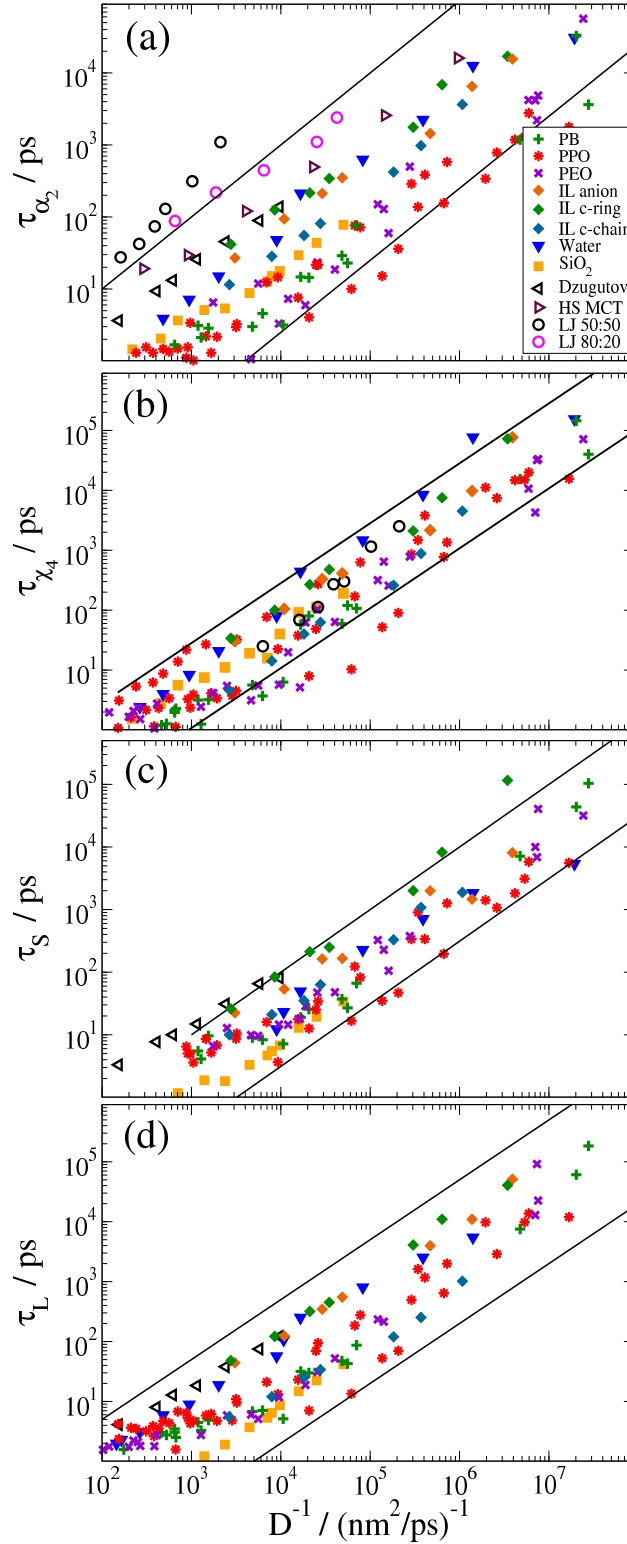


Figure 4.9.: The maximum times of SHDs a) non-Gaussian parameter α_2 , b) 4-point-density-correlation χ_4 , c) mean cluster size S_w , d) mean string length L_w as a function of the inverse diffusion coefficient D^{-1} . Most quantities exhibit a scaling with $\nu = 1$ for the available data of polymers and glass-forming liquids.¹²

Compared to the scaling with τ_α , however, the data for the different systems, e.g., in Fig. 4.9(a) have shifted apart from each other. The expanded representation in Fig. 4.9 may result from differences in the average jump length of each system and, for polymers, from the existence of the Rouse regime. We demonstrate this behavior in Fig. 4.10, where the diffusion coefficient is rescaled by the average jump length δ defined as the first maximum of the intermolecular pair-correlation function.¹³ For τ_{α_2} we find that the inclusion of the jump length into the diffusion constant D/δ^2 shifts the data for most systems closer together. Thereby, we exclude only polymer systems with substantial lengths, i.e., the short chain of PPO₂ is well included in the rescaling as shown in Fig. 4.10(a). For longer chains it is not surprising that the simple rescaling with the jump length δ does not suffice. Moreover, for polymers it is expected that the diffusion constant D is lower than for the respective monomer or short chain. The effect is well-known and has been investigated in detail by A. Bormuth [87]. The diffusive regime for a polymer is delayed due to the preceding Rouse regime and, hence, we expect the polymer data to be separated from the simple liquids.

| | ν | | | | | | | |
|------------------|-------------------|-----------------|--------------|--------------|-------------------|-----------------|--------------|--------------|
| | τ_α | | | | D^{-1} | | | |
| | τ_{α_2} | τ_{χ_4} | τ_{S_W} | τ_{L_W} | τ_{α_2} | τ_{χ_4} | τ_{S_W} | τ_{L_W} |
| PB | 0.7 | 0.75 | 0.83 | 0.78 | 0.95 | 1.1 | 1.11 | 1 |
| PPO | 0.68 | 0.77 | 0.7 | 0.77 | 0.84 | 1.03 | 1 | 0.88 |
| PEO | 0.8 | 0.76 | 0.72 | 0.88 | 0.94 | 0.95 | 0.97 | 1.1 |
| IL-A | 0.73 | 0.69 | 0.84 | 0.81 | 0.91 | 0.92 | 0.88 | 0.87 |
| IL-CR | 0.82 | 1.02 | 0.86 | 0.91 | 0.84 | 0.96 | 1.01 | 0.97 |
| IL-CC | 0.815 | 0.89 | 0.77 | 0.72 | 0.93 | 1.04 | 0.92 | 0.8 |
| Water | 0.8 | 0.96 | 0.86 | 0.82 | 1.01 | 1 | 0.96 | 0.89 |
| SiO ₂ | 0.77 | 0.91 | 0.77 | 0.94 | 0.71 | 0.82 | 1 | 0.94 |
| Dzugutov | 0.67 | / | 0.63 | 0.64 | 0.87 | / | 0.78 | 0.79 |
| HS MCT | 0.74 | / | / | / | 0.92 | / | / | / |
| LJ 50:50 | 0.7 | 0.98 | / | / | 1.36 | 1.37 | / | / |
| LJ 80:20 | 0.6 | / | / | / | 0.68 | / | / | / |

Table 4.3.: Slopes for SHD scaling corresponding to Fig. 4.8 and 4.9. Obtained within this study partly with data of previous studies.¹²

¹² Literature data: SiO₂ [23], LJ(50:50) [15, 166], LJ (80:20) [10, 13, 167, 168]{with Argon parameter $t = 0.3$ ps, $\sigma = 2.47$ Å [15]}, Dzugutov [17, 169], HSS MCT [33]

¹³ see also Sec. 3.3.1 and therein specifically Fig. 3.6

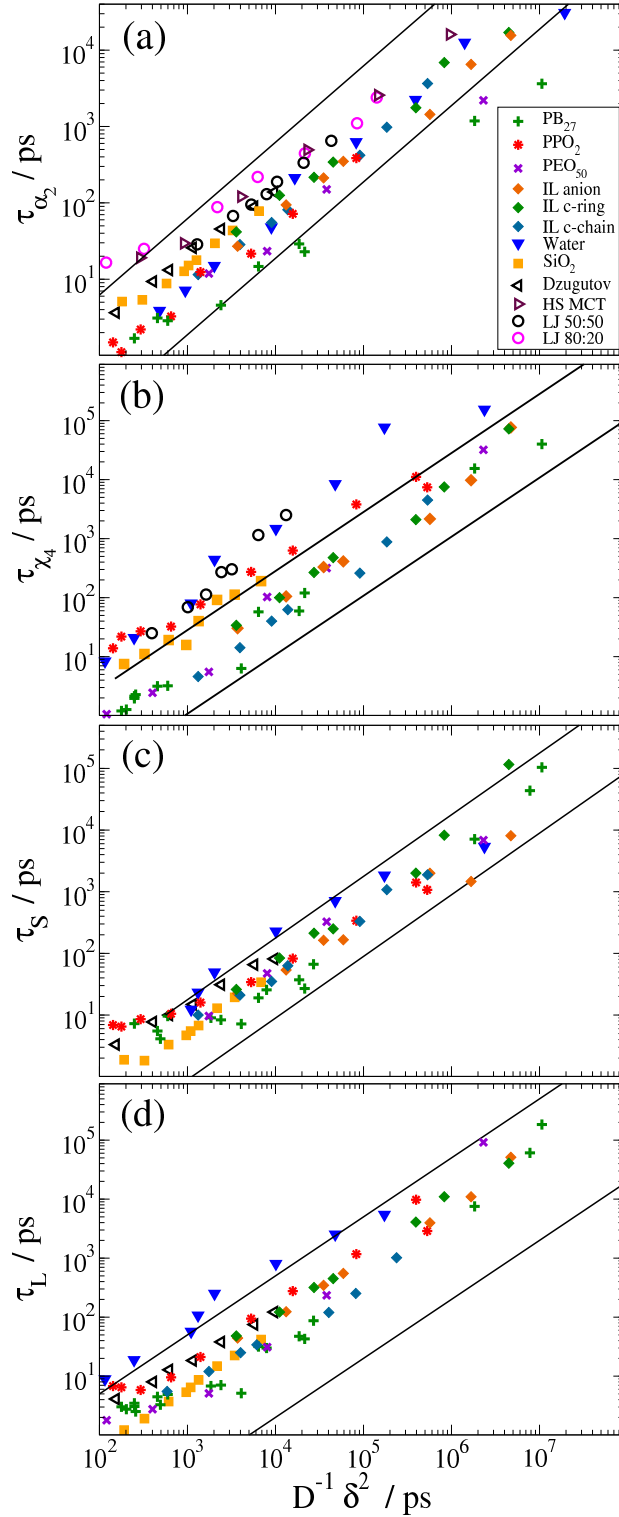


Figure 4.10.: The maximum times of the dynamic heterogeneities a) non-Gaussian parameter α_2 , b) 4-point-density-correlation χ_4 , c) mean cluster size S_w , d) mean string length L_w as a function of the inverse diffusion coefficient scaled by the jump length $D^{-1} \cdot \delta^2$.¹⁴

4.4 The Breakdown of the Stokes-Einstein Relation

We have seen that the characteristic times of SHD yield a description of the structural relaxation and the diffusion in the form of a power law. While a power law with an exponent of about 0.75 was found for scalings with τ_α , scalings with D yielded nearly perfect correlation with an exponent of 1. Hence, direct comparison of the two dynamic properties is of interest.

In Fig. 4.11 we present the diffusion coefficient D as a function of the structural relaxation time τ_α and the temperature T in a logarithmic plot. The SE relation in this form is given by

$$\log 10(D) = -1 \cdot \log 10(\tau_\alpha/T). \quad (4.13)$$

The fractional SE relation leads to

$$\log 10(D) = \xi_{SE} \cdot \log 10(\tau_\alpha/T). \quad (4.14)$$

This means, we can identify deviations from the SE relation based on the slope ξ_{SE} . We find that the relation is fulfilled for SiO_2 , the MCT calculations for an HS system, and high temperatures of the polymer systems. Upon cooling, the SE relation breaks down and a fractional exponent $\xi_{SE} < 1$ emerges. This exponent varies among the systems and hence could be a characteristic parameter for each system. In order to ensure better visibility within Fig. 4.11 we have not shown all data but provide the relevant parameters ξ_{SE} comprised in Tab. 4.4. The table reveals that the exponent decreases in value for increasing polymer chain lengths, whereas it is in a comparable range ≈ 0.8 for most molecular systems. Specifically, for the IL it shows that for all three evaluated atoms the same relation holds.

Fig. 4.12 furthermore illustrates the breakdown of the SE relation via $D\tau_\alpha/T$ and alternatively $D\tau_\alpha$ as a function of τ_α . If either the classic SE relation or a modification without T were valid, the result would be a constant value. In Fig. 4.12, however, we observe increasing curves for $D\tau_\alpha/T$ and $D\tau_\alpha$ so that the SE breakdown is clearly identified.

The fractional Stokes-Einstein exponent ξ_{SE} is a system-characteristic constant, which describes the breakdown of the SE relation and thereby the

¹⁴ Literature data: SiO_2 [23], LJ(50:50) [15, 166], LJ (80:20) [10, 13, 167, 168], Dzugutov [17, 169], HSS MCT [33]

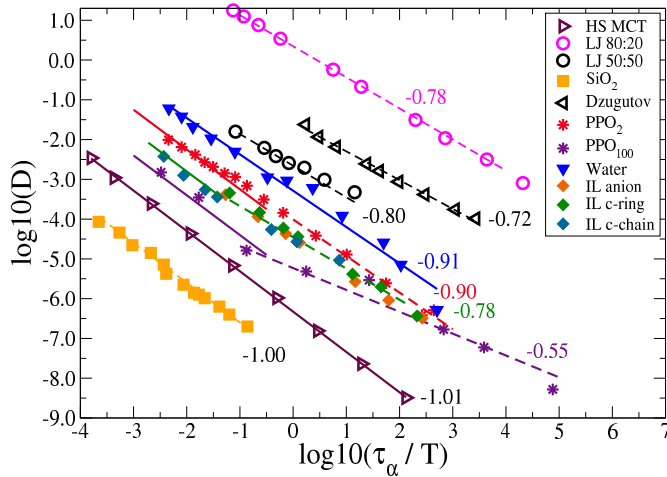


Figure 4.11.: The translational diffusion coefficient D as a function of the structural relaxation τ_α and temperature T , reveals the breakdown of the Stokes-Einstein relation, here indicated by a slope of 1 (solid lines). At low temperatures a power law with exponent ζ_{SE} describes the data. Here, D is in units of nm^2/ps , τ_α in ps and T in K. (LJ Systems shifted up by two decades, water up 1 decade, SiO_2 down by two decades, MCT without T).

| System | ζ_{SE} | System | ζ_{SE} |
|--------------------|--------------|----------------|--------------|
| PB ₂₇ | -0.74 | IL-anion | -0.78 |
| PB ₂₇₅ | -0.68 | IL-CR | -0.78 |
| PPO ₂ | -0.90 | IL-CC | -0.78 |
| PPO ₃ | -0.86 | Water | -0.90 |
| PPO ₉ | -0.80 | SiO_2 | -1.00 |
| PPO ₃₆ | -0.66 | Dzugutov | -0.72 |
| PPO ₁₀₀ | -0.55 | HS MCT | -1.01 |
| PEO ₁₂ | -0.75 | LJ 50:50 | -0.80 |
| PEO ₅₀ | -0.70 | LJ 80:20 | -0.78 |
| PEO ₁₅₀ | -0.67 | | |

Table 4.4.: Fractional Stokes-Einstein exponents ζ_{SE} from fits analogous to Fig.4.11.

evolution of the structural relaxation. The phenomenon was previously connected to the glass transition or for water to artifacts of a liquid-liquid phase transitions [134]. The SE breakdown in context of the glass transition describes a broadening of the distribution of relaxation times, which

results in a divergence of the time average and the rate average. The calculated average time τ_α is rather sensitive to contributions with a long relaxation time. The diffusion coefficient, however, is sensitive to the relation rate and will be dominated by fast relaxation or large relaxation rates. Therefore, it is intuitive that the averages of the quantities differ for any single temperature. If the underlying distribution of relaxation times was a log-Gaussian distribution this effect must not necessarily yield a fractional SE exponent. For a log-Gaussian distribution of relaxation times the relation between rate-average D and time-averaged τ_α can be linked to the width parameter σ of the distribution [173]

$$\log(\tau_\alpha D) \sim \sigma^2. \quad (4.15)$$

Hence, it would be reasonable to discuss $\log(\tau_\alpha D)$ as a constant rather than the SE relation, when the width of the distribution is constant. In the picture of a log-Gaussian distribution of relaxation times the breakdown is thus associated with a change in the temperature dependence of the distribution width σ . Specifically, for the present observation, this means that the evolution of the rate average is weaker than that of the time average. Hence, the fast relaxation times experience a weaker temperature dependence than the slow relaxation times. Unfortunately, the distribution of relaxation times cannot be calculated in an unambiguous way, because a Laplace transformation is not defined distinctively. Moreover, the considerations above are made under the assumption that all relaxation times contribute as a single-exponential decay, whereas a stretched exponential cannot be ruled out.

Another indicator which measures the shape of the underlying distribution of relaxation times is the stretching parameter β of the stretched exponential decay of the scattering function. Assuming a single relaxation corresponds to an exponential decay, the stretched exponential decay reflects the distribution of relaxation times. In contrast to ξ_{SE} , β is a temperature dependent parameter. However, it has been found in various studies [38, 80] that a constant stretching can be found at sufficiently low temperatures. This temperature-independence of β at low temperature contradicts the picture of continuous broadening in the distribution of relaxation times. In this work we cannot clearly distinguish the possible features of the underlying distribution so that we just discuss the accessible observables. In Fig. 4.13 we therefore present the low temperature value β as a function of the fractional SE exponent ξ_{SE} . For all available systems we find a clear correlation between the two parameters. For systems with

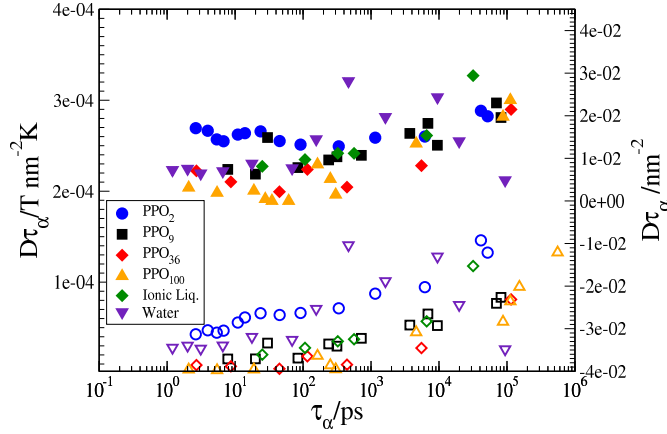


Figure 4.12.: The translational diffusion coefficient D the structural relaxation τ_α and temperature T , reveal the breakdown of the Stokes-Einstein relation, here indicated by the deviation from $D\tau_\alpha/T = \text{constant}$ (open symbols). Moreover, the relation $D\tau_\alpha = \text{constant}$ appears to hold just as well or even better for PPO₂ at low temperatures (full symbols).

mildly stretched exponential decays almost no or minor deviations from the SE relation are found, while systems with extremely stretched correlation decays experience severe deviations from the SE relation. These results are found for a variety of chemically different systems, as well as under variant chain lengths included in the polymer data.

Here, we have discussed the structural relaxation defined by the incoherent scattering function for a specific scattering vector $q = |\vec{q}|$. Naturally, the scattering vector as a choice of a relevant length scale controls the resulting correlation times τ_α and subsequently influences the determined β and ξ_{SE} . In order to ensure the above findings are consistent independently of the chosen inverse length scales q , we have investigated four additional scattering vectors $q = 24.0, 12.0, 7.13$ and 3.9 nm^{-1} for the exemplary systems PPO₂ and PPO₁₀₀. For each of them the fractional SE relation was evaluated to determine ξ_{SE} . Furthermore, we determined the respective stretching parameters β at low temperatures. The results for the studied values of q are included in Fig. 4.13 in a separate legend as \times and $+$. Clearly, the results for various q are consistent with the data so that we can interpret the correlation found between β and ξ_{SE} as q -independent. In detail, the correlation found reflects that the structural relaxation on large length scales occurs less stretched and with a less

prominent SE breakdown. The larger the considered length scales is the more single particle reorientations are included in it, which yields a narrower distribution for the relaxation times for larger length scales. The significance of the temperature-dependent width of the distribution, thus, decreases and β just as ξ_{SE} converge towards their ideal values.

Additionally, we have investigated which effect the choice of the incoherent scattering function for the characterization of the structural relaxation has. For this purpose we have defined the structural relaxation via the correlation of the backbone vectors $F_2(t)$ and extracted $\tau_{\alpha,rotation}$. In analogy to Fig. 4.11 we then defined a rotational SE exponent from the temperature dependence of the relation between translational diffusion constant and $\tau_{\alpha,rotation}$. It is important to note the difference to the Stokes-Einstein-Debye relation at this point, which describes the relation between rotational diffusion and rotational autocorrelation times. The inset of Fig. 4.13 illustrates the similar information content of ξ_{SE} and $\xi_{SE,rot}$. Consequently, we have shown that the SE exponent and its relation to dynamic heterogeneity is a common feature of glass formers.

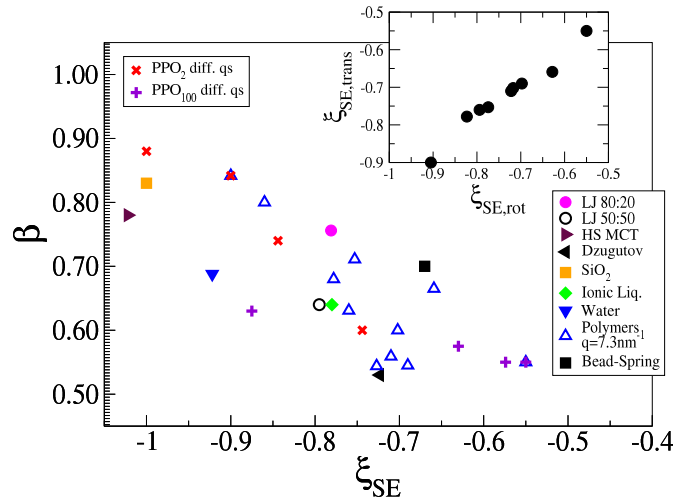


Figure 4.13.: Stretching factor β of the α -relaxation measured by incoherent scattering function as a function of the exponent of the fractional SE relation. The representation reveals a strong correlation for a variety of supercooled fluids (Hard sphere [33], SPC/E [113], Dzugutov [17], Bead-Spring [174–176]). The inset shows the rotational and translational SE exponents.

Moreover, we want to address the relation between the SE exponent and SHD by way of example for the non-Gaussian parameter $\alpha_2(t)$. In the previous section we have seen that the diffusion coefficient and the characteristic time τ_{α_2} are well correlated for most systems. Here, we are interested in quantifying the strength of the heterogeneity itself. Intuitively, this has been done with the peak-height maximum value of the $\alpha_2(t)$ peak ($\alpha_{2,max}$) for most SHD indicators [13, 15, 164, 177, 178]. Unfortunately, $\alpha_{2,max}$ just like τ_{α_2} is a temperature-dependent parameter. Thus, we present the maxima $\alpha_{2,max}$ as a function of the inverse diffusion coefficient D^{-1} in Fig. 4.14. The results show that the maxima $\alpha_{2,max}$ increase upon the slow-down of dynamics as expected. This means, the deviations from a Gaussian distribution of particle displacements increase approaching the glass transition. For a comparison with the exponent ξ_{SE} , however, we need a single characteristic parameter of the presented effect. For this purpose we have determined the $\alpha_{2,max}$ for different isokinetic points of similar D^{-1} , the curvature of the data and the low temperature plateau via a fit. Unfortunately, we cannot find any reasonable connection between ξ_{SE} and any of these features of $\alpha_{2,max}$ that holds for the complete range of the available systems. These findings are unexpected because β as a very simple indicator has demonstrated a very prominent correlation. The peak height of SHD indicators is commonly expected [13, 15, 164, 177, 178] to increase strongly upon approaching the glass transition and is therefore often discussed as an indicator for the glass transition. Specifically, $\chi_4(t)$ as a susceptibility is expected to diverge [15, 164, 177, 178] at a critical point, while cluster and string sizes are expected to change corresponding to changing length scales.

After two contrary findings regarding the correlation of ξ_{SE} with SHD and the unexpectedly uncorrelated behavior of $\alpha_{2,max}$ we must ask whether the peak height of $\alpha_2(t)$ is a good indicator after all. The broad peaks found for all SHD indicators are not only characterized by their height and position, but also by their width. Quantification of the non-Gaussian behavior within a system simply by its peak maximum might not include all relevant information. Intuitively, a high narrow peak and a low broad peak might induce the same “amount” of non-Gaussian dynamics. While this picture implies the area under the peak as the relevant parameter, we will consider just the width of the $\alpha_2(t)$ peaks. In Fig. 4.15 we present the non-Gaussian parameter $\alpha_2(t)$ for several systems at an isokinetic point defined by a diffusion coefficient $D \approx 5 \cdot 10^{-7} \text{ nm}^2/\text{ps}$. In order to allow a comparison solely on the basis of the peak width, we have normalized the

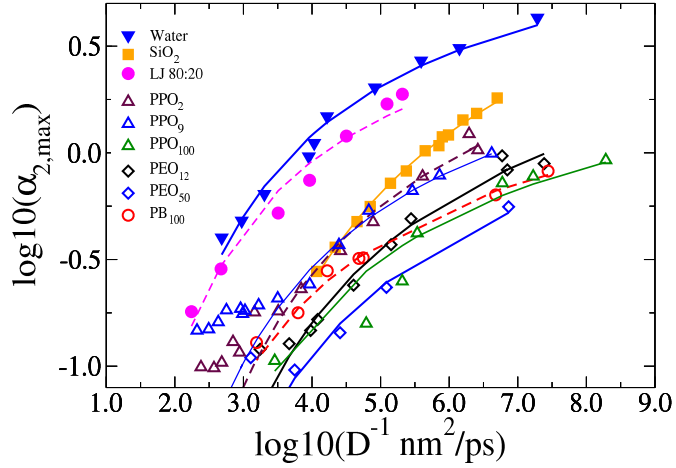


Figure 4.14.: The maximum of the non-Gaussian factor α_2 as a function of the inverse diffusion coefficient D^{-1} converges towards a maximum approaching low temperatures. Lines are presented as guidelines for the eye revealing converging maxima.

x- and y-axis with the peak position τ_{α_2} and height $\alpha_{2,max}$. The resulting representation clearly demonstrates a connection between the peak width and the complexity of the system. While for the model systems LJ, HS MCT, and SiO_2 $\alpha_2(t)$ exhibits a symmetric Gaussian peak shape, increasing complexity for the water and polymer systems broadens the peak, resulting in strong asymmetry. In order to quantify this effect we introduce the full width at half maximum (FWHM) value and compare the findings with the SE exponent ξ_{SE} . The result is shown in the inset of Fig. 4.15 and reveals a correlation between the two parameters. Hence, we have found a new observable, the peak width of SHD, which is correlated to ξ_{SE} and describes a feature of the glass transition.

In this section we have defined the fractional Stokes-Einstein exponent ξ_{SE} for a variety of systems, both calculated from data from previous studies [10, 13, 15, 17, 23, 33, 166–169] and our own data. The thereby determined ξ_{SE} have not been reported to our knowledge so that this study is the first to report such data in a comparative study of several glass formers. Notably, we have found that ξ_{SE} is correlated with the stretching of the correlation function and a new aspect of the non-Gaussian parameter. The here proposed and conducted analyses of SHD peak widths in form of the FWHM have, to our knowledge, also not been introduced in previous

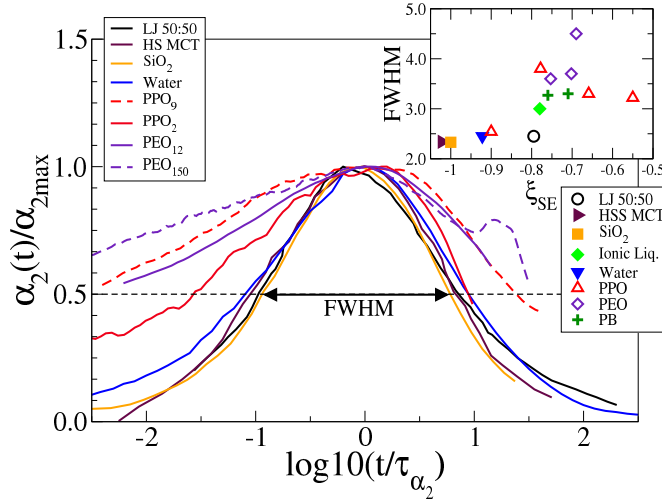


Figure 4.15.: The non-Gaussian parameter $\alpha_2(t)/\alpha_{2,max}$ normalized by its maximum value as a function of the reduced time t/τ_{α_2} at an isokinetic point defined by $D \approx 5 \cdot 10^{-7} \text{ nm}^2/\text{ps}$. With increasing complexity of the systems the Gaussian form of $\alpha_2(t)$ broadens asymmetrically. The inset presents the FWHM of the curves as a function of the corresponding fractional exponent ξ_{SE} , revealing a significant correlation.

studies and are an interesting new feature worthy of investigation in future studies.

4.5 Dynamic Facilitation

We ascertain the Dynamic Facilitation (DF) theory [9, 48–51] as suggested in previous studies [23, 56] in a direct analysis of its key feature, the facilitation of enhanced dynamics in spatial proximity to highly mobile particles. In contrast to the investigation of universal features of the glass transition in the previous sections, we will here apply an analysis specifically designed for the evaluation of DF. For the DF model we may ascertain two predicted features. The dynamic domains proposed in DF should scale with $\sqrt{\tau_\alpha}$ [9, 49] and formerly immobile particles have a greater chance of becoming mobile, when they reside in proximity to a mobile particle.

Specifically, the latter can be determined using a higher order correlation function. We thereby analyze two different particles each at two separate time intervals $\tau_{1 \rightarrow 2}$ and $\tau_{2 \rightarrow 3}$ in analogy to Refs. 23, 56. In these two

time intervals we look for a particle that is highly mobile in $2 \rightarrow 3$ and not highly mobile $1 \rightarrow 2$. After the new highly mobile particles have been identified they are connected with the minimal distance to a highly mobile particle at the transition time 2. The result is the probability distribution $P_F(r, t)$ of finding a non-mobile particle in interval $1 \rightarrow 2$ with minimum distance r to all mobile particle in $1 \rightarrow 2$ that becomes mobile in $2 \rightarrow 3$. The upper left inset of Fig. 4.16 presents a resulting probability distribution $P_F(r, t)$ in comparison to the distribution for randomly chosen particles $P_F^*(r, t)$, which of course can also reside near a highly mobile particle. This definition of DF is sensitive to the chosen time interval t , which we have chosen symmetrically so that $\tau_{1 \rightarrow 2} = \tau_{2 \rightarrow 3} = t$. For each length of these back-to-back time intervals we have hence calculated distance profiles of DF $P_F(r, t)$. In order to quantify the DF part of the profile we put the DF part in relation to the random part and calculate the area of the first peak normalized by the area of the random part as suggested in Refs. 23, 56.

$$F_c(t) = \frac{\int_0^{r_{min}} P_F(r, t) dr}{\int_0^{r_{min}} P_F^*(r, t) dr} \quad (4.16)$$

The result is an indicator for the relevance of DF. When $F_c(t) > 1$ the DF mechanism contributes to relaxation, whereas for $F_c(t) = 1$ the mechanism is statistically insignificant. $F_c(t)$ is a function of the chosen back-to-back time interval length t and exhibits a time dependence similar to SHD indicators. In the main panel of Fig. 4.16 we see the temperature dependence of $F_c(t)$ for PPO₂ at low temperatures. As the temperature range already indicates the contributions of DF can only be measured at very low temperatures and even here only yield very small values. We see that the chances of dynamic facilitation are just 10% higher than spontaneous occurrence of high mobility.

However, we observe there is a characteristic time τ_F , where the dynamic facilitation occurs most prominently and shifts towards longer times upon cooling, while the maximum value $F_{c,max}$ moderately increases. The upper right inset of Fig. 4.16 presents the characteristic peak time τ_F as a function of τ_α in analogy to the scaling plots in Sec. 4.3. This representation is the first to extend the formerly introduced scaling to τ_F . In addition to our own simulation of PPO₂ and the ionic liquid we have calculated values for water data provided by F. Klameth [1] and extracted the relevant data from Refs. 23, 56 for SiO₂ and the Dzugutov model. Unfortunately, we could not calculate any significant data for any of the longer polymers,

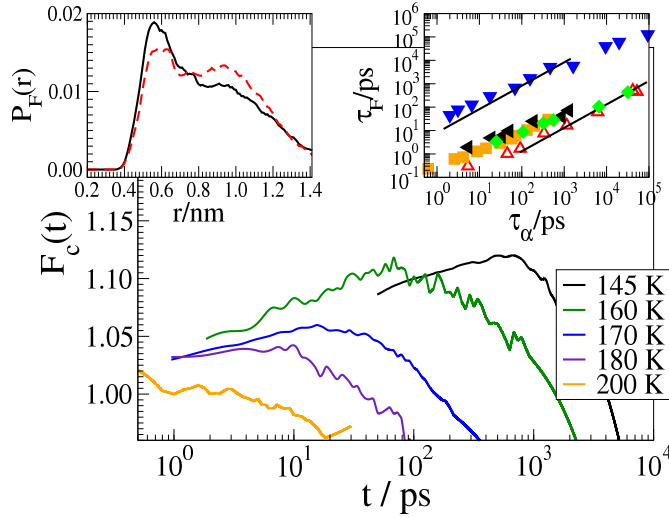


Figure 4.16.: The dynamic facilitation strength $F_c(t)$ for the central carbon atom in PPO_2 . Upper left panel probability distributions $P_F(r, t)$ (solid) and $P_F^*(r, t)$ (dashed). Upper right panel characteristic facilitation time τ_F as a function of the relaxation time τ_α , solid line represents a slope of $3/4$. Symbols are analogous to Fig. 4.17 referring to PPO_2 , Dzugutov [56], water and SiO_2 [23].

where the DF model fails due to an enhanced distribution of the dynamics via the covalent bonds along the chain. For the available data though we find that all four systems follow a power law $\tau_F \sim \tau_\alpha^\nu$ with the common slope $\nu = 0.75$ known from the previous section.

In one of the previous studies it was shown that the DF strengths measured by the peak maximum $F_{c,max}$ for a Dzugutov model [56] and for SiO_2 [23] follow a common trend. In Fig. 4.17 we find that our data for water exhibits almost a constant strength $F_{c,max}$, while the ionic liquid along with the polymer exhibit a significantly weaker dependence of the time scale. Hence, we can neither support the found scaling, nor are we able to explain the findings in detail. It is intuitive to assume water as a molecular liquid will experience a stronger DF than the IL and the polymer, which include more, e.g., intramolecular interactions. Yet, we do not understand the behavior of water in comparison to SiO_2 .

Finally, we inspect the prediction of DF that the size of dynamic domains scales with $\sqrt{\tau_\alpha}$. So far, our analysis of DF has not clearly defined the do-

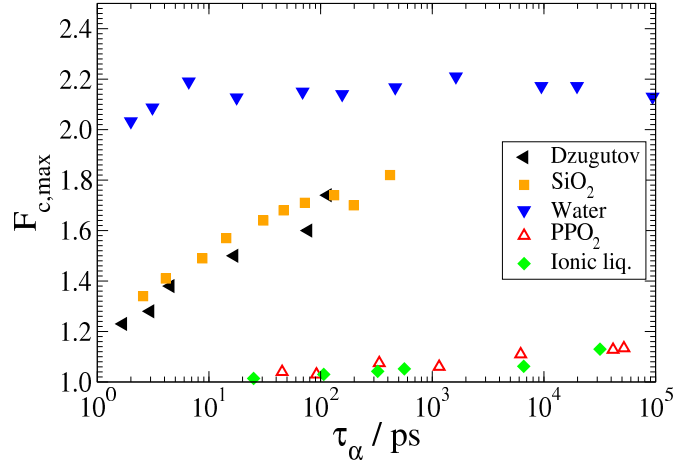


Figure 4.17.: The maximum of the dynamic facility strength $F_{c,max}$ as a function of the structural relaxation time τ_α . (With Dzugutov [56] and SiO_2 [23] from previous studies.)

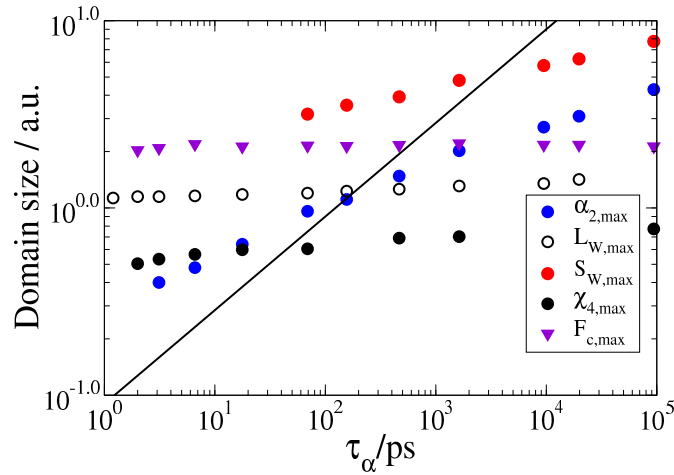


Figure 4.18.: The maximum of α_2 , χ_4 , S_w , L_w and F_c as a function of the structural relaxation analyzed for the water data provided by F. Klameth. The solid line represents the domain growth within the DF model with $\sqrt{\tau_\alpha}$.

main size neither will we try this here. Yet, we can utilize all previously shown findings and compare all introduced SHD indicators to the proposed scaling. Assuming the domain size refers to the maxima of the calculated parameters, we present the maxima of non-Gaussian parameter, weight-averaged dynamic string length ($L_w(t)$), weight-averaged dynamic cluster size ($S_w(t)$), 4-point density correlation function ($\chi_4(t)$) and indicator for

significant contribution of dynamic facilitation ($F_c(t)$) as a function of τ_α in Fig. 4.18. The solid line represents the proposed scaling $\sqrt{\tau_\alpha}$. We have chosen to show the data for the water system, where F. Klameth provided the raw data and we conducted the concrete analysis. We observe that neither of the here presented definitions resemble the proposed scaling.

For the DF theory we hence find only weak influences in general and none specifically for complex systems, e.g., polymers. Interestingly, the universal time scaling found previously is found once more for DF observables. Yet, domain size scaling could not be found and the model itself is not a promising approach for a complete description of the glass transition in all classes of systems.

4.6 Summary

In this chapter we have addressed the description of the slowdown of dynamics approaching the glass transition and found various possibilities for valid control parameters. Volume scalings with an exponent γ yield very good master curves for variant pressure and temperature and partly chain length. Simple explanations by the softness of the repulsive potential fail for systems with complex intramolecular interactions.

Approximation of the configuration entropy by Green's entropy expansion allows S_{conf} to be calculated and the glass transition to be described in the framework of Adam-Gibbs theory. Characteristic times of spatially heterogeneous dynamics are described by a power law as a function of the structural relaxation time and the diffusion coefficient with common exponents $\nu_{\tau_\alpha} = 0.75$ and $\nu_D = 1.0$ for a wide range of glass forming systems both extracted from previous studies and our own work.

We find that a breakdown of the Stokes-Einstein relation occurs in most glass formers and determine formerly unknown fractional exponents, which are closely related to the heterogeneity of dynamics indicated by the stretched exponential decay of the correlation function and the peak width of the non-Gaussian factor. Specifically, with the introduction of the peak width as an interesting parameter we have proposed a new analysis.

We have characterized Dynamic Facilitation by specifically designed observables [23] and found no measurable effects for polymer chains and the ionic liquid along with only weak influences on the dimer PPO₂ but

strong influences for water. The Dynamic Facilitation theory as a universal description of the glass transition can not be supported because its mechanism has only minor influence in some systems and does therefore not describe the complete class of glass forming liquids.

In this chapter we have discussed several scalings for the structural relaxation. Thereby, we have identified strong relations with volume influences, the configuration entropy, spatially heterogeneous dynamics and the breakdown of the Stokes-Einstein relation. All of these scalings were found to describe a wide range of glass formers. Unfortunately, all of them introduce new fit parameters such as the exponents γ , ν or ξ_{SE} , while allowing us to extend the description to master curves for variant temperature, pressure and polymer chain length.

5 Confinement Systems

In the previous chapter we have discussed the existence of spatially heterogeneous dynamics (SHD) in glass formers. Supporting previous studies [10–24], we thereby identified SHD as a key feature of the glass transition, which experiences a strong increase approaching the glass transition, thus describing the evolution of the structural relaxation and diffusion coefficient. Specifically, the picture of cooperatively rearranging regions (CRRs) within the Adam-Gibbs (AG) theory has sent us on a quest for the definition of length scales related to these dynamic regions. The nature of these regions along with their specific size is of interest in order to decide which theory applies best.

While the AG picture of the CRR is primarily dynamic, the Random First Order Transition (RFOT) approach also introduces static concepts. The mosaics in RFOT are dynamic regions just as in the AG theory, but the introduction of the surface tension and clearly defined surface limits between two regions give them static properties. The entropic droplets in RFOT are formed with a temporary static size and the surface tension as a result of persisting droplet structure.

We have so far observed SHD under different conditions, but were not able to study their effects in an isolated and clearly controlled way. Application of confinements here gives us the opportunity to implement well-defined SHD in the form of completely immobile particles. The most powerful possibility for MD simulations thereby is the construction of “neutral” confinements. Whereas for an experiment, a confinement comprised of, e.g., a silica pore needs to be introduced, in MD simulations we can freeze some of the molecules of the bulk system and construct any desired geometry. The created confinement is considered to be a neutral confinement because it does not introduce new interactions between confining atoms and the confined liquid. In experiments [179, 180] new interactions were inevitably introduced so that the dynamics are changed compared to the bulk system. Of course, it may be of interest to study the specific behavior of a supercooled liquid in a pore. In the present study, however, we are interested in glassy dynamics and therefore use the confinement as a tool, which is not supposed to introduce new system features, but rather to unravel inherent features of the bulk system.

In this chapter, we will systematically vary the average distance between pinned particles and liquid particles and observe the changes of the systems compared to the bulk system. The confinement length scale thereby imprinted on the system is well-defined and allows us to observe the interference of imprinted length scale and bulk inherent length scales. In other words, when we observe a dramatic change of the bulk behavior we assume the bulk length scale is reached.

This approach has so far been applied to simple systems such as binary hard-sphere [60, 61], soft-sphere [62], harmonic-sphere [63, 64], Lennard-Jones mixtures [58, 59] or bead-spring oligomers [65] and is widely discussed in the relevant literature. In these previous studies it was possible to define a static length scale ξ_s , [58–65, 181–185] as well as a dynamic length scale ξ_d , [186–190] with this method. Here, we will contribute data for PPO₃ along with data from Felix Klameth for water. The complete data for the water system along with the PPO₃ data for the random pinned confinement has been published in Ref. 1. In the following, we show the published data along with three complementary confinement systems of PPO₃. Thus, we provide the first reports for realistic, atomistic glass formers, complementing the previous results for simple model systems.

To determine whether a meaningful length scale corresponding to a bulk property is obtained, we investigate different geometries of the confinement. The procedure is supposed to yield reasonable data for different confinement geometries within certain limits so that inherent effects of the confinements may be neglected. Four different types of geometry (slit, spherical, spherical inverted, random pinned) will be investigated, to make sure only geometry-independent conclusions can be drawn.

We will introduce an overlap correlation function, which has proven to be a useful tool to ascertain the effect of pinned particles on the configuration of unpinned particles [58–65, 182–185]. The overlap correlation function enables us to observe the development of an “amorphous order” approaching the glass transition, which yields a static correlation length ξ_s , [59–65]. In addition, the well-known concept of the incoherent scattering function provides us with a dynamic definition of a length scale. The concepts of static and dynamic length scales have thereby been reported to decouple in some scenarios, while yielding good descriptions of the struc-

tural relaxation of the bulk in other cases.

5.1 Confinement Details

For the proposed approach we implemented four different types of confinements for the PPO_3 system at temperatures between 450 and 200 K illustrated in Fig. 5.1. In detail, all systems were taken from fully equilibrated bulk systems and fixed to their bulk volume. From this equilibrium state whole molecules were chosen to be pinned with the freeze groups option of the GROMACS simulation package [98–100]. With self-scripted programs liquid and pinned sub-ensembles were defined based on the center of mass position of the molecules in an index file for the program to run. The resulting trajectory was then, with the help of the index file, analyzed for the liquid molecules and with respect to the closest distance to any pinned particle.

The particles were pinned into a sphere of radius 2.55 nm leaving a confining matrix of hard spheres in a melt, which we will refer to as the inverse spherical (IS) confinement (see upper left Fig. 5.1). The spherical (S) confinement of the same size is prepared the same way (see upper right Fig. 5.1). Furthermore, we pinned a wall fully extending over two dimensions via the periodic boundary conditions with a thickness of about $d_{wall} = 1.5$ nm into the third dimension. With the boundary conditions this yields a slit (SL) confinement of slit width $d_{slit} = 5.5$ nm. Finally, in the fourth type of confinement, which we refer to as random pinned (RP) confinement, a statistically chosen fraction f of molecules is pinned to its position (see lower right Fig. 5.1). Here, a single confinement for one temperature does not suffice to get evaluations of variant distance parameters. The fraction f of the pinned particles is varied between $f=0.1$ and $f=0.9$ and the distance parameter is defined as the average distance to a fixed particle

$$d_{RP} = 0.5(f\rho)^{-1/3} \quad (5.1)$$

with particle density ρ . In the analyses for the other three systems, we distinguish particles in the liquid parts according to their closest distance to a pinned particle.

For these studies of PPO_3 the temperature is varied between 450 K and

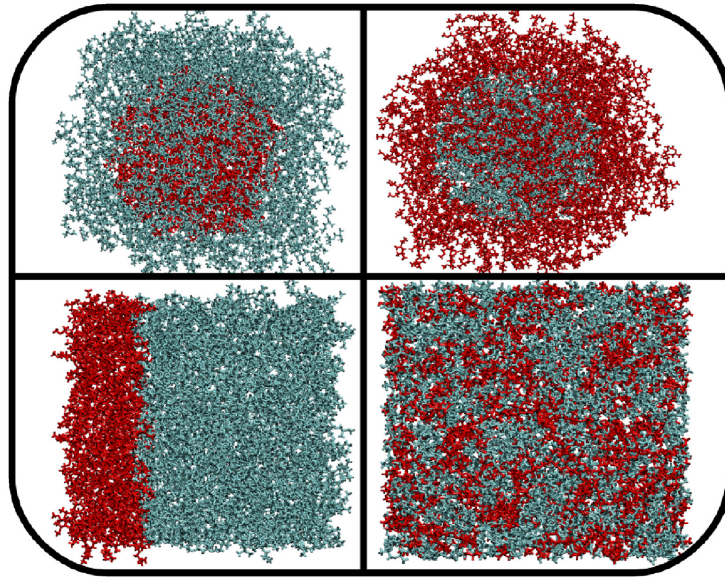


Figure 5.1.: Illustration of the pinned particle confinement systems for PPO_3 . Particles in red are pinned to their current positions, particles in blue are mobile following the interactions of the bulk force field. Upper left: Inverted spherical confinement of a fixed sphere $r = 2.55$ nm in a melt. Upper right: spherical confinement of a liquid drop in a pinned spherical confinement $r = 2.55$ nm. Lower left: Slit confinement, a wall of pinned particles results in a slit of size $d_{slit} = 5.5$ nm ($d_{wall} = 1.5$ nm) and creates a slit via the periodical boundary conditions. Lower right: Random pinned system, where a statistical fraction $f = 0.4$ of molecules is pinned. All systems are taken from a bulk simulation and were simulated at the bulk volume.

280 K at a pressure of 1 bar. The system size has been increased compared to the other bulk simulations referred to in the previous chapter to make sure the statistics for the evaluations are kept within a reasonable range, i.e., the number of particles is increased so that the liquid part yields statistics comparable to the bulk. We simulate a box of a size of about $(7\text{ nm})^3$ depending on the temperature, which contains 29696 atoms or 1024 whole molecules of PPO_3 . Details on the complementary study on water can be found in our joint publication [1], where the temperature range is lower, between 260 K and 200 K. Along with the comparable RP and SL geometries F. Klameth has therein studied water in two cylindrical pores of 1.5 nm and 2.5 nm, in the following referred to as water-15

and water-25. In the following, we will refer to the -SL, -S, -IS, -15, -25 systems as classic confinement systems because their geometry is experimentally accessible in contrast to RP systems, which are only accessible to MD simulations.

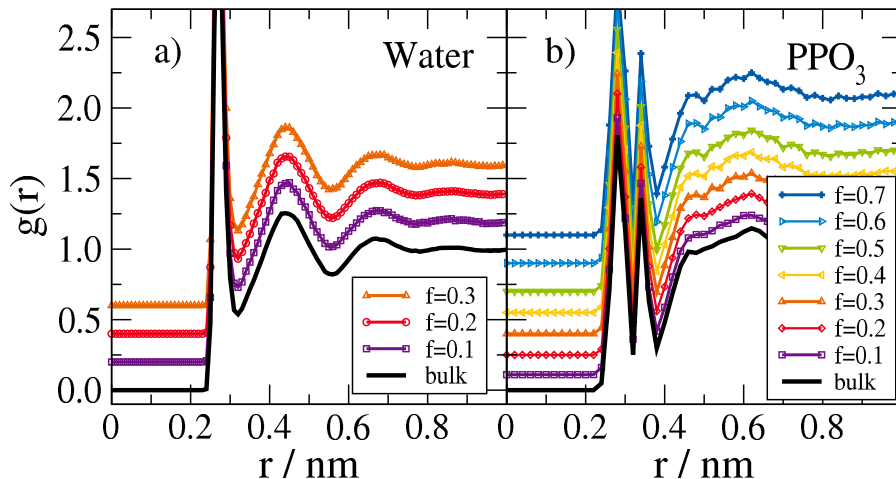


Figure 5.2.: The pair correlation function of the intermolecular oxygen atoms for (a) water from F. Klameth (240 K) and (b) PPO_3 (350 K) for several fractions of pinned particles. Random pinned data is shifted up to ensure visibility. The data shows that the structure of the liquids is not influenced by the confinement, so comparability with the bulk for all systems and the assumption of a neutral confinement is validated. The same results are found for the comparison with the other bulk geometries [1].

For all mentioned systems we ensured that the local structure of the systems does not change when the confinement is introduced or changed. In Fig. 5.2 the pair correlation function $g(r)$ for the RP systems by way of example shows unchanged local order for different fractions of pinned particles in water and PPO_3 . For the other geometries we also made sure the structure is basically identical.

5.2 Definition of Correlation Lengths

For the definition of length scales we will differ between dynamic and static correlation lengths, which are probed through different observables sensitive to single particle translation or ensemble structure.

5.2.1 Dynamic Correlation Length

We start with the calculation of the incoherent scattering function

$$F_s(q, t) = \langle \cos[\mathbf{q}(\mathbf{r}_i(t) - \mathbf{r}_i(0))] \rangle \quad (5.2)$$

and choose for both liquids a scattering vector $q = |\mathbf{q}|$ corresponding to the intermolecular oxygen-oxygen distance, yielding $q = 2.27 \text{ \AA}$ for water and $q = 1 \text{ \AA}$ for PPO₃. The concept of the incoherent scattering function was already introduced in the previous chapters and reflects the single particle displacements in a time window t observed on the length scale $|q|$. It yields a stretched exponential decay which upon cooling shifts towards longer times. Similar behavior is observed when the scattering function is calculated for different layers of the system with decreasing distance to the confinement molecules.

In Fig. 5.3(a), (c) and (e) on the left side, the results of the incoherent scattering function $F_s(q, t)$ are displayed for layers with different intermediate distances d to the confinement along with the corresponding bulk data. For all three confinement geometries the correlation function experiences increasing relaxation times and stretched-exponential behavior when approaching the pinned molecules. Molecules residing far away from the confinement $\approx 0.8 \text{ nm}$ resemble the known bulk behavior revealing a characteristic distance of influence originating from the pinned molecules of the confinement.

Comparable behavior is also found for the RP systems shown in Fig. 5.4. Here, we observe the influence of the pinned molecule fraction, which again leads to more stretched and delayed relaxation processes when the average distance to a pinned particle is decreased, here meaning the fraction of pinned particles is increased. In Fig. 5.4(a and c), in addition to the PPO₃ data we provide the corresponding water data from F. Klameth [1], which experiences comparable changes through the confinement.

For further evaluation we extracted the now distance-dependent characteristic relaxation times τ_α from the incoherent scattering function at a decay of $1/e$ so that $F_s(q, \tau_\alpha) = 1/e$. For each temperature this approach leads to a data set of distance parameter-dependent relaxation times as dis-

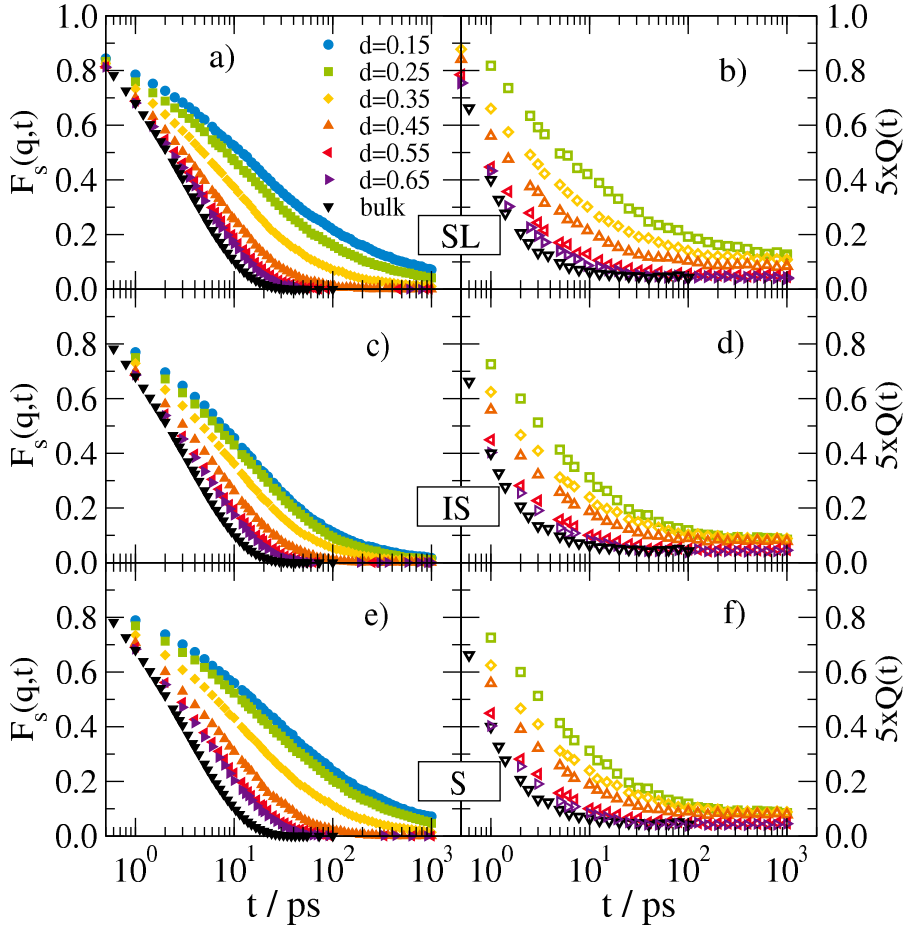


Figure 5.3.: Incoherent scattering function $F_s(q, t)$ (left) and overlap correlation function $Q(t)$ (right) for the PPO_3 system at 350 K evaluated for different layers with distance d to the confinement. First row (a,b) slit confinement (SL), second row (c,d) inverted spherical confinement (IS) and last row spherical confinement (S). Overlap correlation data are scaled up by a factor of 5. Approaching the confinement relaxation times and overlap plateau values Q_∞ increase.

played in Fig. 5.5. Reasonable description of the data is thereby achieved via the empirical relation [186–189]

$$\ln\left(\frac{\tau}{\tau_\infty}\right) \propto \exp\left(-\frac{d}{\xi_d}\right) \quad (5.3)$$

which yields the characteristic dynamic length scale ξ_d . This characteristic distance estimates the length up to which the bulk dynamics are perturbed

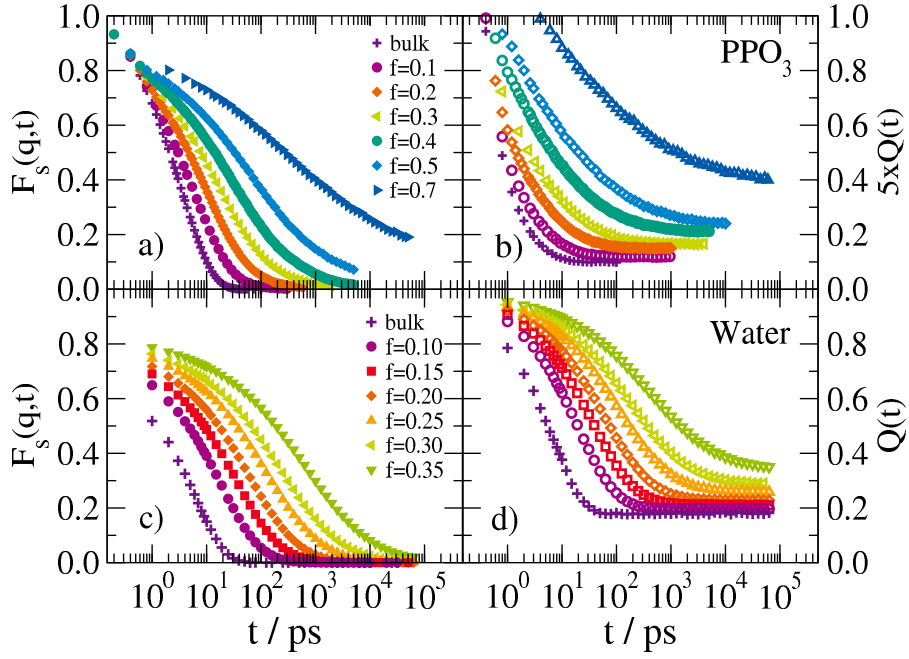


Figure 5.4.: Incoherent scattering function $F_s(q, t)$ (left) and overlap correlation function $Q(t)$ (right) for the PPO₃ system at 350 K (a and b) evaluated for random pinned systems with different pinned fractions $f = 0.1 - 0.7$ compared to comparable data on water from F. Klameth at 240 K (c and d) [1]. Overlap correlation data scaled up by a factor of 5 because cell size is chosen for water.

by the confinement. For the long-distance limit of the relaxation times τ_∞ the fit was set to the bulk values as indicated by the open symbols in Fig. 5.5.

The temperature-dependent results of the fit with Eq. 5.3 for all confinement geometries are given in Fig. 5.6(a). For the classic confinements with clear surface definition (SL, IS, S, 25, 15) the dynamic length scale ξ_d increases upon cooling forming a master curve for water and PPO₃ separately. The RP system here exhibits fundamentally different behavior. In both cases no temperature dependence is evident. The classic confinements produce the expected behavior associated with the theoretical pictures of growing CRR approaching the glass transition. The behavior of the RP systems on the other hand brings us to the conclusion that the RP system is another class of system which at least dynamically does not reproduce the bulk behavior upon cooling.

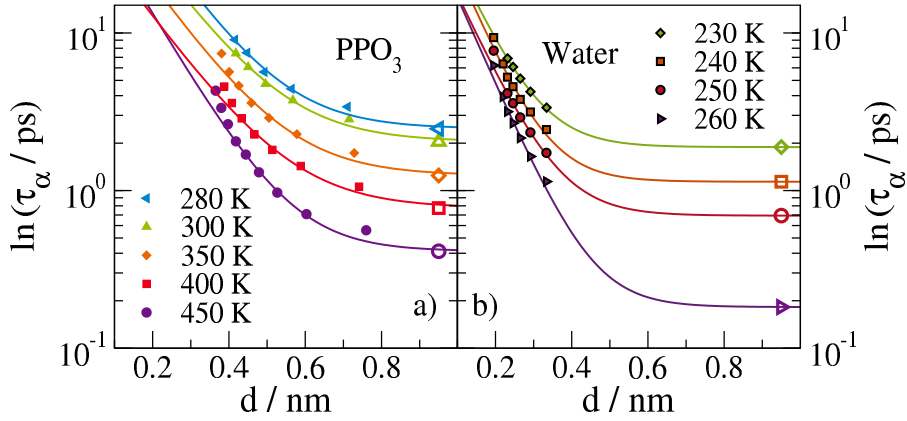


Figure 5.5.: Correlation times τ_α for the random pinned (RP) geometries of the (a) PPO₃ system and the (b) water system [1] as a function of the confining length d . Open symbols represent the corresponding bulk values and solid lines the fit according to Eq. 5.3.

In the introduction to this chapter we mentioned that the characteristic length scale we are looking for should describe the bulk behavior of the system and hence be independent of the confinement geometry. Excluding the RP system, the proposed length scales extracted for the 3 geometries of PPO₃ and water fulfill this demand and yield lengths within reasonable agreement.

5.2.2 Static Correlation Length

In addition to the changes of translational dynamics, confinements induce a static short range mean interaction field upon the liquid which may not be measured with dynamic observables. In order to measure these static influences we define the overlap correlation function

$$Q(t) = \frac{\sum_j \langle n_j(t) n_j(0) \rangle}{\sum_j \langle n_j(0) \rangle} \quad (5.4)$$

where $n_j(t)$ is 1 if cell j at time t is occupied and 0 if not. A small cell size of $(1 \text{ \AA})^3$ is chosen¹ to ensure the possibility of more than one oxygen atom occupying a cell is negligible.

¹ For the data in Ref. 1 we had chosen a cell size of $(0.5 \text{ \AA})^3$ for PPO₃ and $(1 \text{ \AA})^3$ for water. Here, without quantitative changes we adjusted the cell size.

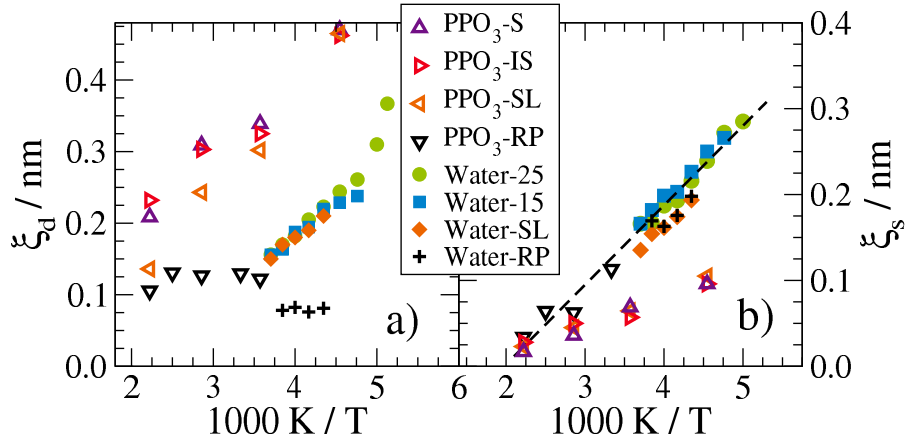


Figure 5.6.: Length scales obtained from four confinement geometries for each water [1] and PPO_3 as a function of the inverse temperature for (a) the dynamic correlation length ξ_d and (b) the static correlation length ξ_s .

The basic concept of overlap correlations is illustrated in Fig. 5.7. We measure the overlap of two particle configurations disregarding particle exchange. Characteristically, the overlap correlation function decays from a normalized value at $t=0$ to a finite value in the long-time limit $Q_\infty = Q(t \rightarrow \infty) > 0$. This long-time limit holds information about a static correlation and must be compared to the overlap between two randomly chosen configurations Q_{rand} as obtained from the bulk simulations. In Figs. 5.3 and 5.4 we have included the overlap correlation functions of the previously described systems of PPO_3 and water which, in contrast to the incoherent scattering function, experience long-time plateaus $Q_\infty > Q_{rand}$. In the center of the observed confinements we find good agreement with the bulk values whereas the static correlation increases towards the walls of the confinements. In the RP systems we similarly observe increasing static correlations when the fraction of pinned particles is increased. Apart from the emergence of the static plateaus, the decays dynamically shift towards longer times corresponding to the shift in the incoherent scattering function.

The results of the plateau evaluation from Figs. 5.3 and 5.4 are shown in Fig. 5.8. In panel (a) we present the plateau heights Q_∞ for the different geometries of PPO_3 and water [1] as a function of the confinement

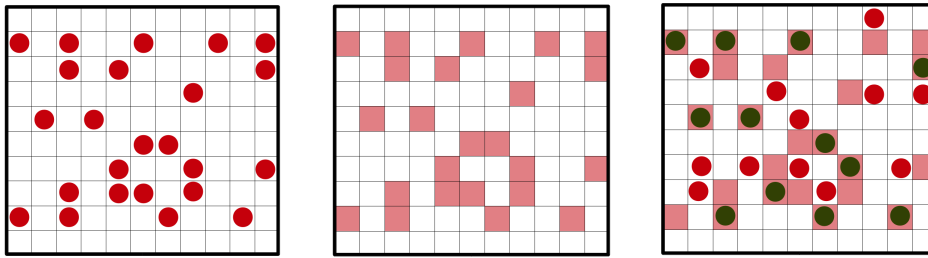


Figure 5.7.: Illustration of the principle of the overlap correlation function in two dimensions; actual implementation is in three dimensions. In step 1 (left) the space is divided into cells of volumes $(1 \text{ \AA})^3$. In step 2 we mark all cells that were occupied at a starting time frame $t=0$ (middle). At later times $t>0$ we then count all marked cells which are still occupied by any particle (right). After normalization with the number of marked cells the overlap correlation function yields a quantitative value characterizing to what extent the structure of $t=0$ is still present at $t>0$. On time scales larger than the structural relaxation time the correlation exhibits a plateau, which is a measure for the static structural correlations.

distance. Since the number of oxygen atoms in PPO_3 is smaller than in water and very small cell sizes were chosen the plateau values in PPO_3 are systematically and expectedly smaller. Alongside the presented data we calculated data for other cell sizes (0.5 \AA and 4 \AA) to ensure the chosen cell size does not influence the conclusions.

For both systems in Fig. 5.8(a) with increasing distance parameter we observe that the plateau value Q_∞ follows an exponential decay with slightly different slopes for the different geometries. While the classic confinements (SL, S, IS, 15, 25) are in good agreement with each other, the RP geometries, especially for water, experience a steeper decay. This observation is consistent with a previous study on a binary mixture of harmonic spheres, which also reported a steeper decay for RP geometries than for the classic ones [63]. The differences reported and confirmed here are expected because the RP geometry surrounds each unpinned particle with pinned particles in all directions resulting in an overlap of pinned particle influences.

In contrast, the classic confinements provide a pinned particle mean-field interacting from one direction of the particle and bulk interactions from the

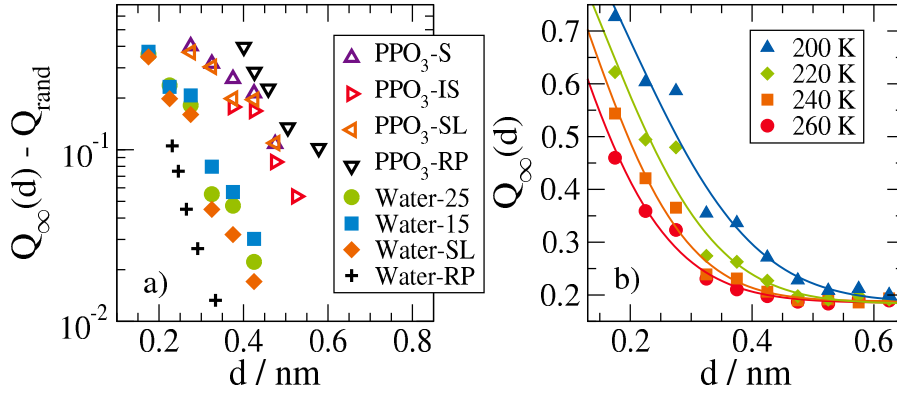


Figure 5.8.: The static correlations/plateau heights Q_∞ for various geometries (SL, RP, IS, S, 15, 25) for PPO_3 (350 K) and water from F. Klameth (240 K) [1] as a function of the distance to the confinement. In (a) data is reduced by the random correlation Q_{rand} , in (b) results for Water-25 with solid lines corresponding to a fit with Eq. 5.5. PPO_3 values are multiplied by a factor of 10 for better visibility.

other. The steeper and hence more sensitive behavior of the RP systems is therefore expected because influences of the mean distance on the single particle are supposed to be higher. Similar effects are hence expected for very narrow confinements, where likewise stronger effects from multiple directions were found in previous studies [189].

The temperature dependency of the distance parameter is displayed in panel (b) of Fig. 5.8. We see larger plateau values upon cooling along with an amplified persistence of the plateau heights at larger distances. Description of the curves as an exponential decay seems the obvious choice regarding the linear behavior shown in Fig. 5.8(a). Yet, slight deviation are better captured with the fit function

$$Q(d) = (1 - Q_{fit}) \exp \left[- \left(\frac{d}{\xi_s} \right)^{\gamma_s} \right] + Q_{fit}. \quad (5.5)$$

This compressed exponential decay with a plateau of Q_{fit} is an empirical function, used in previous studies on spherical confinements [59, 62], and fits some of our data much better than the strictly exponential decay. The plateau values Q_{fit} are fitted here resulting in minor differences to the bulk value but better agreement of the complete data set. We discarded the original bulk values Q_{rand} here, since small differences related to limited statistics in the confinement systems altered the results compared to

the bulk.

Our major result from the fit is the static correlation length ξ_s , which is a measure for the upper limit of correlated regions [62]. This means, for confinements in which the average distance to a pinned particle is larger than this length, no significant deviations to bulk dynamics are observed. Hence, the CRRs or entropic droplets remain undisturbed. As the confinements length is reduced, first deviations to the bulk dynamics occur when the largest CRRs are disturbed, hence the association between the two lengths. Following the findings of previous studies on simple liquids [59–65] our complexer liquid systems, water and PPO₃, experience increasing static length scales ξ_s upon cooling. The results for ξ_s as a function of the temperature in Fig. 5.6(b) show a very good match between all four confinement systems for water and PPO₃.

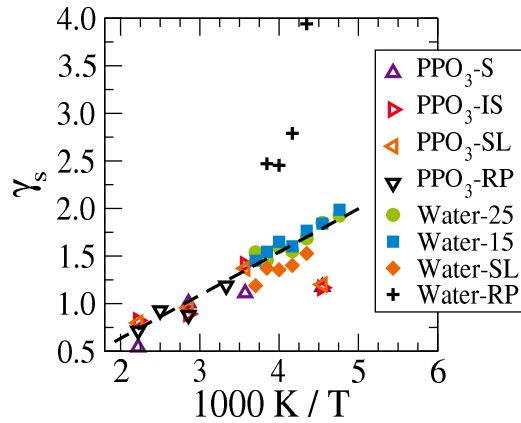


Figure 5.9.: The compression exponent γ_s from Eq. 5.5 as a function of the inverse temperature for the PPO₃ and water [1] systems and the confinements as labeled in previous figures. Dashed line as guideline for the eye.

The exponents γ_s for all systems and confinements increase upon cooling as shown in Fig. 5.9. This result is also found in the relevant literature and generally connected to the RFOT theory of the glass transition [62]. Assuming a liquid is in the supercooled state, the static correlation length as mentioned before is just the largest possible region size necessary for relaxation under the most extreme conditions. This means the necessary size of a region completely surrounded by pinned particles must have a size of ξ_s for relaxation. In contrast to the theoretical picture and because

we study just moderately cooled systems, there are not just mobile and pinned particles, but all sorts of moderately fast particles, so that even regions smaller than ξ_s may contribute to the relaxation. In an idealized picture Q_∞ would be a step function $\Theta(\xi_s - d)$.

Considering a distribution of region or mosaic sizes then yields a superposition the different step functions yielding an exponential decay of the static structure. The compressed exponential decay displayed in Fig. 5.8 hence may be interpreted as the smeared-out high temperature equivalent of this step. Furthermore, the exponent γ_s then measures the deviation from the step function, where increasing γ_s corresponds to a sharper, more step-like transition.

Considering these arguments, the increase in γ_s observed in Fig. 5.9 reflects the sharpening definition of the static length scale. Apparently, this effect is quite similar for the different confinements with the exception of the RP water system. This can be explained with the stronger influence of the confinement from all directions being typical for the RP geometry. In the PPO₃-RP confinement on the other hand, the effect is not apparent because we have only pinned whole molecules. Each unpinned oxygen atom is hence still connected to other unpinned atoms. Thus, the confinement effect is substantially reduced and comparable to the classic confinements.

For both definitions of length scales, dynamic ξ_d and static ξ_s , as well as both systems, we have found linear growth of the length scales as a function of inverse temperature. While the dynamic length scale identified the RP confinements as a different class of system, the results for the static length scale match for all four confinements. Thus, the present results complement previous findings [59–65] on dynamic and static length scales for simple liquids by two complexer liquids thereby demonstrating validity of the approach.

5.3 Description of the Bulk

Finally, we can ascertain the meaning of the dynamic and static length scales obtained from the confinements to the studied bulk systems. In the theory chapter (Sec. 2.1) we have introduced the concepts of the Adam-Gibbs (AG) and Random First Order Transition (RFOT) theories, which postulate the free energy barrier ΔF as the relevant relaxation barrier and hence derived its relation to the region/mosaic sizes. In the AG approach

the configuration entropy S_{conf} dominates and thus the number of particles and the region volume

$$\Delta F \sim n \sim \xi^d \quad (5.6)$$

are the relevant control parameters governing the glass transition. Here, d

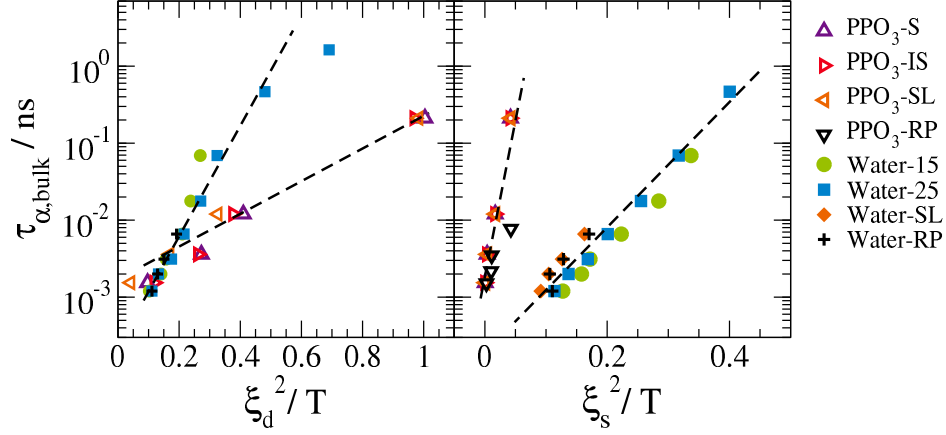


Figure 5.10.: Relation between bulk relaxation times and correlation lengths of water from F. Klameth [1] and PPO₃. In panel (a) as a function of the dynamic correlated length ξ_d^2/T and in panel (b) of the static correlation length ξ_s^2/T . Lengths ξ_d and ξ_s are in nm, $1/T$ in 1000/K.

is the dimension of the region, which is not necessarily equal to the system dimension due to the complexity of the effect. For the RFOT theory the introduction of a surface tension term shifted the dominating influence to the surface exponent

$$\Delta F \sim \xi^\theta, \quad (5.7)$$

where in principle $\theta \leq d - 1$ and a Vogel-Fulcher-Tammann law results for $\theta = 3/2$. With the relation

$$\tau_\alpha \sim \exp\left(\frac{\Delta F}{k_B T}\right) \quad \text{or} \quad \log(\tau_\alpha) \sim \Delta F/T \quad (5.8)$$

it becomes clear that a good choice for the exponent in a semi-logarithmic representation results in a linear relation. In previous studies different exponents $\theta = 1$ and $\theta = 2$ were reported [59, 62]. In water as well as the PPO₃ a linear relation is observed for an exponent $\theta = 2$. Moreover, this result is found for both the dynamic and static length scale along with the different confinement geometries. These findings clearly deviate from the

expected VFT behavior associated with an exponent of $\theta = 3/2$ and support the suggestion of RFOT that a surface tension propagates the dramatic increase of correlation times upon the approach of the glass transition.

5.4 SHD in RP Confinement

Of course, it is of interest to ascertain the well-known SHD indicators for the confinement systems, following the analyses of the bulk. Unfortunately, the parameters are very sensitive to statistical fluctuations so that we cannot present a reasonable distance-resolved analysis of the classical systems. For the RP system on the other hand, we calculated the SHD indicators of the mobile fraction.

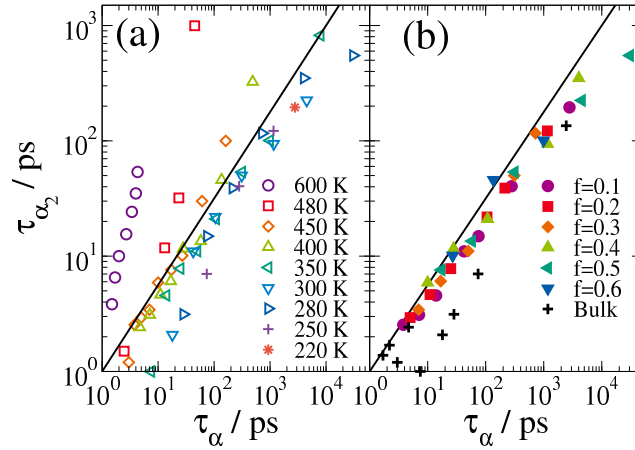


Figure 5.11.: Peak time of the non-Gaussian parameter $\alpha_2(t)$ as a function of the relaxation time τ_{α} for the PPO₃-RP system at different temperatures and fractions of pinned particles f . Panel (a) open symbols indicate data sets with constant T at variant f . Panel (b) full symbols indicate data sets of constant f at variant T . Solid line power law of slope 0.75

In Figs. 5.11 and 5.12 we present the results for the non-Gaussian parameter $\alpha_2(t)$ and the 4-point density correlation $\chi_4(t)$ in the scaling presentation known from Sec. 4. As a guideline for the eye we provide consistent markings for constant temperature in panel (a) and for constant pinned fractions in (b). In analogy to the scaling observed in Sec. 4 we again observe that a power law of slope 0.75 describes the data very well. Merely, the high temperatures 600 K and 480 K follow a steeper power law. Those

systems however are here only shown for pinned fractions $0.8 < f < 0.98$. For these high temperatures lower pinned fractions yield no significant deviations from bulk behavior. As consequence of these high pinned fractions on the other side statistics may influence the results in an unwanted way and the power law is changed. Within a reasonable range of pinned particles $0 < f < 0.6$ we observe very good agreement when f or T are varied. A similar result is found for τ_{χ_4} in Fig. 5.12 and for the cluster and string sizes².

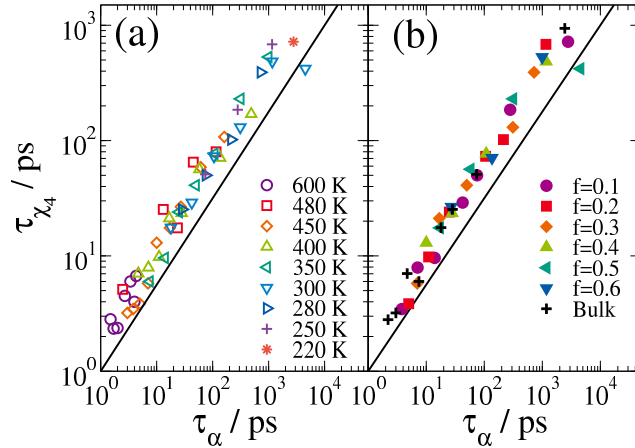


Figure 5.12.: Peak time of the 4-point-density correlation $\chi_4(t)$ as a function of the relaxation time τ_{α} complementary to previous figure.

Conclusively, the temporal correlation between the SHD indicators and the bulk α -relaxation times is unperturbed by the confinement, i.e., we may describe the influences of the confinement via SHD. These findings are interesting because the dynamic correlation length ξ_d did not describe the bulk relaxation in the RP geometry. Yet SHD seem to describe the dynamics just as in the bulk. A complementary study of the SHD indicators within a confinement system has not been conducted to our knowledge so that we have not developed a clear picture of the connections between the findings.

In Sec. 4 we have proposed the full width at half maximum (FWHM) of $\alpha_2(t)$ as a descriptive value for the heterogeneities. As in the previous chapter please note that the following idea for an evaluation of SHD in confinements has been neither conducted nor proposed in any of the pre-

² see Appendix B.2

vious studies. Here, we will apply the method to the confinement systems in analogy to the definition of the dynamic and static correlation lengths. First, we rescale $\alpha_2(t)$ by its peak time τ_{α_2} and peak height $\alpha_{2,max}$. On a logarithmic time scale we then define the full width at half maximum (FWHM) of the peaks. In Fig. 5.13 we present the original curves along with the rescaled curves in panel (b).

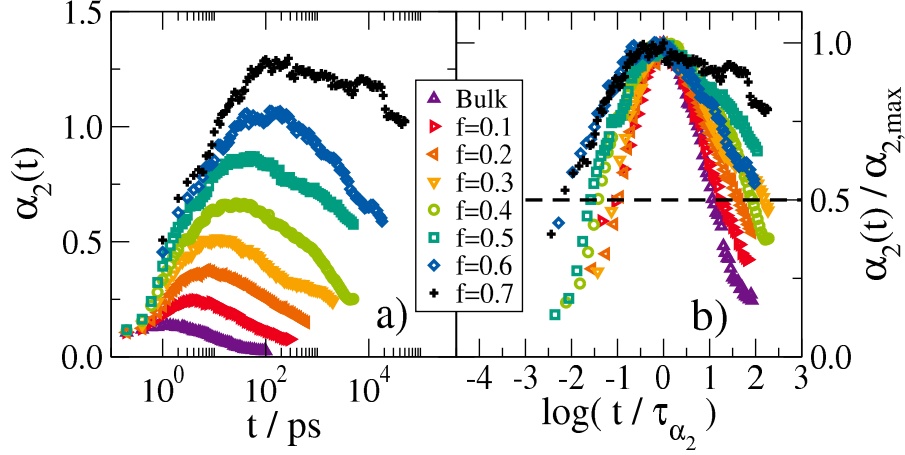


Figure 5.13.: Non-Gaussian parameters $\alpha_2(t)$ for the PPO₃-RP system at 350 K for different fractions f of pinned particles. In panel (b) the data is normalized to the peak value $\alpha_{2,max}$ and shifted horizontally to achieve a comparable peak location. The time axis of panel (b) is chosen logarithmically. Determined FWHM of the curves are given in units of time decades equivalently.

The resulting FWHM curves for each temperature are then represented as a function of the average distance to a pinned particle d in Fig. 5.14(a). A fit function resembling Eq. 5.3

$$\frac{FWHM(\alpha_2)}{FWHM_\infty} \propto \exp\left(-\frac{d}{\xi_{SHD}}\right) \quad (5.9)$$

is applied to describe the distant-dependent curves. Again the fits yield a length scale, here for the SHD referred to as ξ_{SHD} . In panel (b) of Fig. 5.14 on the primary axis in black circles the fit values of ξ_{SHD} are shown in an Arrhenius representation. In analogy to Fig. 5.10 we also present the bulk relaxation time $\tau_{\alpha,Bulk}$ as a function of ξ_{SHD}^2 / T in red squares on the secondary axis. Here, with the choice of a quadratic exponent $\theta = 2$ we already imply to find results comparable to the other length scales. With

$\theta = 3/2$ a Vogel-Fulcher-Tammann is expected and for a linear relation $\theta = 1$ the corresponding region has an overall dimension $\theta < d - 1$ pointing towards a string-like motion.

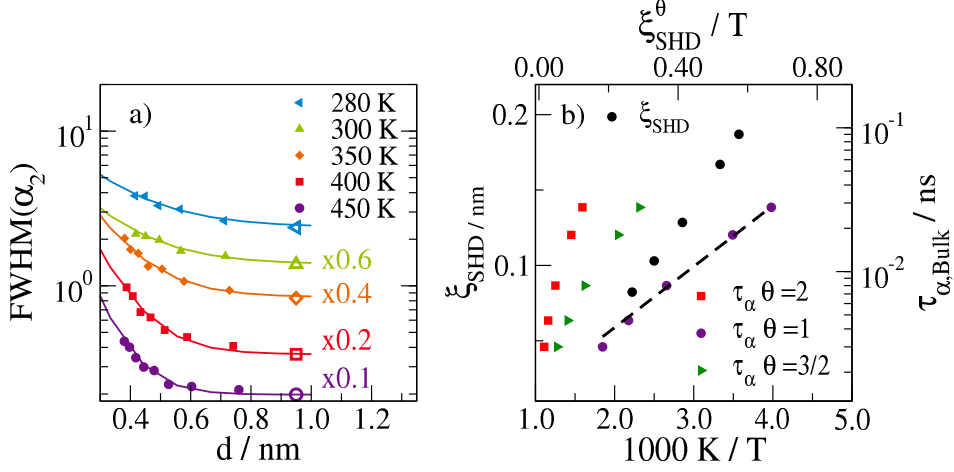


Figure 5.14.: (a) FWHM of PPO₃-RP extracted from $\alpha_2(t)$ in Fig. 5.13(b) in units of time decades as a function of the distances to pinned particles d . The fit function is given in Eq. 5.9 and yields ξ_{SHD} as given in panel (b). Regular axis in panel (b) show the SHD length scales ξ_{SHD} as a function of the inverse temperature. Alternative axis in panel (b) show the bulk relaxation time τ_α as a function of ξ_{SHD}^θ/T , with ξ_{SHD} in nm and $1/T$ in 1000/K.

In Fig. 5.14(b) the higher exponents $\theta > 1$ exhibit a non-linear relation, whereas for $\theta = 1$ we can fit a straight curve. Obviously, the three exponents presented deviate only mildly when certain points are neglected, yet the linear exponent fits better in a systematic way. Previous studies [58, 59] also found the exponent to be ambiguous. Specifically, it was shown by Biroli et al. in Ref. 58 that the evaluation of the exponent may vary throughout the time range. It was found that in the supercooled liquid an exponent $\theta = 1$ suffices, whereas upon more excessive cooling towards the glass transition an exponent $\theta = 2$ fits the data better.

The data presented here can only be interpreted as moderately supercooled as a consequence of the limits of the MD simulation method. Within the observations of this regime, however, our findings for the complexer PPO₃ system agree with interpretation from previous studies on model liquids [58, 59].

5.5 Summary

In this chapter we have studied the influences of four different confinements on PPO₃ and water from F. Klameth [1]. We have extracted a temperature-dependent dynamic length scale ξ_d from the incoherent scattering function along with a static length scale ξ_s from the overlap correlation plateau height. It was shown that the dynamic scaling between characteristic times of SHD and the structural α -relaxation holds within the random pinned confinement and allows bulk behavior to be described. In analogy to the previous chapter a new procedure applied the FWHM of the non-Gaussian parameter $\alpha_2(t)$ to extract a third length scale of the SHD ξ_{SHD} .

Within the well-known Adam-Gibbs and Random First Order Transition theories length scales and their dimensions play a critical role. In this chapter we were able to show that dynamic length scales along with their static counterpart describe the bulk behavior of water and PPO₃ very well. Specifically, for an exponent $\theta = 2$ the evolution of the length scales explains the bulk relaxation time very well. This result was found for all system and confinement geometries, excluding the dynamic length scale in the random pinned (RP) geometry, an effect well known from previous studies [190]. An explanation of the bulk relaxation time via SHD correlation length ξ_{SHD} yields an exponent of $\theta = 1$, whereas the correct exponent is hard to determine due to possible variations over time scales reported in Refs. 58 and 59.

In conclusion, we found very good descriptions of the bulk relaxation time via three different types of length scales for two different molecules in four different confinements. Systematically, we thereby estimated the exponent of the functionality to be $\theta \leq 2$. In comparison to theoretic concepts we hence discard the Adam-Gibbs approach for its prediction of a volume dependent term ξ^d and find further motivation to investigate the RFOT approach.

After our preliminary findings in Sec. 4, which indicated significant influences of string-like motion, the findings of very small exponents support this interesting feature.

6 Relation to Experimental Methods using the Example of NMR

This section will illustrate the possibility to use molecular dynamics (MD) simulations for improvements in experimental methods. The following study was published in the Journal of Solid State Magnetic Resonance Spectroscopy (see Ref. 89) and contributes an MD perspective on nuclear magnetic resonance (NMR) observables. Apart from a merely theoretical point of view this chapter also refers to some aspects of a study published in Macromolecules (see Ref. 2), which concentrates on the comparison of field-cycling (FC) NMR and MD data. Specifically, the chain-length dependence of polymer dynamics is investigated for the examples of poly(propyleneglycol) (PPG) and poly(propyleneoxide) (PPO).

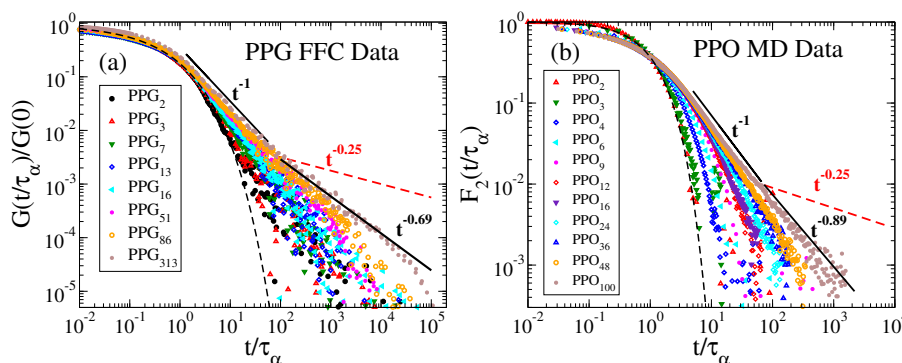


Figure 6.1.: (a) Normalized and rescaled proton-proton correlation function $G(t/\tau_\alpha)/G(0)$ for PPG from FC ^1H NMR relaxometry and (b) rescaled rotational autocorrelation function $F_2(t/\tau_\alpha)$ for the oxygen-oxygen vector along the backbone in PPO calculated from MD simulations [2]. Dashed black line: stretched exponential in regime 0. Solid black lines: power laws in the regimes I and II. Dashed red line: prediction of tube-reptation model in regime II.

NMR is a widely used, powerful experimental tool, which provides structural as well as dynamic information through a variety of possible probe nuclei. Especially, successful measurements in a wide range of magnetic fields strengths, called field-cycling NMR, have recently increased possible uses. With this method the possibility to obtain dynamic data for seven decades in time with a resolution of 5 decades as illustrated in Fig. 6.1 is

of high value. Here, we see the data is complemented by MD data, which exhibits the same characteristic features of polymer dynamics. While the topic has been studied extensively, including some theoretical work, an MD analysis has not been conducted so far. Hence, this study will investigate the interpretation of NMR data. We will focus on protons (^1H s) and deuterons (^2H s) belonging to the most common nuclei. While the quadrupolar interaction, reflecting purely rotational motion dominates in ^2H NMR, the homonuclear dipole-dipole interaction probing intramolecular, rotational parts as well as intermolecular, translational parts, is most important in ^1H NMR.

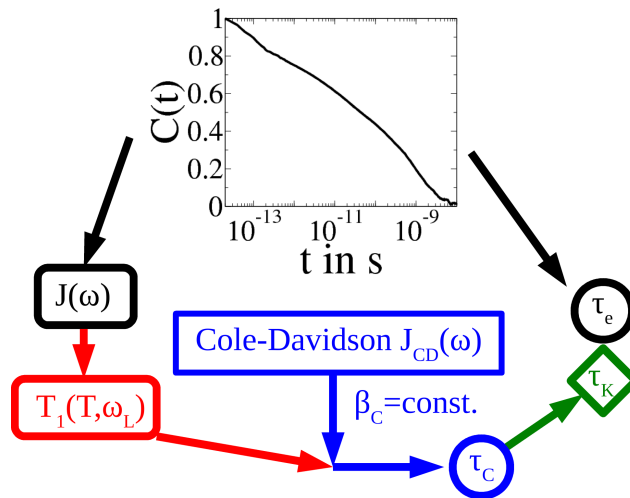


Figure 6.2.: Illustration of the two analytic methods to obtain the supposedly equivalent molecular correlation times τ_K and τ_e

In detail the following chapter will determine the validity of the assumption that the reorientation of the $^1\text{H} - ^1\text{H}$ vector is isotropic, see Sec. 6.2.1. Furthermore, the following section addresses the question which protons or which respective vectors provide relevant contributions to the observables, i.e., we determine to which extent, e.g., next neighbor interactions are sufficient. In Sec. 6.2.3 we will then compare the obtained NMR correlation functions with the well-known observables from other methods, e.g., neutron scattering, and show deviations are well motivated. Our calculations are then used in Sec. 6.2.4 to validate the analysis method applied in NMR as illustrated in Fig. 6.2. In addition, we will validate a new method to obtain the diffusion with FC NMR. Finally, in Secs. 6.2.7 and 6.2.8 the

choice of the exact vector for the correlation is investigated. Thereby, it is of interest, which calculation yields the best reproduction of the NMR data and which feature of the NMR method stands against the theoretic description within the models.

First, however, we provide a basic definition of the NMR framework. Then, starting with our PPO and PEO simulations for various chain lengths N , we will calculate correlation functions $C(t)$, spectral densities $J(\omega)$ and spin-lattice relaxation (SLR) rates $1/T_1$ checking each of the assumptions commonly made in experimental works step by step. The study will show most of them to be valid, but often misjudged in their range of validity, and provide suggestions for improved interpretation and analysis routines.

6.1 Theoretical Principles of NMR

In this section the basics of ^1H and ^2H NMR are described. As major differences ^1H interactions are dominated by a multi pair dipole-dipole (DD) interaction with a rotational component and a translational component in form of a distance dependence. ^2H interactions on the other hand are dominated by quadrupolar (QP) interactions related to the C- ^2H bond therefore mainly reflecting rotational motion.

6.1.1 ^1H NMR Observables

A major observable in NMR is the spin-lattice relaxation (SLR) rate $1/T_1$, in case of ^1H given by

$$\frac{1}{T_1} = \frac{3}{2}I(I+1) \left(\frac{\mu_0}{4\pi}\right)^2 \gamma_G^4 \hbar^2 [J^{(1)}(\omega) + J^{(2)}(2\omega)] \quad (6.1)$$

Here, I and γ_G are the nuclear spin and the gyromagnetic ratio of the proton respectively. The spectral densities $J^{(m)}(\omega)$ are defined by the relations:

$$J^{(m)}(\omega) = 2 \operatorname{Re} \int_0^\infty G^{(m)}(t) \exp(-i\omega t) dt \quad (6.2)$$

$$G^{(m)}(t) = \sum_k \langle F_{jk}^{(m)}(0) F_{jk}^{(m)*}(t) \rangle \quad (6.3)$$

$$F_{jk}^{(m)}(t) = d_m \frac{Y_{2m}(\Omega_{jk}(t))}{r_{jk}^3(t)} \quad (6.4)$$

Apart from $J^{(1)}$ and $J^{(2)}$, the spectral density $J^{(0)}$ will be of some relevance in the following. In the above equations, the constants are $d_0^2 = 16\pi/5$, $d_1^2 = 8\pi/15$, and $d_2^2 = 32\pi/15$. The time-dependent internuclear vector connecting proton j and proton k is denoted as $\mathbf{r}_{jk}(t)$, where r_{jk} is its modulus and $\Omega_{jk} = (\theta_{jk}, \phi_{jk})$ is its orientation with respect to the direction of the external magnetic field. The normalized spherical harmonics are referred to as Y_{lm} and the angular brackets $\langle \dots \rangle$ indicate an average over all pairs of protons.

At this point we make one of the most common assumptions of ^1H NMR studies on polymer melts, an isotropic distribution of all directions in combination with an isotropic reorientation. As one can already suspect from the prefactors after an integral over all directions [191], these assumptions yield the relation

$$\frac{1}{6}G^{(0)}(t) = G^{(1)}(t) = \frac{1}{4}G^{(2)}(t). \quad (6.5)$$

As a result, provided the assumptions holds, it is possible to discuss all further formula work in $m=0$. We will follow the custom approach and continue discussing the formula work assuming the assumptions hold, but we will check their validity below. When considering Eq. 6.3 again, two contributions can be distinguished, namely the intra- and the intermolecular part. Contributions arising from protons k within the same molecule as proton j are henceforth denoted as $G_{intra}^{(m)}$, whereas those related to other molecules are referred to as $G_{inter}^{(m)}$. Following Eq. 6.2 $J_{intra}^{(m)}$ and $J_{inter}^{(m)}$ are named accordingly. Hence the SLR rate can be presented as a sum of both contributions [131, 132]:

$$\frac{1}{T_1} = \frac{1}{T_{1,intra}} + \frac{1}{T_{1,inter}} \quad (6.6)$$

The contributions may be identified with two basic motions, a rotational intramolecular motion on rather short time scales or high frequencies [74] and a translational intermolecular motion. The latter includes short-time and long-time parts, though on short time scales the rotational motion clearly dominates. On long time scales or low frequencies [133, 192] on the other hand all rotations are relaxed and a purely translational motion can be observed.

We start by discussing the fast intramolecular motion. Due to the non-exponential nature of glassy dynamics, it has proven useful to describe such dynamics with a stretched exponential correlation function called Kohlrausch-Williams-Watts (KWW) function or, in the frequency domain, a Cole-Davidson (CD) spectral density:

$$G_{\text{intra}}(t) \propto \exp \left[- \left(\frac{t}{\tau_K} \right)^{\beta_K} \right] \quad (6.7)$$

$$J_{\text{intra}}(\omega) \propto \frac{\sin [\beta_C \arctan(\omega \tau_C)]}{\omega [1 + (\omega \tau_C)^2]^{\beta_C/2}} \quad (6.8)$$

Both functions describe a similar underlying distribution of correlation times $G(\tau)$, but with slightly different correlation times τ_C and τ_K and stretching parameters $0 \leq \beta_C, \beta_K \leq 1$. Characteristic for glassy dynamics is the stretched exponential in the time domain, associated with deviations to the classic Bloembergen-Purcell-Pound model [193] (BPP model) in the frequency domain. The relation between a single exponential decay as characteristic for BPP and the stretching factor β_C in CD is well known so that β_C is determined via the deviations. Assuming the relaxation of each entity to be single exponential leads us via a Laplace transformation to the distribution of relaxation times $G(\tau)$, which broadens with decreasing β_C, β_K .

In the present case we are investigating polymers which experience, aside from simple glassy dynamics, polymer dynamics associated with the connectivity of the chain. These dynamics dominate the long-time behavior leading to a power law in the Rouse regime (see Sec. 2.2.2), e.g., $G(t) \propto t^{-1}$. For a long polymer exceeding the so-called entanglement length¹ N_E the polymer dynamics cross over to entanglement dynamics after the relaxation of the longest Rouse mode denoted as τ_R . Here, we observe the first stages of entanglement dynamics. Since $N_E \approx 90$ [194] is about the largest chain we can investigate and τ_R is close to our available time window.

Apart from these intramolecular dynamics we will discuss the possibility to extract self-diffusion coefficients from ¹H SLR. Recent studies [74, 195] have provided new approaches to exploit the $r_{jk}^{-3}(t)$ -dependency in Eqs.

¹ see: Sec. 2.2.3 and Ref. 2, 80

6.3 and 6.2. When assuming a model of free diffusion it is possible to derive a model correlation function G_{inter} and its associated spectral density J_{inter} :

$$G_{\text{inter}}(t) = 72 \frac{N_H}{d^3} \int_0^\infty \frac{u^2 \exp\left(-\frac{u^2 t}{\tau_T}\right)}{81 + 9u^2 - 2u^4 + u^6} du \quad (6.9)$$

In this model, force-free diffusion of hard spheres and reflecting boundary conditions were supposed [196]. The model furthermore introduces a distance of closest approach d as a characteristic of the hard spheres, which carry the nuclear spin in their centers. A uniform distribution of spheres beyond the distance of closest approach is additionally assumed. N_H accounts for the number density of spins in the system, here represented by the hydrogen atoms. Dynamic information is provided by the translational relaxation time τ_T in the hard sphere model, which is related to the diffusion coefficient (D) by

$$2D = \frac{d^2}{\tau_T}. \quad (6.10)$$

D is herein derived via the relative self-diffusion coefficient D_R , which is just twice as large. Application of the model henceforth allows to extract D from the intermolecular contribution to the ^1H - ^1H correlation function G_{inter} [132, 133]. In the following we will test the applicability of this model for polymer dynamics. While the assumptions largely represent the basic characteristics of a simple liquid, a complex liquid as the present polymer melts differs in a number of properties. The assumption of free diffusion with Gaussian distributed motion and neglecting rotational contributions to the intermolecular part are addressed in Sec. 6.2.

Furthermore, Kehr et. al. (see Ref. 131) have shown that SLR may provide access to shorter time scales of the proton via the mean-squared displacement (MSD) $\langle r_H^2(t) \rangle$. Unfortunately, we cannot derive the relation step by step here, for the details please refer to the relevant literature [131]. Especially, for long polymers one may assume the existence of a subdiffusive regime ($\propto t^\epsilon$, $\epsilon < 1$) preceding regular diffusion ($\propto t^1$). The combination of this regime with the common assumption of Gaussian distributed bead displacements $G_0(\vec{r}_i(t) - \vec{r}_i(0))$ allows one to derive a term for the correlation function G_{inter} and hence also J_{inter} . This is possible via introducing the new propagator (Gaussian with subdiffusive MSD) into the definition of the correlation function yielding

$$G(t) \propto \frac{1}{\langle r^2(t) \rangle^{3/2}}. \quad (6.11)$$

Considering the correlation function yields the spectral density. Through a Fourier transformation we can then derive a relation to the intermolecular SLR rate $1/T_1$

$$\frac{1}{T_{1,inter}(\omega)} \propto \frac{1}{\omega \langle r^2(t = 1/\omega) \rangle^{3/2}} \quad ; \quad \langle r^2(t = 1/\omega) \rangle \propto \left[\frac{T_{1,inter}(\omega)}{\omega} \right]^{2/3} \quad (6.12)$$

The rearrangement of the equation reveals that the intermolecular SLR can hence be used to approximate the MSD in intermediate, subdiffusive regimes. The validity of these and other equations will be investigated based on simulation data.

6.1.2 ^2H NMR Observables

In this section we will present the theoretical basics of ^2H NMR, the second nucleus investigated in this study. ^2H NMR probes the dominant quadrupolar interactions, which are closely related to the C-D bond. In detail, the interaction describes the coupling of the nuclear electric quadrupole moment (Q) to the electric field gradient tensor at the nuclear site. As PEO and PPO exhibit aliphatic C-D bonds the relevant electric field gradient tensors are axially symmetric [197]. Its distinct direction then points along the C-D bond axis with eq denoting the corresponding eigenvalue. In the following we assume the protons in the simulation do not yield any other dynamic information than a deuteron would. Hence the calculation of ^2H NMR data may be conducted with the protonated systems at hand, i.e., the orientation of the C-H bonds in the simulation are supposed to reflect those of the C-D bonds in the experiment.

NMR measures resonance frequencies of the spins as a result of the orientation with respect to the applied magnetic field and the electric field gradient tensor, which is here represented by the angle θ between C-D (C-H) bond and a distinct direction. In order to measure the fluctuations for isotropic systems the rotational auto-correlation function (RACF)

$$F_2(t) = \left\langle \frac{P_2[\cos \theta(0)]P_2[\cos \theta(t)]}{P_2[\cos \theta(0)]P_2[\cos \theta(0)]} \right\rangle \quad (6.13)$$

is defined. $P_2(x)$ here denotes the second Legendre polynomial and the angular brackets an ensemble average. In analogy with Eq. 6.2 the cor-

responding spectral density of ^2H NMR $J_2(\omega)$ is obtained, yielding the relaxation rate

$$\frac{1}{T_1} = \frac{1}{15} \left(\frac{3e^2qQ}{4\hbar} \right)^2 [J_2(\omega) + 4J_2(2\omega)]. \quad (6.14)$$

The coupling constant of ^2H NMR is known from experiments as

$$\frac{3e^2qQ}{4\hbar} = 2\pi \times 125\text{kHz} \quad (6.15)$$

for aliphatic bonds [197]. This stands in contrast to ^1H coupling constants, which are related to the inter-spin distances resulting from spin-pair correlation. ^2H coupling constants result from a single spin interaction and hence, are free of this influence.

In the following result section we will often compare results of ^1H and ^2H NMR and therefore give an alternative representation of Eq. 6.1 at this point:

$$\frac{1}{T_1} = \frac{3}{2} I(I+1) \left(\frac{\mu_0}{4\pi} \right)^2 \gamma_G^4 \hbar^2 \left\langle \frac{1}{r_{ij}^6} \right\rangle [J'(\omega) + 4J'(2\omega)] \quad (6.16)$$

In this representation we have assumed an isotropic distribution of the H-H vectors, constant distances r_{ij} and hence dominating next neighbor influences. Thus, we can draw $\left\langle \frac{1}{r_{ij}^6} \right\rangle$ into the front and out of the Fourier transformation. Hence $J'(\omega) = J(\omega) / \left\langle \frac{1}{r_{ij}^6} \right\rangle$ is quite comparable to $J_2(\omega)$ only referring to a different vector. With this modification it is possible to discuss the two SLR T_1 regarding their different coupling constants with rather figurative arguments.

6.2 Results

In the following we will address the theoretical assumptions which experimental studies usually simply accept.

6.2.1 Interchangeability of Correlation Functions $G^{(m)}(t)$

In Fig. 6.5(a) the three random functions $G^{(m)}(t)$ are scaled to agree for isotropic reorientations. While $m = 2$ closely matches $m = 0$, $m = 1$

exhibits significant deviations. At first sight these findings are not plausible, since the system itself has a sufficient size. In conclusion, the orientation of the ^1H - ^1H vector should be isotropic. What the figure does not show is whether the amplitudes of the random functions $G^{(m)}(t=0)$ scale correctly, since the logarithmic time axis does not include this point. However, we have inspected the amplitudes of several systems including several chain lengths, pressures, and polymeric structures, all showing a perfect scaling according to

$$G^{(0)}(0) = 6G^{(1)}(0) = 6/4G^{(2)}(0). \quad (6.17)$$

Conclusively, the last remaining explanation is differences in the ampli-

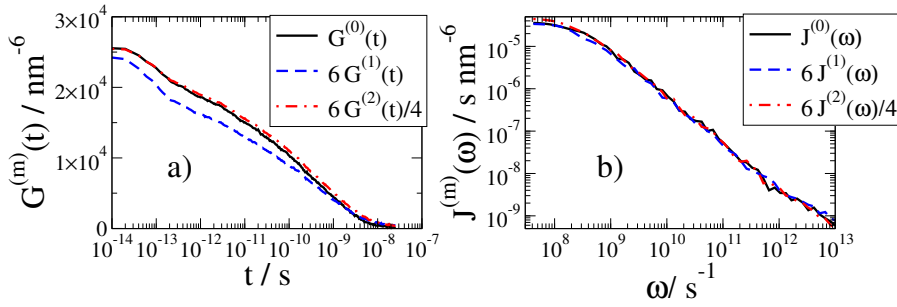


Figure 6.3.: Scaled (a) random functions ($G^{(m)}(t)$) and (b) spectral density (SD) $J^{(m)}(\omega)$ for PEO_{12} at 265 K.

tude of the process preceding the structural relaxation at times outside the studied time window. This first decay commonly identified as vibrational motion, obviously affects all following data in amplitude. In order to check this we have rescaled all $G^{(m)}$ dividing them by the relative height of the final decay, which leaves us with a reduced random function $g^{(m)}(t)$ excluding vibrational influences.

$$g^{(m)}(t) = G^{(m)}(t) \left/ \frac{G^{(m)}(t_{vib})}{G^{(m)}(0)} \right. \quad (6.18)$$

Where t_{vib} denotes the characteristic time where the transition from the first, vibrational relaxation to the second, structural relaxation takes place. This reduced random function is shown in Fig. 6.4 emphasizing the proposed vibrations to cause the deviations. After the removal of the varying vibrational amplitudes, all three random functions agree very well and isotropic distribution of the ^1H is assured.

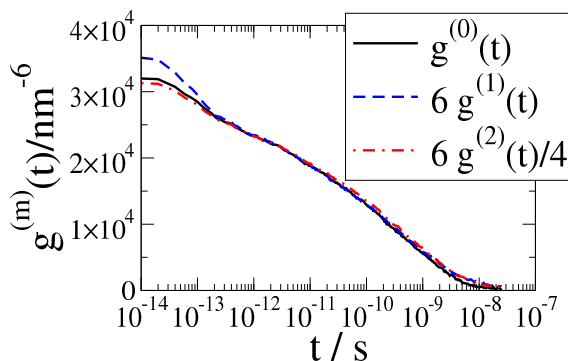


Figure 6.4.: Twice-scaled random functions ($G^{(m)}(t)$) according to Eq. 6.18 and the isotropic assumption in Eq. 6.17 for PEO₁₂ at 265 K.

This leaves to explain why the vibrational motion should be anisotropic. Vibrations refer to movement around the minimum of a harmonic potential of a bond for example. As indicated by the rather small amplitude with regard to structural relaxation, vibrations are rather small movements. Therefore vibrations of proton A in relation to proton B will have different results for the vector orientation depending on their distance. In case of a large ^1H - ^1H distance the vibrational motion will not alter the orientation to the magnetic field θ significantly, whereas on short-distanced pairs a vibration with the same amplitude will induce significant changes. This can all be said neglecting the r_{ij}^{-6} -dependency of the correlation function, since for a vibration we may assume movement around a single minimum. Conclusively, pairs with long distances essentially do not move concerning $G^{(m)}(t)$ whereas close pairs do very well. Now the sub-ensemble of contributing pairs clearly does not follow an isotropic distribution, because the polymer structure does not surround all protons evenly with partners. So even while the large length scale structure of the system may not change during times $t < t_{vib}$, the foreground around a single proton does exhibit dynamic changes through vibration. While this may leave us with an isotropic static case the, dynamic case sees these differences and therefore is anisotropic.

However Fig. 6.3(b) also shows the relevant spectral density of $G^{(m)}(t)$ $J^{(m)}(\omega)$, which are the actually relevant functions concerning Eq. 6.1. $J^{(m)}(\omega)$ however does not experience the differences seen in $G^{(m)}(t)$ since the amplitude effect is merely reflected in slightly higher contributions on the high frequency side. Subsequently, the NMR analysis approximation

can be assumed as valid, so henceforth we will skip the superscript (m). Specifically, we denote $G(t) \equiv G^{(0)}(t)$ and $J(\omega) \equiv J^{(0)}(\omega)$.

6.2.2 Contributions to $G(t)$ and their Relevance

In Sec. 6.1 we have mentioned the basic types of contributions to the $G(t)$, namely intramolecular and intermolecular contributions. Considering the strong distance dependence of the correlation as in Eqs. 6.3 & 6.4 and, thus, of the whole SLR, some studies argue ^1H SLR is dominated by the intramolecular part [75, 82, 198, 199] or even only the next neighbors within that part. Particularly for long times on the other hand it was argued that intermolecular contributions must not be neglected [130–133].

In Fig. 6.5 we provide a detailed analysis of the contributions exemplary for PEO_{12} at 265 K. The major parts of $G(t)$ are G_{intra} with about $\frac{3}{4}$ and G_{inter} with $\frac{1}{4}$ of the contribution. As expected, contributions within the same molecule largely dominate, while at the same time coupling across different molecules is still quite large and non-negligible. Experiments use dilution studies to determine the intramolecular contribution to the ^1H - ^1H correlation function, furthermore leading to assumptions, e.g., domination of next neighbor protons, within this part. Regarding polymer dynamics, assumptions are often made that SLR reflects the dynamics of backbone vectors, so that these contributions are of particular interest. Here, Fig. 6.5 distinguishes between (a) all dipolar interactions within a molecules G_{intra} , (b) a subset including only those protons within neighboring C atoms and (c) only protons within the same CH_2 group.

We have therefore found that identification of the intramolecular part as the rotational correlation function of a single vector is a crude approximation, reflecting only $\frac{2}{3}$ of intramolecular contribution to the ^1H - ^1H correlation function (G_{intra}). At this point it is crucial to mention that these findings are limited to the main part of the decay as displayed in Fig. 6.5. For longer times the behavior is different as we will discuss in the context of Fig. 6.6.

In order to study long-time behavior we will take a look at a double-logarithmic representation of two exemplary systems of a short polymer PPO_2 at 325 K, which basically represents a molecular fluid, and a long polymer PEO_{150} at 300 K, which represents typical polymer dynamics. Fig. 6.6(a) shows inter- and intramolecular data for PPO_2 and 6.6(b) for

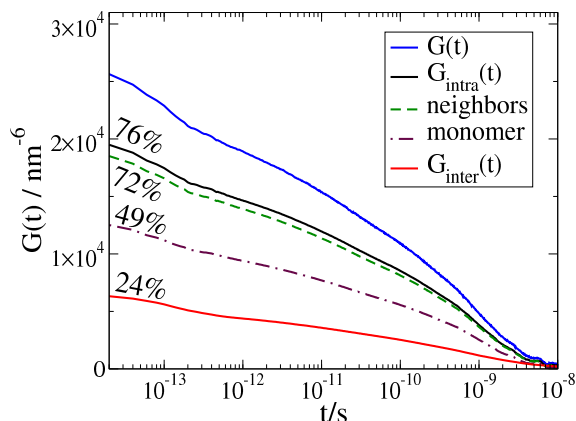


Figure 6.5.: Proton Correlation functions $G(t)$ for PEO_{12} at 265 K. In detail the intermolecular G_{inter} and intramolecular contributions G_{intra} are shown. Of the latter different subsets of the sum are evaluated where the proton interacts only with its counterparts on neighboring C atoms or in the same CH_2 group.

PEO_{150} respectively. The molecular fluid consisting of a short polymer melt exhibits typical glassy dynamics for G_{intra} , which follows a stretched exponential function (KWW). Fig. 6.6(b) on the other hand experiences a power law of type $t^{-\varepsilon}$, which is typical of polymer dynamics [2] (see Sec. 2.2.3). The observed exponent ε however does not match either of the proposed regimes. This result has been found in various studies [2, 73–79], where the exponents are systematically larger than 0.25 for systems in entanglement. Specifically, with $N=150$ merely above the entanglement chain length N_E , the exponent observed here is large compared to other studies.

Furthermore, we describe G_{inter} via Eq. 6.9, thus including the assumptions of the hard sphere model (see Sec. 6.1). For PPO_2 the hard sphere model describes the curve very well since the small molecule is close to the model. The most important part of the curve in this case is the long-time behavior, here asymptotic $t^{-3/2}$. In the end G_{inter} is the gateway to diffusion measurement, which is why only long times, i.e., the diffusive regime is of interest. In case of the polymer in Fig. 6.6(b) the short-time behavior subsequently deviates due to the incorrect model, whereas the long-time diffusive motion is well described. In conclusion, both systems enable a fit of Eq. 6.9 in order to extract the translational relaxation time τ_T , which in turn provides access to the diffusion coefficient D .

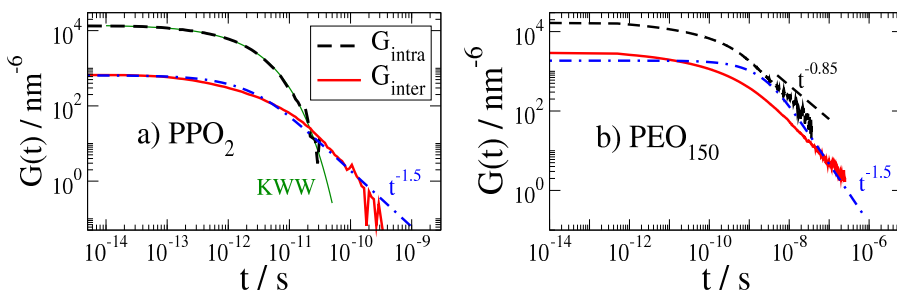


Figure 6.6.: Correlation functions G_{intra} and G_{inter} for a short and a long polymer: (a) PPO₂ at 325K and (b) PEO₁₅₀ at 300K. The logarithmic representation allows closer inspection of the long-time behavior. G_{inter} can be described by Eq. 6.9, predicting an asymptotic $t^{-3/2}$ behavior (dash-dotted lines). G_{intra} can for a short polymer as in (a) PPO₂ be described within simple glassy dynamics. Hence, it is fitted with Eq. 6.7. In case of PEO₁₅₀ a protracted transition to polymer dynamics with a characteristic power law is observed. In the present case $t^{-0.85}$ is provided as a guideline for the eye.

We will present the results of the fit for several systems in Sec. 6.2.6 and investigate possible application regarding the determination of diffusion coefficients. Obviously, the proposed models for the intra- and intermolecular contributions work very well. Yet, it is very important to note that both contributions are without large efforts only accessible as their sum in experimental studies. So far most studies referred only to the normalized correlation functions hence losing all information about relative heights of the two correlations, which are experimentally difficult to assess. Therefore three major conclusions for the experimental work are to be drawn here: (a) For short polymers G_{intra} decays fast enough so it is safe to assume measurement of pure G_{inter} at long times. (b) For long polymers typical polymer dynamics dominate the diffusional part up to long times and low frequencies, therefore making it inaccessible without further knowledge of $G(t)$. (c) Exponents ε of the power-law of typical polymer dynamics may be affected due to the $t^{-3/2}$ decay of G_{inter} .

6.2.3 Comparison of NMR Correlation Functions to other Methods

NMR is but one of various methods investigating dynamic properties of molecules. Any of these methods has pros and cons, which we unfortu-

nately cannot discuss here at this point. However, most of these pros and cons are directly associated with the interactions measured in the experiment and therefore the dynamics they reflect. Considering Fig. 6.7 we will discuss the relations between correlations from ^1H and from ^2H NMR as well as from neutron scattering and experimentally non-accessible vectors evaluated from MD simulations. At this point MD once more shows all its strengths enabling us to calculate experimental data along with theoretically interesting observables. The reader may note here that this data is particularly valuable regarding the fact that the evaluated trajectory is literally the same. So in the present case no experimental effects whatsoever either extrinsic or intrinsic may occur.

As it is often assumed, we can show that the quadrupolar interaction of ^2H NMR here denoted as F_2 yields the same dynamic information as G_{intra} . In contrast to other sections the incoherent scattering function here denoted as $F_s(q, t)$ has been evaluated for protons and the q vector was trimmed to achieve agreement with the NMR curves.

$$F_s(q, t) = \langle \cos\{\mathbf{q} \cdot [\mathbf{r}_i(t) - \mathbf{r}_i(0)]\} \rangle \quad (6.19)$$

A common assumption is that $q \approx 1 \text{ \AA}^{-1}$ yields reasonable agreement between NMR and neutron scattering (NS). In Fig. 6.7 we have identified a scattering vector of $q = 1.2 \text{ \AA}^{-1}$ as a good value to match both experimental methods. Unfortunately, theoretical polymer models do not refer to specific vectors observed in experiments, but backbone tangent vectors such as the intramonomer vector C-C or the intermonomer vector O-O. Therefore, we provide the rotational correlation function calculated in analogy to Eq. 6.13 of these vectors in reference to theoretical models. Both correlations exhibit significantly slower decays, where the longer O-O vector is even slower than the C-C vector. Additionally, both correlation decays are far less stretched than their experimental equivalents. These findings clearly demonstrate that experimental results are not straight-forward comparable to the backbone vectors. Specifically, the time scale and the stretching of a correlation needs careful consideration and may differ compared to, e.g., the reorientation of backbone vectors.

6.2.4 Conventional Spin-Lattice Relaxation Analysis

In the previous parts we have focused on rather microscopic, basic observables, which are not accessible without sophisticated experimental

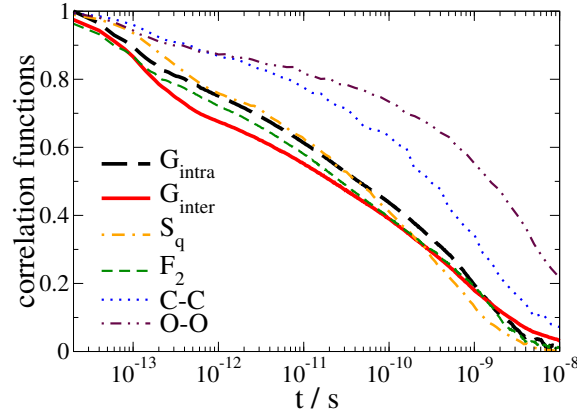


Figure 6.7.: Various normalized correlation functions for PEO₁₂ at 265 K. Proton correlations G_{inter} and G_{intra} are compared to rotational motion of C-H bonds represented by F_2 (see Eq. 6.13). Additionally the rotational correlation function for two backbone vectors O-O (C-C) connecting neighboring O(C) atoms are provided. Finally the intermediate incoherent scattering function of the hydrogen atoms is shown for a scattering vector of $q = 1.2 \text{ \AA}^{-1}$ (see Eq. 6.19).

approaches and analysis. In this part we will focus on the most common evaluation in NMR experiments. In detail, we will here determine if the complicated extraction of the structural α -relaxation time defined via $F_s(q, t)$ (τ_α) from SLR T_1 at variant temperature, as illustrated in Fig. 6.2, yields the same times τ as the direct path via the correlation function, which we take in simulations. For this purpose we will calculate T_1 just as it is obtained in NMR and follow the common NMR analysis. The obtained τ from NMR is then compared to the directly evaluated τ from the correlation function. In contrast to other studies, the original data for both analyses is the same so that the findings of this study are of particular significance.

The beginnings of NMR relaxometry did not include field dependent experiments, hence providing only information about SLR at a single Larmor frequency ω_L . Spectral densities and their Fourier transform, the correlation function, are therefore not accessible. Yet the goal is to extract the relaxation time τ_α from T_1 . Assuming the form of the spectral density as exponential (Debye) or stretched exponential (Cole-Davidson) allows the curve $T_1(T)$ to be predicted via Eq. 6.1 or the other way around respectively. Therefore, even this analysis holds interesting information.

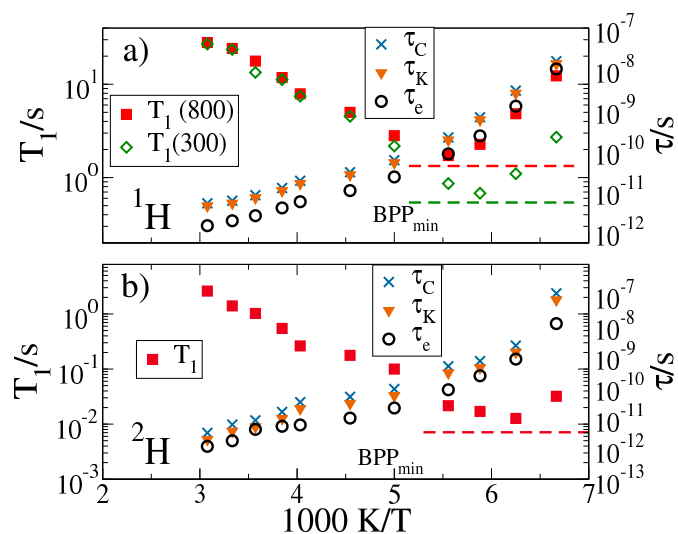


Figure 6.8.: Relaxation and correlation times calculated from MD simulations for PPO₂. Temperature dependence of (a) ¹H T_1 for two exemplary ω_L (300MHz: open squares, 800MHz: solid squares) and (b) ²H T_1 (123MHz). In addition, three correlation times are displayed on the secondary y axis. Therein, τ_C refers to the correlation times from T_1 assuming CD spectral densities with parameters $\beta_C = 0.55$ in ¹H NMR and $\beta_C = 0.40$ in ²H NMR. β_C herein was extracted from the minimum of each T_1 curve and its characteristic deviation to the minimum value expected for exponential correlation functions indicated as dashed lines. τ_C represents the actual procedure applied in experimental work. Correlation times τ_K from the KWW are calculated from τ_C using Eq. 6.20. The result should be comparable to the correlation times of the respective correlation functions (a) $G(t = \tau_e)/G(0) = e^{-1}$ and (b) $F_2(t = \tau_e) = e^{-1}$.

We calculate the relaxation times T_1 according to the equations of Sec. 6.1 for two ¹H NMR frequencies ω_L and one ²H NMR frequency ω_L . For a complex fluid such as a polymer melt we must assume a non-exponential decay and a distribution of correlation times. The common approach is to describe this behavior via the asymmetric spectral density namely the Cole-Davidson (see. Eq. 6.8) [200]. This evaluation allows the extraction of correlation times τ_C directly from T_1 , where the only unknown parameters are the stretching factor β_C and the coupling constant of the process. Experimental approaches extract the coupling constant from the

line shape, whereas we can directly calculate it via the internuclear vectors yielding $\langle r_{ij}^{-6} \rangle$ (see Eqs. 6.3 and 6.2). The analysis assumes an invariant shape of the spectral density and therefore a temperature-independent stretching factor β_C . This assumption is quite common and can also be associated with the time-temperature superposition (TTS). In conclusion, it is sufficient to define the parameter β_C at the T_1 -minimum where it can be extracted. Therefore, Eq. 6.8 inserted in Eqs. 6.1 and 6.14 is tuned to the T_1 -minima of Fig. 6.8. In the following the derived $T_1(\tau_C)$ curve allows a reverse determination of τ_C .

In order to address the validity of this analysis the well-known conversion from CD to KWW [201]

$$\tau_K = \tau_C(1.184\beta_C - 0.184) \quad (6.20)$$

is used to determine τ_K . The correlation time τ_K referring to Eq. 6.7 is for a single decay also associated with a decay to the value of e^{-1} , which we henceforth denote as τ_e .

$$G(t = \tau_e)/G(0) = e^{-1} ; F_2(t = \tau_e) = e^{-1} \quad (6.21)$$

After τ_C is converted to τ_K it is directly comparable to the results from the correlation functions τ_e . In Fig. 6.2 we provide a schematic illustration of the supposedly comparable analyses described here.

In Fig. 6.8 it is evident that none of the T_1 curves reach the T_1 minimum heights of $T_1 = 1.33$ s (^1H 800 MHz) or $T_1 = 7.11$ ms (^2H 123 MHz) of the exponential Bloembergen-Purcell-Pound (BPP) model [193]. An enhanced minimum here reflects the existence of non-exponential correlation functions for the studied systems. Subsequently, a CD function is assumed and the stretching parameters are determined as $\beta_C = 0.55$ and $\beta_C = 0.4$ for ^1H and ^2H , respectively. Above described analysis yields τ_C in Fig. 6.8, where both methods ^1H and ^2H yield comparable results, which do not follow an Arrhenius law. In contrast, the data experiences a polymer-typical fragile behavior described by a Vogel-Fulcher-Tammann (VFT) [6–8] function.

The resulting correlation times experience reasonable but far from perfect agreement. Especially, at high and low temperatures far from the T_1 minima the deviations are substantial. Far from the T_1 minima the SLR analysis is particularly sensitive to the shape of spectral density (SD) ($J(\omega)$), so the result mainly reflects the limited validity of the assumptions. This means,

the shape of the spectral density modeled as a CD with constant β_C may change to other basic forms or just stretching parameters. In case of ^1H NMR a temperature-dependent coupling constant may furthermore complicate the analysis, which we will later on address further in Sec. 6.2.5.

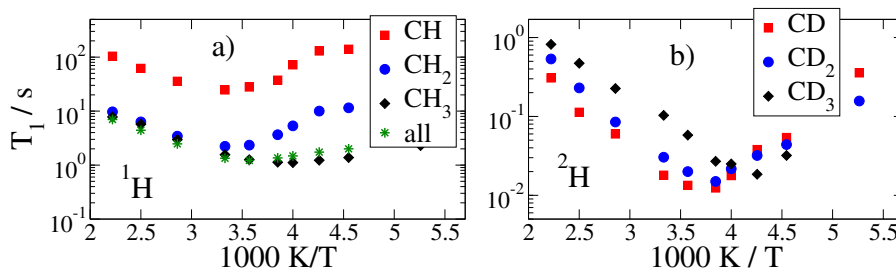


Figure 6.9.: SLR relaxation times (a) ^1H T_1 and (b) ^2H T_1 for different proton and deuteron species calculated from MD simulations for PPO₉. Three types of protons and deuterons can be distinguished by their respective chemical group, methin groups (CH/CD), methylene groups (CH₂/CD₂) and methyl groups (CH₃/CD₃). Panel (a) shows ^1H data, where only the dipolar couplings within protons of the same species were calculated. As a reference data for all proton pairs is provided.

Having considered the experimental point of view with Fig. 6.8, we move on investigating species-dependent results as a sophisticated approach available within MD simulations. For this purpose, a system of PPO₉ is chosen, because PPO includes three different types of proton species, where species shall refer to different chemical groups. CH and CH₂ groups are situated along the backbone chain and the CH₃ groups are attached to the CH group. In order to distinguish the overall contributions of these different species, the correlation functions are evaluated for each species separately. In Fig. 6.9 we present the temperature dependence of the SLR T_1 for $\omega_L = 2\pi \cdot 300 \text{ MHz}$ (^1H) and $\omega_L = 2\pi \cdot 123 \text{ MHz}$ (^2H).

We observe for ^1H NMR in Fig. 6.9(a), that the two species along the backbone of the chain, CH and CH₂, experience a similar shape and therefore similar dynamics. At the same time the data is clearly shifted as a consequence of strongly deviating coupling constants. With the coupling constant linked to $\langle r_{ij}^{-6} \rangle$ (see Eqs. 6.3 and 6.4) it is clear that the significantly larger distance between protons of two CH groups compared to the two protons in the CH₂ group yields a smaller coupling constant and sub-

sequently longer SLR times T_1 (see Eq. 6.16).

The methyl groups on the other hand show different dynamics. In addition to the structural relaxation of the whole polymer, the CH_3 group rotates in itself about the CH_3 symmetry axis. Thus, with the two processes partially overlapping, a clear T_1 minimum cannot be identified. Here, the coupling constant of the CH_3 group is comparable to the CH_2 group, because the proton distances within these groups are of about the same order of magnitude. To accomplish a comparable experimental analysis it would be necessary to replace all unwanted proton species by deuterons. Here, we also present T_1 data for which all protons were evaluated, denoted as “all”. Fig. 6.9 clearly indicates, that the total signal (all) follows the T_1 curve with the shortest relaxation time or the highest relaxation rate, as the data reflects a rate average. In conclusion, this analysis has provided us with the insight, that ^1H SLR at low temperatures may face problems with fast side-groups such as the present CH_3 group. Consequently, fully protonated systems at low temperatures will underestimate the segmental relaxation due to contributions from fast methyl dynamics.

Complementary ^2H NMR as considered in Fig. 6.9 (b) yields information about single CD bond of the different species.² An apparent difference to the provided ^1H data is that T_1 times of CH and CH_2 species hardly differ in value. Furthermore, consistent with Fig. 6.9 (a) the CH_3 group, in the ^2H calculations, displays faster dynamics. Perdeuterated PPO experiments [202–204] have also determined similar results, where two separate steps related to the methyl group and deuterons in the backbone can be identified.

6.2.5 Field-Cycling Relaxometry

In the following we discuss field-cycling (FC) data calculated from MD simulations in the range $\omega = 10^8 - 10^{13} \text{ s}^{-1}$. This frequency range does not coincide with experimentally accessible, systematically lower angular frequencies between 10^4 and 10^8 s^{-1} . While present MD is limited by the computational time window, NMR measures from high fields of superconducting magnets down to low fields with compensation of the earth field [79]. In the present study however, the apparently small overlap of these frequency windows shall not be of concern to us, because we do not aim at

² In experiments this is equivalent to the assumption that all other species are protonated

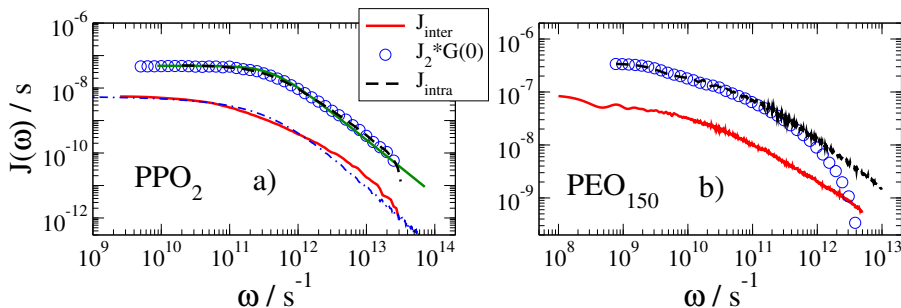


Figure 6.10.: Frequency-dependent spectral densities of the ^1H relaxation J_{intra} and J_{inter} along with their ^2H scaled counterpart $J_2(\omega)$ for (a) PPO_2 at 325 K and (b) PEO_{150} at 300 K. The normalized function $J_2(\omega)$ was multiplied by $G(0)$. J_{intra} in (a) is interpolated with a Cole-Davidson function according to Eq. 6.8 (solid green line) and J_{inter} respectively with the Fourier transform of Eq. 6.9 (dash-dotted blue line).

a direct comparison of experiment and calculated data, but a basic analysis of field-cycling data.

As we have seen in the previous sections, especially, in Sec. 6.1, one of the currently debated topics in NMR literature is the separation of intra- and intermolecular ^1H NMR parts and its utilization. To accomplish this separation, labeling as well as dilution experiments were recently developed [130–133]. In order to simplify the procedure, it is argued that ^2H relaxation holds the same basic intramolecular information as the intramolecular part of ^1H NMR. With that major assumption a much simpler approach towards the determination of $T_{1,\text{inter}}$ results. Specifically, the approach reduces a dilution sequence or extensive sample preparations to two simple NMR experiments. According to Eqs. 6.1 and 6.14, there are basic differences in the coupling constants of the two experiments, which is why we will continue discussing spectral densities. In Fig. 6.10 the three spectral densities of interest $J_2(\omega)$, from ^2H NMR, J_{intra} , and J_{inter} , from ^1H NMR, are shown for a short, glassy system and a long, polymer system. Clearly, the spectral densities of both polymers and both methods follow each other over a broad range of angular frequencies with a proportionality factor C , i.e., $J_{\text{intra}}(\omega) = C \cdot J_2(\omega)$. For PEO_{150} the validity of this statement is limited to low frequencies. Despite that, the relation may enable a good estimation of J_{intra} via ^2H relaxation since the region of interest is restricted to low frequencies, where diffusion occurs. Additionally, we may

describe the spectral density with a CD function, yielding good agreement, which furthermore affirms its previous usage. In conclusion, the proposed *modus operandi* is reasonable once the factor C is available.

Consistent with the findings of Sec. 6.2.2 and especially Fig. 6.6 the long-time behavior of G_{inter} has converted to a similar low-frequency behavior. The Fourier transform of Eq. 6.9 with its characteristic $t^{-3/2}$ behavior is transformed into a characteristic low-frequency dependence of $J_{\text{inter}}(\omega) = a - b\omega^{-0.5}$. Our simulations in Fig. 6.10 (a) agree with this prediction.

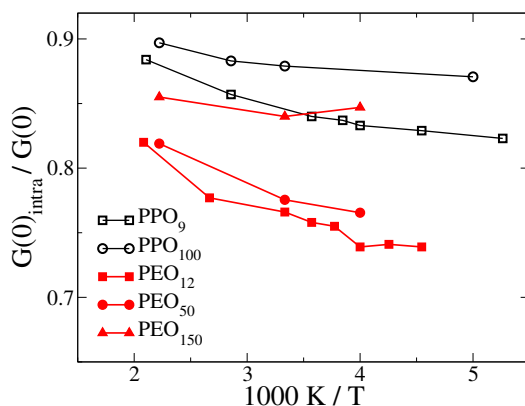


Figure 6.11.: Ratio $G_{\text{intra}}(0)/G(0)$ of various PEO and PPO chain lengths as a function of inverse temperature. The property reflects the ratio of intra and total dipolar coupling and is used to accomplish the superposition ${}^1\text{H } J_{\text{intra}}(\omega)$ and ${}^2\text{H } J_2(\omega)$.

When separating the intra- and intermolecular contributions of ${}^1\text{H}$ NMR with the help of ${}^2\text{H}$ NMR it is crucial to know the proportionality factor C. This factor clearly depends on the relative coupling constants of the ${}^1\text{H}$ and ${}^2\text{H}$ experiments concerning the spin-lattice relaxation (SLR) rate ($1/T_1$). It has proven a useful practice in our research to accomplish agreement for the spectral densities by superposing ${}^1\text{H } J_{\text{intra}}(\omega)$ with ${}^2\text{H } J_2(\omega) \cdot G_{\text{intra}}(0)$. In the present simulation approach the ratio $G_{\text{intra}}(0)/G(0)$ is calculated directly, whereas experimental practice requires tedious dilution experiments. The ratio $G_{\text{intra}}(0)/G(0)$ is a valuable information, because it also reflects the ratio between intramolecular and total dipolar coupling. Subsequently, the knowledge of the ratio enables through known ${}^1\text{H}$ and ${}^2\text{H}$ coupling constants direct superposition of J_{intra} from ${}^2\text{H}$ SLR. In order to discuss the practicality of the described approach, we provide Fig. 6.11,

which illustrates the temperature dependence of the ratio for PPO and PEO as well as various chain lengths. Clearly, the ratio depends on chain length as well as the polymer, as expected for different chemical structures.

For all investigated systems the ratio decreases towards lower temperatures. Lower temperatures result in higher proton densities and therefore smaller ^1H - ^1H distances, which intuitively increases the relevant factor $\langle 1/r^6 \rangle$. Here, we are referring to the ratio between all distances and the intramolecular contributions. While the intramolecular distances are almost unchanged, the intermolecular contribution increases through the higher density and the ratio converges toward a constant factor for low temperatures. Similarly, smaller molecular weights reduce the intramolecular contributions to the total coupling, resulting in a decreasing ratio. Fig. 6.11 implicates temperature independent ratios $G_{intra}(0)/G(0)$ for low temperatures and long chains, which is the standard case in experimental studies. Conclusively, it is possible to use a single dilution experiment at low temperatures with a long chain instead of numerous. The result of this single experiment in combination with rather simple ^2H SLR may then yield the intra- and intermolecular contributions for a broad range of molecular weights and temperatures.

Hence, this subsection showed how the combination of ^1H and ^2H NMR can be utilized to determine the intermolecular part of the ^1H . Thereby, the effort needed for dilution experiments is drastically reduced because only one dilution experiment for low temperatures and long chains can describe the relevant factor needed for the proposed evaluation.

6.2.6 Studying Translational Diffusion by Field-Cycling NMR

So far we have addressed the methods ^1H and ^2H SLR to obtain dynamic information on a molecular scale and especially the separation of intra- and intermolecular contributions. In the following we will address the intermolecular part and its practical applicability to determine translational dynamics. For this purpose, the typical MD approach is the calculation of the mean-squared displacement (MSD) of the hydrogen atoms:

$$r_H^2(t) = \langle [\mathbf{r}_i(t) - \mathbf{r}_i(0)]^2 \rangle \quad (6.22)$$

Where the determination of the full time dependence is not available, it is common to define a diffusion coefficient. The diffusion coefficient is defined via

$$r_H^2(t) = 6Dt \quad (6.23)$$

for a 3-dimensional system in its diffusive regime. The diffusion coefficient D can be determined in various experiments.³ Recently, two major approaches allow the ^1H SLR to determine diffusion coefficients as well as the better part of the subdiffusive regime of the MSD [131–133]. In one approach the diffusion coefficient is calculated in a hard-sphere model from a power law [132, 133] and in the other MSD is calculated through spin-lattice relaxation (SLR) rate. Here, we will evaluate our data according to the experimental standard and compare them to the directly determined MSD from the MD data.

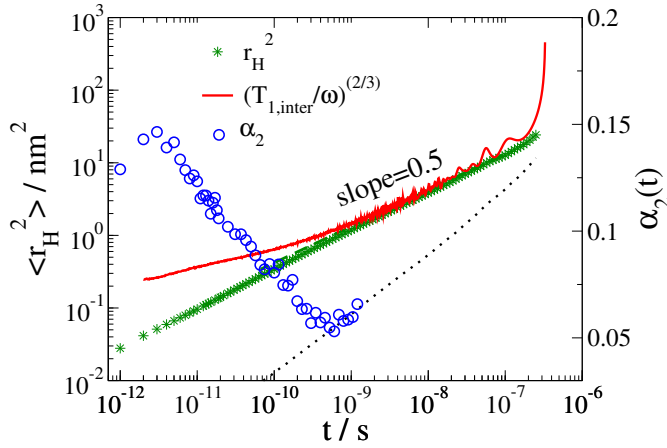


Figure 6.12.: Time-dependent mean-squared displacement of the hydrogen atoms in PPO₁₀₀ at 450 K, together with the non-Gaussian parameter $\alpha_2(t)$ for the same atoms, for Eqs. 6.22 and 6.24, respectively. Furthermore $\left(\frac{T_{1,inter}}{\omega}\right)^{2/3}$ is provided and shifted to test Eq. 6.12. Moreover, the mean-squared displacement of the center of mass is displayed as a dotted line.

For the sub-linear part of the MSD it was argued that it may be described by $r_H^2(t) \propto \left(\frac{T_{1,inter}}{\omega}\right)^{2/3}$ (see Eq. 6.12) [131]. Fig. 6.12 tests the validity of this approach for PPO₁₀₀ disclosing its limits through a direct comparison of NMR and calculated data. Evidently in the range of 10^{-9} - 10^{-7} s

³ This is possible through the Stokes-Einstein relation in Chapter 4 or the viscosity η

the time-dependent curves agree and frequency-dependent SLR may yield reasonable MSD data. However, the range of validity is by two orders of magnitude smaller than predicted by previous studies [131]. It was argued that the present approach is limited by the structural relaxation τ_α at short times and the terminal relaxation of the polymer end-to-end vector τ_{ete} at long times. Yet, with a present structural relaxation time $\tau_\alpha = 6 \times 10^{-11}$ s, the observed validity is shorter by two orders of magnitude on the short-time side.

The relation in Eq. 6.12 has been derived under the assumption of sub-linear diffusion in connection with a Gaussian propagator (see Appendix of Ref. 131). Subsequently, we study the deviation from Gaussian motion based on the non-Gaussian parameter calculated from the present MD trajectory.

$$\alpha_2(t) = \frac{3 \langle [\mathbf{r}_i(t) - \mathbf{r}_i(0)]^4 \rangle}{5 \langle [\mathbf{r}_i(t) - \mathbf{r}_i(0)]^2 \rangle^2} - 1 \quad (6.24)$$

for the hydrogen displacements of PPO₁₀₀. The angular brackets as in previous sections denote an ensemble average. Assuming a Gaussian distribution of displacements $\alpha_2(t) \equiv 0$ and subsequently all heterogeneous dynamics are indicated by $\alpha_2(t) > 0$. Previous studies have shown that the characteristic peak value of $\alpha_{2,max} = \alpha_2(t = \tau_{\alpha_2})$ is systematically smaller than the structural relaxation time τ_α and hence the assumption of Ref. 131 seemed reasonable.⁴ The findings of Fig. 6.12, however, indicate that neither the peak value of the non-Gaussian dynamics at rather short times nor the structural relaxation mark the short-side of the validity range, but rather the point of vanishing non-Gaussian motion. Only when $\alpha_2(t)$ reaches its minimum are all assumptions of the model valid and the curves agree. So far, it was shown that ¹H SLR can determine mean-squared displacement in a time range limited by the non-Gaussian dynamics of the structural relaxation for short times and the terminal relaxation of the chains end-to-end vector.

The end of this section as well as the end of the MSD is dedicated to the diffusion coefficient and its determination by ¹H FC. Following Sec. 6.1 we have introduced a model of free diffusion of hard spheres leading to Eq. 6.9. Concluding from this relation the derivation of a translation relaxation time in the hard sphere model [196] (τ_T) and with it and Eq. 6.10 the diffusion coefficient D is possible. It was proposed that the approach

⁴ see. Refs. 38, 38 and Sec. 4

| System | d [nm] | τ_T [ps] | D_{SLR} $10^{-12} [\frac{m^2}{s}]$ | D_{MSD} $10^{-12} [\frac{m^2}{s}]$ |
|------------------------------------|-------------|------------------|---|---|
| PEO ₁₂ ^{265K} | 0.2 | 10000 | 2 | 5 |
| PEO ₁₂ ^{350K} | 0.198 | 200 | 98 | 115 |
| PEO ₅₀ ^{300K} | 0.2 | 3000 | 6.7 | 8.22 |
| PEO ₁₅₀ ^{450K} | 0.2 | 90 | 222 | 50 |
| PPO ₂ ^{450K} | 0.197 | 2.5 | 7762 | 9860 |
| PPO ₉ ^{250K} | 0.196 | 18000 | 1.0 | 1.2 |
| PPO ₉ ^{300K} | 0.2 | 500 | 40 | 42 |
| PPO ₉ ^{450K} | 0.195 | 35 | 543 | 609 |
| PPO ₁₂ ^{450K} | 0.215 | 45 | 514 | 450 |
| PPO ₃₆ ^{450K} | 0.215 | 200 | 115 | 45 |
| PPO ₄₈ ^{450K} | 0.215 | 200 | 115 | 41 |
| PPO ₁₀₀ ^{450K} | 0.21 | 250 | 88 | 16.8 |

Table 6.1.: Determination of the self-diffusion coefficient for PEO and PPO of various chain lengths and temperatures with all relevant parameters. The distance of closest approach denoted as d , the fitted translational relaxation time τ_T and the resulting diffusion coefficient from SLR denoted as D_{SLR} are compared to the diffusion coefficient extracted from the diffusive part of $r_H^2(t)$. Where the distance of closest approach is extracted from $g_{HH,inter}(r)$ as described in the text.

yields correct self-diffusion coefficient in glass-forming liquids [132, 133], but data for an identical system for comparison is rare. Hence, the present MD simulations ascertain the possibility to determine the diffusion coefficients with both methods, i.e., direct calculation from MSD with MD data and indirect via T_1 and the hard sphere model, and determine all necessary boundary conditions. When fitting Eq. 6.9 to a proton correlation function $G(t)$, it is problematic to find the start value or start plateau, which is very sensitive to the distance of closest approach d . Since this value is merely a factor of the model of hard spheres, there is no clear physical meaning for polymers of increasing molecular weights. The distance of closest approach must be linked to the pair correlation function $g_{HH,inter}(r)$. $g_{HH,inter}(r)$ shows at which distances many neighboring atoms reside, while the normalization to the proton density yields $g_{HH,inter}(r) \equiv 1$ for distances of about four times the first neighbor proton distances. In order to define the distance of closest approach systematically, we have considered reason-

able values and their respective meaning in terms of $g_{HH,inter}(r)$, yielding a simple rule for the determination of d . The distance of closest approach d is therefore consistently defined as the distance where $g_{HH,inter}(r = d)$ equals 10% of the first neighbor peak.

With d well defined we may ascertain the proton density of the system N_H via an experimentally common relation [132] as:

$$10N_H = \frac{4}{3}\pi d^3 \rho_{1H} \quad (6.25)$$

With all relevant parameters known, τ_T is the only free parameter, to be fitted in Eq. 6.9. We subsequently determine $D_{SLR} = \frac{d^2}{2\tau_T}$ and compare it to its MSD counterpart D_{MSD} in Tab. 6.1. D_{MSD} is ascertained from the standard procedure $r_H^2(t) = 6D_{MSD}t$. In detail, Tab. 6.1 illustrates good agreement between D_{MSD} and D_{SLR} for short chains, where small molecules are well described as hard spheres. Moving on to longer chains then reveals a substantial and systematic overestimation of D_{SLR} compared to D_{MSD} . In addition to the obviously debatable assumption of hard spheres for larger molecules, the results in the previous section have shown that diffusive motion, e.g., in G_{inter} , is masked by polymer dynamics. In the evaluated time range large molecules are not likely to reach the limit of free diffusion, hence disabling successful application of the model.

It was thus shown that the ^1H FC relaxometry may yield reasonable diffusion coefficients, provided it has reached the long-time limit of free diffusion. Especially, for long polymers with high molecular weights and measurements at low temperatures this requires the application of very small frequencies, i.e., ultra-low magnetic fields.

6.2.7 Comparison of Computed and Experimental Data

In the previous sections we have shown that the FC NMR experiment allows extraction of dynamic data in the frequency domain. While so far we have discussed the results of MD analysis applied to NMR observables, we will start this section vice versa taking a look at FC data in the time domain. This representation is much more intuitive and the basis of any method, be it NS, NMR, Dielectric Spectroscopy (DS) or MD. For the analysis of polymer dynamics, it specifically allows us to check the exponents proposed by the Doi-Edwards model [68].

For the determination of the correlation function from NMR data the frequency-temperature superposition is used, leading to an extremely broad frequency window and finally applying a Fourier transform to a broad time window. The approach is a common tool in NMR [82, 83, 205], therefore it is not described here.

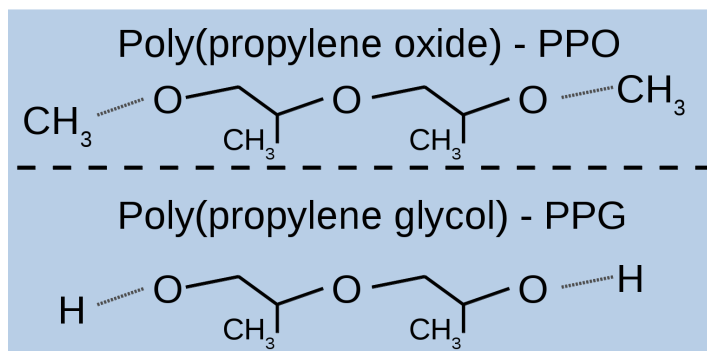


Figure 6.13.: Illustration of the chemical difference between PPO and PPG.

In order to check the regimes predicted by the Doi-Edwards model we presented the rescaled correlation function in the introduction of this chapter on a double-logarithmic scale, where power laws are visible as straight lines with a prominent slope. Specifically, the combination of the NMR and MD results enable the comparison of PPG/PPO, experiment/simulation and H-H correlation function/O-O bond vector. While the latter has already been partly discussed in Sec. 6.2.3, we will here focus on the long-time regimes and their power laws. In Fig. 6.1 we present the correlation functions resulting from ^1H FFC experiments conducted in Bayreuth [2] for PPG of various chain lengths, along with the corresponding PPO data extracted from MD simulations. Both data sets PPG and PPO experience chain length-dependent different dynamic regimes identified with local, glassy dynamics (regime 0) and the Doi-Edwards limits for Rouse dynamics (regime I) and constrained Rouse dynamics (regime II).

The comparison of FC NMR data and MD data has thereby shown that a long-time entanglement regime preceding the Rouse regime is evident. Specifically, for MD simulation our joint work in Ref. 2 has been the first chemically realistic simulation study to report entanglement. Still, some deviation between the MD and NMR data especially for short chains occurred. These deviation may be the result of several differences between the NMR and MD evaluations of the data. Following the tube-reptation

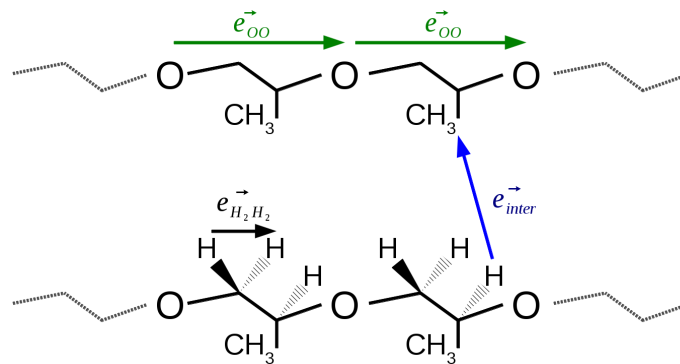


Figure 6.14.: Illustration of the vectors evaluated in NMR and MD.

model, the MD data in Fig. 6.1 was calculated for the connection vectors of the oxygen atoms. The interaction measured by ^1H NMR on the other hand reflect all proton connection vectors as we have indicated in the illustrations of Fig. 6.14. Additionally, the chemical differences considering the end groups of PPO and PPG (see Fig. 6.13) could be the source for deviations.

In Fig. 6.15 we compare the correlation functions of the experiment and simulation in further detail, for (a,b) the dimer PPO_2 and PPG_2 and (c) the largest comparable chain lengths PPO_{100} and PPG_{86} . In Ref. 2 we already showed that the NMR data for PPG_{86} matches very well with the backbone reorientation $F_{2,OO}$ in PPO_{100} , while for short chain, i.e., PPG_2 and PPO_2 $F_{2,OO}$ and the proton-proton correlation function do not match. Obviously, this deviation was identified to occur due to the missing intermolecular contributions in $F_{2,OO}$. Fig. 6.15 offers several different calculated correlation functions in order to ascertain the critical missing component. We start with the originally proposed $F_{2,OO}$, which expectedly does not resemble the long-time behavior since it lacks the intermolecular contributions leading to the final slope with $\varepsilon = 3/2$, which we have discussed in Sec. 6.2.2.

Apart from the missing intermolecular contribution, one may criticize the choice of the O-O vector, which was motivated by the fact that polymer models refer to backbone vectors, not side groups. We therefore also analyze the correlation of the hydrogen atoms, specifically the H2-H2 vector of the two hydrogens in the CH_2 group, here indicated as $F_{2,H2H2}$. Figure 6.15 shows $F_{2,H2H2}$ being much closer to the experimental data, while still missing the intermolecular contribution and long-time behavior. In the

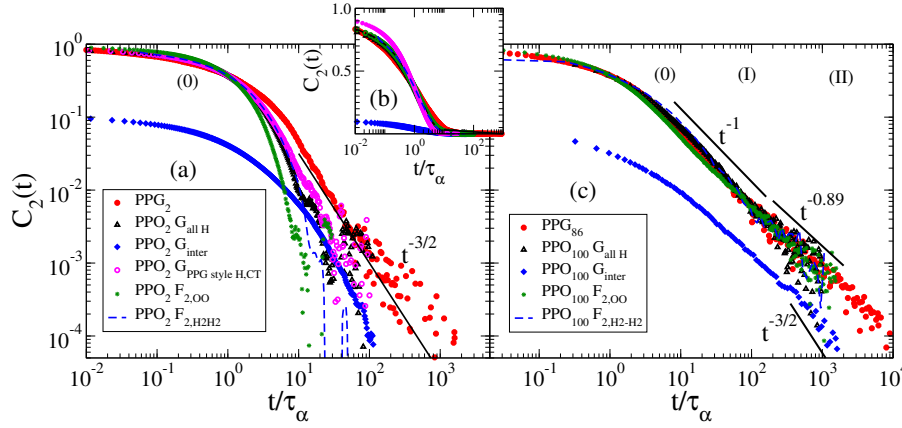


Figure 6.15.: Comparison of the proton correlation function $G(t)$ and the rotational correlation function $F_2(t)$ from experiment and simulation, here referred to as $C_2(t)$ meaning a two-time autocorrelation function. Experimental data are indicated as PPG and simulated as PPO. (a) Comparison for PPG_2 and PPO_2 on a double-logarithmic scale (b) as (a) in a semi-logarithmic representation and (c) comparison for PPG_{86} and PPO_{100} . Solid lines represent power laws of the Doi-Edwards regimes (I),(II) and the intermolecular long-time relaxation with exponent $\varepsilon = 3/2$. Details on the curve meanings see text.

next step the intermolecular particles are also considered, so that the proton proton correlation function G_{allH} as defined in Eq. 6.3 is considered. G_{allH} exhibits the missing long-time features furthermore supported by the presented intermolecular data G_{inter} . Yet, the experimental data is not in agreement with the MD data.

Notably, the dynamics of $F_{2,H2H2}$ and G_{allH} agree very well, so long as the intramolecular contribution dominates the intermolecular. Finally, we calculate a correlation $G_{PPG\ style\ H,CT}$, which disregards the proton atoms in the terminal CH_3 groups, therefore considering the terminal carbon atom CT as a proton. This analysis maps the atomic structure of PPO and its final CH_3 groups onto the PPG molecule and its final O-H groups. We observe that the PPG mapping of PPO does improve the principle trend, though still not reaching full agreement. Considering that the principle long-time behavior of all curves agree experiencing a stretched exponential and a kink to a power-law $t^{-3/2}$, we analyze a semi-logarithmic scale in Fig. 6.15(b).

The linear scale demonstrates clearly the influence of different stretching exponents in the glassy regime that results in a shift at long times. A scaling with a characteristic time τ_S defining the end of the glassy regime would therefore have resulted in better agreement at long times and completely different glassy dynamics. In sum, the short polymer chain shows us that differences in the glassy regime due to differing stretching factors are to be expected from chemical differences of PPG and PPO, while long-time dynamics match very well.

For a long polymer with a chain length close to the entanglement length $N \approx N_e$ we see in Figure 6.15(c) that all considered functions match the experimental data of PPG₈₆. This analysis therefore shows how ¹H FC experiments perfectly measure tube-reptation polymer dynamics limited only by differences in stretching factors within regime 0 and unwanted intermolecular contributions after the final relaxation indicated by $\varepsilon = 3/2$.

6.2.8 Dangling Ends Masking Regime II: Protracted Rouse

In experimental studies the observed signals will always be a superposition of contribution from different segments along the chain. When we take into account that some segments at the chain ends are rather mobile and only hindered by a covalent bond in one direction, whereas the center vectors are strongly influenced by their neighbors on both sides, differences in their dynamic behaviors are expected.

In MD simulations insight into the different dynamic behaviors are available. A. Bormuth has contributed a position-resolved orientation autocorrelation function $f_2(t, n)$ for this purpose in Ref. 2 for PPO₁₀₀, which we will here complement with data on PEO₁₅₀ and PB₂₇₅. The lower *f* here indicates the position-resolved version of F_2 in contrast to the average over all bond vectors. The position *n* denotes the number of the oxygen-oxygen bond vectors counted from the chain end towards the center and then down again, so that the two chain ends contribute to $n=1$ and the center vector to $n=50$. In Fig. 6.16 the position-resolved correlation $f_2(t, n)$ exhibits simple glassy dynamics⁵ at the chain ends $n < 7$ and develops Rouse dynamics⁶ beyond that. For the chain center $n=50$ a second regime after the Rouse regime occurs at longer times with shallower power law ($\varepsilon < 1$). The extremely reduced statistics of a position-resolved correlation function

⁵ Regime 0: stretched exponential decay

⁶ Regime I: power law $\varepsilon_I = 1$

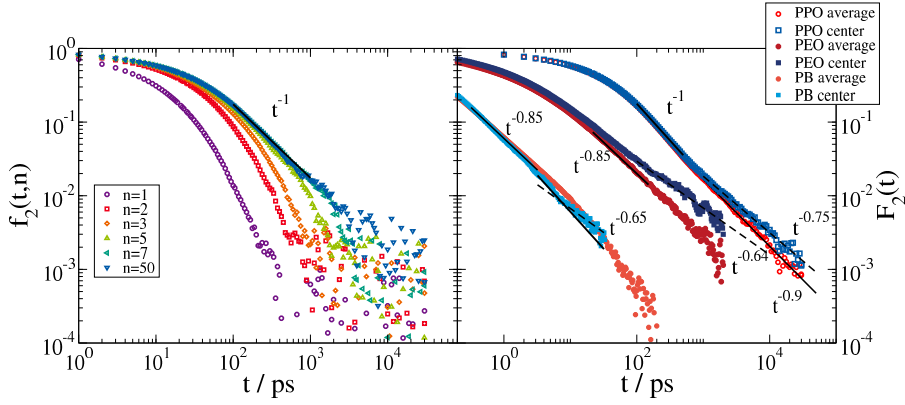


Figure 6.16.: Orientational correlation functions of the oxygen-oxygen/carbon-carbon vectors along the backbone (a) position resolved $f_2(t, n)$ with position n along the backbone (see text) (b) $F_2(t)$ averaged over all vectors or just the 40 central vectors for PB₂₇₆, PEO₁₅₀, and PPO₁₀₀ at 450 K. Analysis of PPO₁₀₀ conducted by A. Bormuth [2].

$f_2(t, n)$ does not allow us to determine a nicely defined exponent ε_{II} . Thus, in Fig. 6.16(b) we compare the usual average over all bond vectors with an average only including the 40 central bonds of the chain. We have hence excluded all those vectors which exhibit a simple glassy dynamics and reduce the expected long-time correlation within the averaging process. The included power laws in Fig. 6.16(b) illustrate the transition from the Rouse regime(I) to the constrained Rouse regime(II).

The center bond vectors reveal a distinct kink compared to the averaged curve but the magnitude of the exponent $\varepsilon = 0.75 > \varepsilon_{II} = 0.25$ is still larger than expected in the Doi-Edwards model for the infinitely long chains [68]. In addition to the previously published data for PPO₁₀₀ [2] we have supplemented Fig. 6.16(b) with data for PEO₁₀₀ and PB₂₇₆. Here, perfect agreement for the Rouse regime ($\varepsilon_I = 1$) is not reached, but the kink towards an entangled regime ($\varepsilon_{II} < 1$) is found for all three systems. To our knowledge, we have therefore presented the first observation of entanglement in atomistic MD simulations for several systems. Specifically, the lower exponent in the Rouse regime in PB and PEO is not uncommon, on the contrary the perfect agreement for PPO₁₀₀ is astonishing. Several studies [88, 206, 207] have repeatedly reported lower exponents in the Rouse regime. Mostly, the studies found the reduced Rouse exponents in MSD and spectral density, yet the implications are

also relevant in the representation of the correlation function. Recently, J. Baschnagel and coworkers [88] have therefore proposed to include hydrodynamic and viscoelastic effects into the Rouse model, which yields a reduced Rouse exponent, as found here.

We may conclude at this point that all experimentally obtained data provide evidence for a delayed onset of polymer dynamics because of fast/dangling end effects. Within the first occurrences of the Rouse regime the dynamic diversity caused by the ends masks the characteristic power law of the Rouse regime protracting establishment of the slope $\varepsilon_l = 1$. For the longer chains just so the ends mask the development of the constrained Rouse regime.

As a consequence, experimental determination of the entanglement chain length N_e or molecular mass M_e will typically yield characteristically larger values than the theory. Additionally, the different dynamics of the chain segments explain the increased stretching of the correlation functions. For short chains the correlation is a superposition of glassy dynamics resulting in mildly stretched correlations. Upon increasing chain lengths the superposition includes segments with glass dynamics from chain ends as well as Rouse and constrained Rouse dynamics from segments in the center, thus, leading to significantly stretched correlation functions.

6.3 Summary

In this chapter it has been shown that MD is a versatile tool to investigate the information content of NMR spin-lattice relaxation data on a detailed level. Specifically, close inspection of the intra- and intermolecular contributions of ^1H NMR proves to be of relevance and easily accessible via MD calculations. Considering the intramolecular part of small molecules the dynamics can be identified with rotational, glassy dynamics. The findings hence follow the assumption that NMR probes segmental relaxation and exhibits as expected the associated dynamics. The extracted correlation times were compared to other methods and found to agree reasonably well, e.g., with neutron scattering data for a scattering vector $q = 1.2\text{\AA}$. When continuing towards larger molecules the glassy dynamics are complemented by typical polymer dynamics in the long-time regime of the correlation function or the low-frequency regime of the spectral density. The polymer dynamics are then described by a power law in the time domain and its Fourier transform in the frequency domain. It is furthermore

noted that NMR results may not without further analysis be compared to polymer theories because they do not directly probe dynamics of backbone tangent vectors.

The intermolecular contributions G_{inter} and J_{inter} deviate significantly from their intramolecular counterpart. G_{inter} exhibits a long-time behavior governed by relative translational motion, resulting in a long-time power law. The findings show good agreement with predictions of a hard-sphere model, $t^{-3/2}$, [196] and are described accordingly.

Disentanglement of the intra- and intermolecular contributions is helpful [130–133] and MD calculations have shown that dilution and labeling strategies are appropriate for the task. In detail, we showed, that J_{intra} may be described via $J_2(\omega)$ from ^1H NMR, when the constant of proportionality mediating between ^1H and ^2H is determined. The proportionality was found to depend on polymer length as well as temperature and, thus, the density. For long polymers and low temperatures the proportionality was found to be almost independent of the latter, suggesting an effective experimental strategy. Experimental work often applies large polymer chains at rather low temperatures. With the strategy presented here the constant can be determined with fewer dilution or labeling experiments than before, saving experimental resources and costs.

In the present study it was hence found that the determination of the intramolecular dipolar interaction through ^2H NMR, as well as the intermolecular contribution through a subtraction, are well-suited strategies. Consistent with previous studies [130–133] it is also possible to determine translational motion, e.g., diffusion and mean-squared displacement from the intermolecular dipolar coupling. Determination of MSD was found to work well, while the proposed range of validity had to be limited on the short-time side by the decay of the non-Gaussian dynamics rather than the structural relaxation. On the low-frequency side of the relaxation dispersion, or at long times of the correlation function, it is possible to determine the self-diffusion coefficient D . In the theoretical approach via a model of hard spheres it was necessary to determine the distance of closest approach d with the help of the proton-proton pair-correlation function $g_{\text{HH}}(r)$. Here the minimum distance at which 10% of the first maximum is reached was denoted as d . The subsequent analysis with the model of hard spheres and the straightforward definition of d has shown that the distance of closest approach has to be chosen as proposed to achieve validity for the pro-

cedure. For the proposed distance of closest approach d it allows good estimations of the self-diffusion coefficient D , as long as the long-time behavior is beyond polymer specific influences.

Direct comparison between field-cycling experiments on PPG and MD simulation of PPO showed clear deviations for the glassy regime, where the stretching factor of the stretched exponential factor is significantly smaller in the experiment, which is identified as a difference between PPG and PPO rather than the method itself. Furthermore, for the long-time behavior characterizing specific polymer dynamics, a perfect agreement between the two systems is observed. While identification of the regimes 0, I and II of the Doi-Edwards model was possible, a previously reported higher exponent is found in regime II $\epsilon = 0.89 > \epsilon_{II} = 0.25$. The correct exponent is expected to emerge at longer chain lengths, because at moderate chain lengths it is masked by fast-dangling chain ends. Altogether, we would like to emphasize that the agreement between experiment and simulation in this study is very good and not just qualitatively but also quantitatively. Moreover, we have shown that the new approaches within NMR studies yield very good results for polymer dynamics and are well suited to obtain informations about diffusion and polymer dynamics, specifically in the entanglement regime.

7 Summary

In this work we have investigated the universality of the glass transition for a wide range of glass formers. Thereby, we included charged and uncharged molecular liquids with simple glassy dynamics and polymer melts showing in addition to the glass, Rouse and entanglement dynamics. We chose these diverse types of systems to ensure that our findings reflect widely universal behavior rather than system-specific properties. We have considered three major sets of simulations for the different systems. First, we studied bulk systems and focused on the relevant control parameters for the glass transition and investigated spatially heterogeneous dynamics. Furthermore, we studied confined systems and determined various definitions of length scales appearing within them. Following the theoretic studies we ascertained the experimental measurement of the quantities relevant for the glass transition by example of nuclear magnetic resonance, which is a widely-used and sophisticated method.

In bulk systems we determined which control parameters adequately describe the glass transition under variant pressure and temperature. Specifically, volume effects are properly included via TV^γ scaling with an exponent γ , which is system specific rather than universal. Likewise, TS_{conf} scaling proposed by the Adam-Gibbs theory enabled an adequate description of the glassy slowdown. We found that spatially heterogeneous dynamics are a key feature of all glass formers. Their characteristic times were shown to be related to either the structural relaxation time or the diffusion coefficient by two power laws. Such findings were only once reported before. Here, they were shown for the first time as a characteristic of a number of different glass formers studied. Furthermore, we found the breakdown of the Stokes-Einstein relation to be a feature of most glass formers. Moreover, a fractional exponent was found to be correlated with the stretched exponential decay of the correlation function and the width of the time-dependent non-Gaussian parameter $\alpha_2(t)$. The latter was thereby introduced for the first time and yields promising results so that it should be considered in future studies.

Associated with the growth of cooperatively rearranging regions in the context of spatially heterogeneous dynamics we have studied the recently proposed possibility to define adequate length scales in confinement systems.

Here, we determined dynamic and static length scales for four confinement geometries, which describe the bulk behavior of the glass transition very well. Furthermore, we define a new length scale via the width of the non-Gaussian parameter, which we introduced before and works just as well as the well-known length scales. The functionality of the length scales for the description of the bulk is found to support the Random First Order Transition theory and yields an surface exponent $\theta \leq 2$ for the tension between entropic droplets.

Investigations of the glass transition as a dynamic phenomenon are complicated because wide ranges of temperatures and time scales are involved. We studied recently-developed experimental analysis methods using nuclear magnetic resonance field-cycling relaxometry from an molecular dynamics simulation perspective, to scrutinize the validity of assumptions and procedures in studies of the glass transition and polymer dynamics. We find all common assumptions yield reasonable results. Furthermore, we propose some refined limitations of the methods. For the field-cycling technique we validate the possibility to determine mean-squared displacement in the subdiffusive regime and diffusion coefficients. Thereby, we find good agreement on a quantitative and qualitative level between nuclear magnetic resonance experiments and molecular dynamics simulations. Finally, we utilized the possibility of molecular dynamics simulation to calculate diverse observables and determined fast-dangling end effects as the origin of protracted Rouse dynamics.

Altogether, in this study we have shown that the glass transition is a universal feature inherent to a wide range of systems. Other than the glass transition itself we have identified its description via multiple control parameters, length scales and spatially heterogeneous dynamics to be common properties of all glass formers. Thereby, we have extended the knowledge of the glass transition and introduced new aspects and interesting parameters. Moreover, we have done so with chemically-realistic models of glass formers, which is an important step extending investigations of the glass transition in simple model liquids.

A Potential parameters

This chapter contains all the relevant potential parameters summarized from the relevant literature separated into the polymers and the ionic liquid.

A.1 Polymers

$$E = \frac{1}{2}k_{\alpha\beta}^{BOND}(r_{ij} - r_{\alpha\beta}^0)^2$$

| stretch | $k_{\alpha\beta}$ [kcal Å ⁻² /mol] | $r_{\alpha\beta}$ [Å] |
|-----------------------------------|---|-----------------------|
| PDMS^a | | |
| Si – O | constrained | 1.66 |
| Si – C | constrained | 2.02 |
| PB^b | | |
| CH ₂ – CH ₂ | constrained | 1.53 |
| CH – CH | constrained | 1.34 |
| CH ₂ – CH | constrained | 1.50 |
| C – H | constrained | 1.10 |
| PPO^c | | |
| C – O | 739 | 1.40 |
| C – H | 655 | 1.09 |
| C – C | 618 | 1.52 |
| PEO^d | | |
| C – O | constrained | 1.4115 |
| C – H | constrained | 1.1041 |
| C – C | constrained | 1.5075 |

Table A.1.: Bond - or stretch parameters ^a [105], ^b [106], ^c [107], ^d [108]

$$E = \frac{1}{2} k_{\alpha\beta\gamma}^{BEND} (\theta_{ijk} - \theta_{ijk}^0)^2$$

| bend | $k_{\alpha\beta\gamma}$ [kcal rad ⁻² /mol] | θ_{ijk}^0 [°] |
|---|---|----------------------|
| PDMS^a | | |
| <i>Si – O – Si</i> | 6.00 | 156.0 |
| <i>O – Si – O</i> | 183.00 | 105.6 |
| <i>O – Si – CH₃</i> | 46.00 | 109.8 |
| <i>CH₃ – Si – CH₃</i> | 72.00 | 112.4 |
| PB^b | | |
| <i>CH₂ – CH₂ – CH</i> | 115 | 111.65 |
| <i>CH – CH – CH₂</i> | 89.4 | 125.90 |
| PPO^c | | |
| <i>C – O – C*</i> | 149 | 109.23 |
| <i>C – O – C</i> | 149 | 108.33 |
| <i>O – C – H</i> | 112 | 110.07 |
| <i>O – C* – C(H₂)</i> | 119 | 107.66 |
| <i>O – C* – C(H₃)</i> | 119 | 111.17 |
| <i>O – C – C*</i> | 119 | 105.96 |
| <i>C – C – H</i> | 85.8 | 109.49 |
| <i>C – C – C</i> | 108 | 111.33 |
| <i>H – C – H</i> | 77 | 108.30 |
| PEO^d | | |
| <i>C – C – H</i> | 85.8 | 110.10 |
| <i>H – C – H</i> | 77.0 | 109.47 |
| <i>O – C – H</i> | 112.0 | 109.48 |
| <i>C – O – C</i> | 149.0 | 108.05 |
| <i>O – C – C</i> | 172.0 | 108.54 |

Table A.2.: Bending parameters ^a [105], ^b [106], ^c [107], ^d [108]

$$E = \frac{1}{2} \sum_n k_{\alpha\beta\gamma\delta}^{TORS}(n) [1 + \cos(n\phi_{ijkl})]$$

| torsion | [kcal /mol] | | | | | |
|---|-------------|--------|--------|--------|--------|--------|
| | k_1 | k_2 | k_3 | k_4 | k_5 | k_6 |
| PDMS^a | | | | | | |
| Si - O - Si - O | | | none | | | |
| Si - O - Si - C | | | none | | | |
| PB^b | | | | | | |
| CH ₂ - CH - CH - CH ₂ | | 24.2 | | | | |
| α (<i>cis</i>) | 1.033 | -0.472 | 0.554 | 0.263 | 0.346 | 0.164 |
| α (<i>trans</i>) | -0.240 | -0.730 | 1.978 | 0.082 | 0.091 | -0.056 |
| β | -0.888 | -0.619 | -3.639 | -0.066 | -0.247 | -0.190 |
| PPO^c | | | | | | |
| C - O - C* - C(H ₂) | -0.5 | -0.24 | -1.13 | | | |
| C - O - C* - C(H ₃) | -0.14 | 0.12 | | | | |
| O - C - C - O | -0.29 | 2.44 | -0.74 | | | |
| C - C* - C - O | 1.97 | 0.03 | | | | |
| C* - C - O - C | 0.485 | -0.34 | -0.34 | | | |
| O - C - C - H | | | -0.34 | | | |
| C* - C - O - C* | 3.09 | 1.02 | 0.50 | | | |
| [C*] - C - O - C* - C | -0.58 | -0.07 | -1.13 | | | |
| C - C - C - H | | | -0.28 | | | |
| H - C - C - H | | | -0.28 | | | |
| C - O - C - H | | | -0.81 | | | |
| PEO^d | | | | | | |
| O - C - C - H | | | -0.28 | | | |
| H - C - C - H | | | -0.28 | | | |
| C - O - C - H | | | -0.73 | | | |
| O - C - C - O | 0.47 | -2.43 | -0.36 | -0.95 | -0.45 | |
| C - O - C - C | 1.87 | 1.17 | 0.46 | -0.37 | | |

Table A.3.: Torsional or dihedral parameters ^a [105], ^b [106], ^c [107], ^d FF-3 [108] corrected k_3 in first two lines to -0.28

| atom | charge in e | mass in u |
|-------------------------|-------------|-----------|
| PDMS^a | | |
| <i>Si</i> | +0.5535 | 28.0860 |
| <i>O</i> | -0.4620 | 15.9990 |
| <i>CH₃</i> | -0.1075 | 15.0110 |
| PB^b | | |
| <i>CH₂</i> | 0 | 14.0000 |
| <i>CH</i> | 0 | 13.0000 |
| <i>C</i> | 0 | 12.0000 |
| <i>H</i> | 0 | 1.0000 |
| PPO^c | | |
| <i>C^{3T}</i> | -0.2327 | 12.0110 |
| <i>C²</i> | -0.1618 | 12.0110 |
| <i>C³</i> | -0.5294 | 12.0110 |
| <i>C¹</i> | +0.4264 | 12.0110 |
| <i>O^T</i> | -0.3304 | 15.9994 |
| <i>O</i> | -0.2348 | 15.9994 |
| <i>H^{3T}</i> | +0.1167 | 1.0880 |
| <i>H³</i> | +0.1400 | 1.0880 |
| <i>H²</i> | -0.0117 | 1.0880 |
| <i>H¹</i> | +0.0957 | 1.0880 |
| PEO^d | | |
| <i>C_m</i> | -0.1187 | 12.0110 |
| <i>C_e</i> | -0.0326 | 12.0110 |
| <i>O</i> | -0.2792 | 15.9994 |
| <i>H</i> | +0.0861 | 1.0880 |

Table A.4.: Partial atomic charges and mass ^a [105], ^b [106], ^c [107], ^d [108] superscripts are explained in the text.



$$E = \frac{1}{2} * \epsilon [(r_{min}/r)^{12} - 2(r_{min}/r)^6] \text{ or } E = A_{\alpha\beta} \exp(-B_{\alpha\beta} r_{ij}) - \frac{C_{\alpha\beta}}{r_{ij}^6} + \frac{q_{\alpha}q_{\beta}}{4\pi\epsilon_0 r_{ij}}$$

| non-bonded | A [kcal/mol] | B [Å ⁻¹] | C [kcalÅ ⁶ /mol] | ϵ [kcal/mol] | r _{min} [Å] |
|-----------------------------------|-----------------|-------------------------|--------------------------------|-----------------|-------------------------|
| PDMS^a | | | | | |
| Si – Si | 48390.4 | 2.84600 | 3114.97 | | |
| Si – CH ₃ | 171902.5 | 3.11910 | 2366.00 | | |
| Si – O | 33599.5 | 3.11200 | 987.38 | | |
| O – O | 46954.8 | 3.82360 | 312.98 | | |
| O – CH ₃ | 248592.1 | 3.85425 | 749.98 | | |
| CH ₃ – CH ₃ | 1319293.3 | 3.88670 | 1797.12 | | |
| PB^b | | | | | |
| CH ₂ – CH ₂ | | | | 0.0936 | 4.500 |
| CH – CH | | | | 0.1000 | 3.800 |
| CH ₂ – CH | | | | 0.1015 | 4.257 |
| PPO^c | | | | | |
| C – C | 14976 | 3.090 | 640.8 | | |
| O – O | 75846 | 4.063 | 398.9 | | |
| H – H | 2650 | 3.740 | 27.4 | | |
| C – H | 4320 | 3.415 | 138.2 | | |
| O – C | 33702 | 3.577 | 505.6 | | |
| O – H | 14176 | 3.902 | 104.5 | | |
| PEO^d | | | | | |
| C – C | 14976.0 | 3.0900 | 637.6 | | |
| O – O | 75844.8 | 4.0630 | 396.9 | | |
| H – H | 2649.6 | 3.7400 | 27.22 | | |
| C – H | 4320.0 | 3.4150 | 137.6 | | |
| O – C | 33702.4 | 3.5770 | 503.0 | | |
| O – H | 14176.0 | 3.9015 | 104.0 | | |

Table A.5.: Non-bonded interaction parameters ^a [105], ^b [106], ^c [107], ^d two-body-FF [108].

A.2 Ionic Liquid

The force field of bmim PF₆ is unfortunately not described in a single study. The state-of-the-art parameter set is given through charges in Ref. 110, coulomb interactions in Ref. 109 and PF₆ details in Refs. 111 and Refs. 112.

| Atom | $q[e]$ | $m[u]$ | $\sigma[\text{nm}]$ | $\epsilon[\text{kJ mol}^{-1}]$ |
|----------------|--------|---------|---------------------|--------------------------------|
| C ₁ | -0,089 | 12,011 | 0,350 | 0,276 15 |
| C ₂ | -0,038 | 12,011 | 0,350 | 0,276 15 |
| C _R | 0,060 | 12,011 | 0,355 | 0,292 89 |
| C _S | -0,038 | 12,011 | 0,350 | 0,276 15 |
| C _T | -0,065 | 12,011 | 0,355 | 0,292 89 |
| C _W | -0,020 | 12,011 | 0,350 | 0,276 15 |
| H _A | 0,096 | 1,008 | 0,192 | 0,125 53 |
| H _C | 0,026 | 1,008 | 0,172 | 0,125 53 |
| H ₁ | 0,105 | 1,008 | 0,250 | 0,125 53 |
| N _A | 0,052 | 14,0067 | 0,325 | 0,711 31 |
| P | 0,580 | 30,9738 | 0,394 | 0,8368 |
| F | -0,230 | 18,9984 | 0,3118 | 0,2552 |

Table A.6.: Parameters of the Lennard-Jones potential for the non-bonded interactions of bmim PF₆ adapted from Ref. 123.

| Bonds | b_0 [nm] | k_b [kJmol ⁻¹ nm ⁻²] | |
|---|----------------|---|---------------------------------------|
| C _R - H _A | 0.108 | const. | |
| C _W - H _A | 0.108 | const. | |
| C* - H* | 0.109 | const. | |
| C _R - N _A | 0.1315 | 1.996 · 10 ⁵ | |
| C _W - N _A | 0.1378 | 1.787 · 10 ⁵ | |
| C _W - C _W | 0.1342 | 2.176 · 10 ⁵ | |
| N _A - C ₁ | 0.1466 | 1.410 · 10 ⁵ | |
| C* - C* | 0.1529 | 1.121 · 10 ⁵ | |
| Bends | Θ_0 [°] | k_Θ [kJmol ⁻¹ rad ⁻²] | |
| C _W - N _A - C _R | 108.0 | 2.926 · 10 ² | |
| C _W - N _A - C ₁ | 125.6 | 2.926 · 10 ² | |
| C _R - N _A - C ₁ | 126.4 | 2.926 · 10 ² | |
| N _A - C _R - H _A | 125.1 | 1.463 · 10 ² | |
| N _A - C _R - N _A | 109.8 | 2.926 · 10 ² | |
| N _A - C _W - C _W | 107.1 | 2.926 · 10 ² | |
| N _A - C _W - H _A | 122.0 | 1.463 · 10 ² | |
| C _W - C _W - H _A | 130.9 | 1.463 · 10 ² | |
| N _A - C* - H* | 110.7 | 3.132 · 10 ² | |
| C* - C* - H* | 110.7 | 3.132 · 10 ² | |
| N _A - C* - C* | 112.7 | 4.184 · 10 ² | |
| C* - C* - C* | 112.7 | 4.184 · 10 ² | |
| Torsions | C ₀ | C ₁ | C ₂ [kJmol ⁻¹] |
| C _W - N _A - C ₁ - H ₁ | 0 | 0 | 0.55 |
| C _R - N _A - C ₁ - H ₁ | 0 | 0 | 0 |
| C _W - N _A - C ₁ - C ₂ | -5.76 | 4.43 | 0.877 |
| C _R - N _A - C ₁ - C ₂ | -3.23 | 0 | 0 |
| N _A - C ₁ - C ₂ - C _S | 0.738 | -0.681 | 1.02 |
| N _A - C ₁ - C ₂ - C _T | 0.738 | -0.681 | 1.02 |
| N _A - C ₁ - C ₂ - H _C | 0 | 0 | 0 |
| C* - C* - C* - H* | 0 | 0 | 1.531 |
| H* - C* - C* - H* | 0 | 0 | 1.331 |
| C* - C* - C* - C* | 0.728 | -0.657 | 1.167 |
| X - N _A - C _R - X | 0 | 19.46 | 0 |
| X - C _W - C _W - X | 0 | 44.98 | 0 |
| X - N _A - C _W - X | 0 | 12.55 | 0 |
| X - N _A - X - X | 0 | 8.37 | 0 |
| X - C _W - X - X | 0 | 9.2 | 0 |
| X - C _R - X - X | 0 | 9.2 | 0 |

Table A.7.: Bonded parameters for the bmim-PF₆ force field. C* is here a dummy for C₁, C₂, C₃, C_T and H* respectively for H₁ and H_C. X refers to an arbitrary atom adapted from Ref. 123.



B Complementary data

B.1 Bulk: Hyperscaling for Various Chain Lengths and Pressures

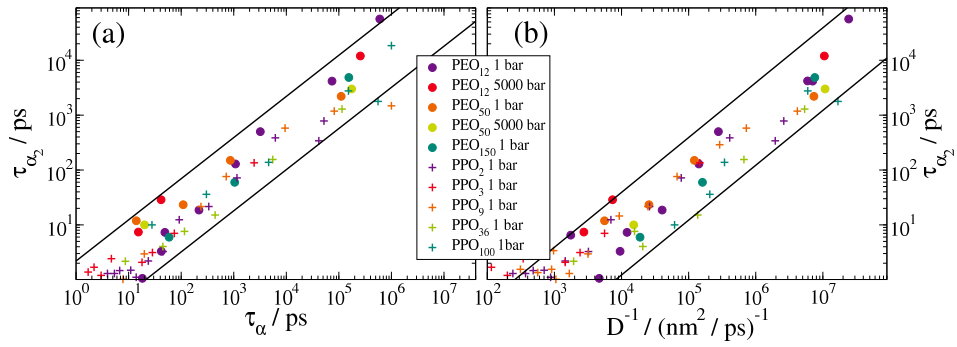


Figure B.1.: The maximum times of the non-Gaussian parameter α_2 as a function of (a) τ_α and (b) D^{-1} for PEO and PPO of variant chain lengths and pressure. The solid lines represent an exponent of (a) $\nu = 0.75$ and (b) $\nu = 1.0$.

B.2 Confinement: Hyperscaling of Characteristic SHD Times

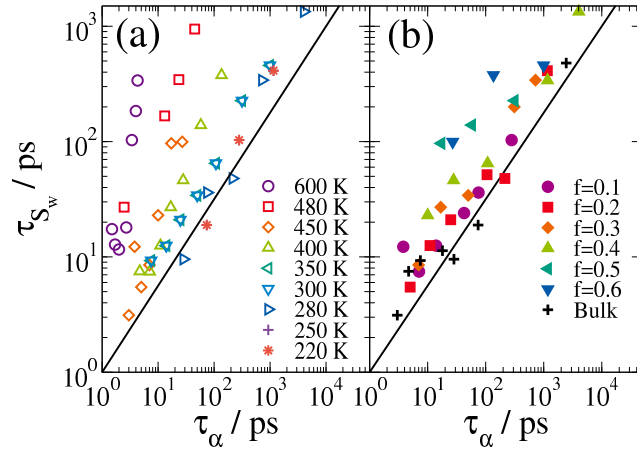


Figure B.2.: Peak time of the cluster size $S_w(t)$ as a function of the relaxation time τ_α for the PPO₃-RP system at different temperatures and fractions of pinned particles f . Panel (a) open symbols indicate data sets of same T different f . Panel (b) full symbols indicate data sets of same f different T . Solid line represents a power law of slope 0.75

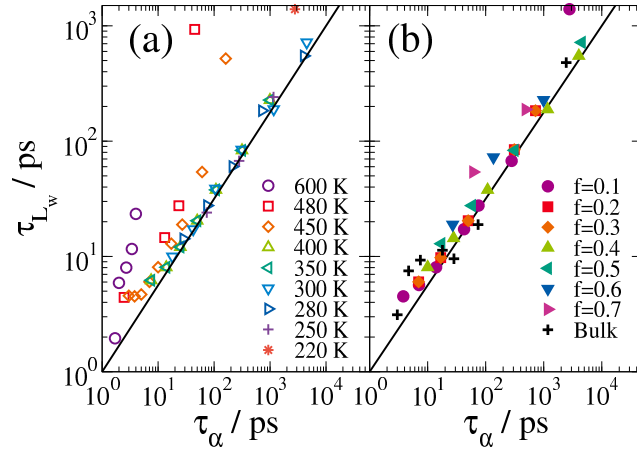


Figure B.3.: Peak time of the string size $L_w(t)$ as a function of the relaxation time τ_α complementary to previous plot.

Bibliography

- [1] F. Klameth, P. Henritzi, and M. Vogel, "Static and dynamic length scales in supercooled liquids: Insights from molecular dynamics simulations of water and tri-propylene oxide," *The Journal of Chemical Physics*, vol. 140, no. 14, 2014.
- [2] A. Bormuth, M. Hofmann, P. Henritzi, M. Vogel, and E. A. Rössler, "Chain-Length Dependence of Polymer Dynamics: A Comparison of Results from Molecular Dynamics Simulations and Field-Cycling 1H NMR," *Macromolecules*, vol. 46, no. 19, pp. 7805–7811, 2013.
- [3] W. Kauzmann, "The nature of the glassy state and the behavior of liquids at low temperatures.," *Chemical Reviews*, vol. 43, no. 2, pp. 219–256, 1948.
- [4] C. A. Angell, "Formation of glasses from liquids and biopolymers," *Science*, vol. 267, no. 5206, pp. 1924–1935, 1995.
- [5] G. Adam and J. H. Gibbs, "On the temperature dependence of cooperative relaxation properties in glass-forming liquids," *The Journal of Chemical Physics*, vol. 43, p. 139, 1965.
- [6] H. Vogel, "The law of the relationship between viscosity of liquids and the temperature," *Zeitschrift für Physik*, vol. 22, p. 645, 1921.
- [7] G. S. Fulcher, "Analysis of recent measurements of the viscosity of glasses," *Journal of the American Ceramic Society*, vol. 8, no. 6, pp. 339–355, 1925.
- [8] G. Tammann and W. Hesse, "Die Abhängigkeit der Viscosität von der Temperatur bei unterkühlten Flüssigkeiten," *Zeitschrift für anorganische und allgemeine Chemie*, vol. 156, no. 1, pp. 245–257, 1926.
- [9] J. P. Garrahan and D. Chandler, "Geometrical Explanation and Scaling of Dynamical Heterogeneities in Glass Forming Systems," *Physical Review Letters*, vol. 89, p. 035704, Jul 2002.
- [10] W. Kob, C. Donati, S. J. Plimpton, P. H. Poole, and S. C. Glotzer, "Dynamical Heterogeneities in a Supercooled Lennard-Jones Liquid," *Physical Review Letters*, vol. 79, pp. 2827–2830, Oct 1997.

-
-
- [11] B. Doliwa and A. Heuer, “Cage Effect, Local Anisotropies, and Dynamic Heterogeneities at the Glass Transition: A Computer Study of Hard Spheres,” *Physical Review Letters*, vol. 80, pp. 4915–4918, Jun 1998.
- [12] C. Donati, S. C. Glotzer, and P. H. Poole, “Growing Spatial Correlations of Particle Displacements in a Simulated Liquid on Cooling toward the Glass Transition,” *Physical Review Letters*, vol. 82, pp. 5064–5067, Jun 1999.
- [13] C. Donati, S. C. Glotzer, P. H. Poole, W. Kob, and S. J. Plimpton, “Spatial correlations of mobility and immobility in a glass-forming Lennard-Jones liquid,” *Physical Review E*, vol. 60, pp. 3107–3119, Sep 1999.
- [14] C. Bennemann, C. Donati, J. Baschnagel, and S. C. Glotzer, “Growing range of correlated motion in a polymer melt on cooling towards the glass transition,” *Nature*, vol. 399, no. 6733, pp. 246–249, 1999.
- [15] S. C. Glotzer, V. N. Novikov, and T. B. Schröder, “Time-dependent, four-point density correlation function description of dynamical heterogeneity and decoupling in supercooled liquids,” *The Journal of Chemical Physics*, vol. 112, no. 2, pp. 509–512, 2000.
- [16] Y. Gebremichael, T. B. Schröder, F. W. Starr, and S. C. Glotzer, “Spatially correlated dynamics in a simulated glass-forming polymer melt: Analysis of clustering phenomena,” *Physical Review E*, vol. 64, p. 051503, Oct 2001.
- [17] Y. Gebremichael, M. Vogel, and S. C. Glotzer, “Particle dynamics and the development of string-like motion in a simulated monoatomic supercooled liquid,” *The Journal of Chemical Physics*, vol. 120, no. 9, pp. 4415–4427, 2004.
- [18] C. Donati, J. F. Douglas, W. Kob, S. J. Plimpton, P. H. Poole, and S. C. Glotzer, “Stringlike Cooperative Motion in a Supercooled Liquid,” *Physical Review Letters*, vol. 80, pp. 2338–2341, Mar 1998.
- [19] M. Aichele, Y. Gebremichael, F. W. Starr, J. Baschnagel, and S. C. Glotzer, “Polymer-specific effects of bulk relaxation and stringlike correlated motion in the dynamics of a supercooled polymer melt,” *The Journal of Chemical Physics*, vol. 119, no. 10, pp. 5290–5304, 2003.

-
- [20] J. Qian, R. Hentschke, and A. Heuer, "Dynamic heterogeneities of translational and rotational motion of a molecular glass former from computer simulations," *The Journal of Chemical Physics*, vol. 110, no. 9, pp. 4514–4522, 1999.
- [21] N. Giovambattista, S. V. Buldyrev, F. W. Starr, and H. E. Stanley, "Connection between Adam-Gibbs Theory and Spatially Heterogeneous Dynamics," *Physical Review Letters*, vol. 90, p. 085506, Feb 2003.
- [22] M. Vogel and S. C. Glotzer, "Spatially heterogeneous dynamics and dynamic facilitation in a model of viscous silica," *Physical Review Letters*, vol. 92, p. 255901, Jun 2004.
- [23] M. Vogel and S. C. Glotzer, "Temperature dependence of spatially heterogeneous dynamics in a model of viscous silica," *Physical Review E*, vol. 70, p. 061504, Dec 2004.
- [24] V. Teboul, A. Monteil, L. Fai, A. Kerrache, and S. Maabou, "An investigation of string-like cooperative motion in a strong network glass-former," *The European Physical Journal B - Condensed Matter and Complex Systems*, vol. 40, no. 1, pp. 49–54, 2004.
- [25] J. Cardy, *Scaling and renormalization in statistical physics*, vol. 5. Cambridge University Press, 1996.
- [26] A. Montanari and G. Semerjian, "Rigorous inequalities between length and time scales in glassy systems," *Journal of statistical physics*, vol. 125, no. 1, pp. 23–54, 2006.
- [27] E. Ising, "Beitrag zur theorie des ferromagnetismus," *Zeitschrift für Physik A Hadrons and Nuclei*, vol. 31, no. 1, pp. 253–258, 1925.
- [28] A. Cavagna, "Supercooled liquids for pedestrians," *Physics Reports*, vol. 476, no. 4, pp. 51–124, 2009.
- [29] W. Götze, *Complex Dynamics of Glass-Forming Liquids: A Mode-Coupling Theory*, vol. 143. Oxford University Press, 2008.
- [30] V. Lubchenko and P. G. Wolynes, "Theory of Structural Glasses and Supercooled Liquids," *Annual Review of Physical Chemistry*, vol. 58, no. 1, pp. 235–266, 2007. PMID: 17067282.
- [31] K. Binder and W. Kob, *Glassy materials and disordered solids: An introduction to their statistical mechanics*. World Scientific, 2011.

-
-
- [32] W. Gotze and L. Sjogren, "Relaxation processes in supercooled liquids," *Reports on Progress in Physics*, vol. 55, no. 3, p. 241, 1992.
- [33] M. Fuchs, W. Götze, and M. R. Mayr, "Asymptotic laws for tagged-particle motion in glassy systems," *Physical Review E*, vol. 58, no. 3, p. 3384, 1998.
- [34] R. Casalini, S. Capaccioli, M. Lucchesi, P. A. Rolla, and S. Corezzi, "Pressure dependence of structural relaxation time in terms of the Adam-Gibbs model," *Physical Review E*, vol. 63, p. 031207, Feb 2001.
- [35] R. Richert and C. Angell, "Dynamics of glass-forming liquids. v. on the link between molecular dynamics and configurational entropy," *Journal of Chemical Physics*, vol. 108, pp. 9016–9026, 1998.
- [36] A. Scala, F. W. Starr, E. La Nave, F. Sciortino, and H. E. Stanley, "Configurational entropy and diffusivity of supercooled water," *Nature*, vol. 406, no. 6792, pp. 166–169, 2000.
- [37] R. J. Speedy, "The hard sphere glass transition," *Molecular Physics*, vol. 95, no. 2, pp. 169–178, 1998.
- [38] M. Vogel, "Conformational and Structural Relaxations of Poly(ethylene oxide) and Poly(propylene oxide) Melts: Molecular Dynamics Study of Spatial Heterogeneity, cooperativity, and Correlated Forward-Backward Motion," *Macromolecules*, vol. 41, pp. 2949–2958, 2008.
- [39] M. Vogel and S. C. Glotzer, "Temperature dependence of spatially heterogeneous dynamics in a model of viscous silica," *Physical Review E*, vol. 70, p. 061504, Dec 2004.
- [40] S. C. Glotzer, "Spatially heterogeneous dynamics in liquids: insights from simulation," *Journal of Non-Crystalline Solids*, vol. 274, no. 1, pp. 342–355, 2000.
- [41] T. Kirkpatrick and P. Wolynes, "Connections between some kinetic and equilibrium theories of the glass transition," *Physical Review A*, vol. 35, no. 7, p. 3072, 1987.
- [42] T. Kirkpatrick and P. Wolynes, "Stable and metastable states in mean-field potts and structural glasses," *Physical Review B*, vol. 36, no. 16, p. 8552, 1987.

-
-
- [43] T. Kirkpatrick and D. Thirumalai, “Mean-field soft-spin potts glass model: Statics and dynamics,” *Physical Review B*, vol. 37, no. 10, p. 5342, 1988.
- [44] D. Thirumalai and T. Kirkpatrick, “Mean-field potts glass model: Initial-condition effects on dynamics and properties of metastable states,” *Physical Review B*, vol. 38, no. 7, p. 4881, 1988.
- [45] T. Kirkpatrick, D. Thirumalai, and P. G. Wolynes, “Scaling concepts for the dynamics of viscous liquids near an ideal glassy state,” *Physical Review A*, vol. 40, no. 2, p. 1045, 1989.
- [46] V. Lubchenko and P. G. Wolynes, “Theory of aging in structural glasses,” *The Journal of chemical physics*, vol. 121, no. 7, pp. 2852–2865, 2004.
- [47] X. Xia and P. G. Wolynes, “Diffusion and the mesoscopic hydrodynamics of supercooled liquids,” *The Journal of Physical Chemistry B*, vol. 105, no. 28, pp. 6570–6573, 2001.
- [48] L. Berthier and J. P. Garrahan, “Nontopographic description of inherent structure dynamics in glassformers,” *The Journal of Chemical Physics*, vol. 119, no. 8, pp. 4367–4371, 2003.
- [49] J. P. Garrahan and D. Chandler, “Coarse-grained microscopic model of glass formers,” *Proceedings of the National Academy of Sciences*, vol. 100, no. 17, pp. 9710–9714, 2003.
- [50] L. Berthier and J. P. Garrahan, “Real space origin of temperature crossovers in supercooled liquids,” *Physical Review E*, vol. 68, p. 041201, Oct 2003.
- [51] S. Whitelam, L. Berthier, and J. P. Garrahan, “Dynamic criticality in glass-forming liquids,” *Physical Review Letters*, vol. 92, no. 18, p. 185705, 2004.
- [52] G. H. Fredrickson and H. C. Andersen, “Kinetic Ising model of the glass transition,” *Physical Review Letters*, vol. 53, no. 13, p. 1244, 1984.
- [53] J. Jäckle and S. Eisinger, “A hierarchically constrained kinetic ising model,” *Zeitschrift für Physik B*, vol. 84, no. 1, pp. 115–124, 1991.
- [54] M. Phillips, A. Barlow, and J. Lamb, “Relaxation in liquids: a defect-diffusion model of viscoelasticity,” *Proceedings of the Royal Society of*

London. A. Mathematical and Physical Sciences, vol. 329, no. 1577, pp. 193–218, 1972.

- [55] G. H. Fredrickson and H. C. Andersen, “Facilitated kinetic ising models and the glass transition,” *The Journal of Chemical Physics*, vol. 83, no. 11, pp. 5822–5831, 1985.
- [56] M. N. Bergroth, M. Vogel, and S. C. Glotzer, “Examination of dynamic facilitation in molecular dynamics simulations of glass-forming liquids,” *The Journal of Physical Chemistry B*, vol. 109, no. 14, pp. 6748–6753, 2005.
- [57] A. C. Pan, J. P. Garrahan, and D. Chandler, “Heterogeneity and growing length scales in the dynamics of kinetically constrained lattice gases in two dimensions,” *Physical Review E*, vol. 72, p. 041106, Oct 2005.
- [58] G. Biroli, S. Karmakar, and I. Procaccia, “Comparison of Static Length Scales Characterizing the Glass Transition,” *Physical Review Letters*, vol. 111, no. 16, p. 165701, 2013.
- [59] G. M. Hocky, T. E. Markland, and D. R. Reichman, “Growing point-to-set length scale correlates with growing relaxation times in model supercooled liquids,” *Physical Review Letters*, vol. 108, no. 22, p. 225506, 2012.
- [60] B. Charbonneau, P. Charbonneau, and G. Tarjus, “Geometrical frustration and static correlations in a simple glass former,” *Physical Review Letters*, vol. 108, no. 3, p. 035701, 2012.
- [61] P. Charbonneau and G. Tarjus, “Decorrelation of the static and dynamic length scales in hard-sphere glass formers,” *Physical Review E*, vol. 87, no. 4, p. 042305, 2013.
- [62] G. Biroli, J.-P. Bouchaud, A. Cavagna, T. Grigera, and P. Verrocchio, “Thermodynamic signature of growing amorphous order in glass-forming liquids,” *Nature Physics*, vol. 4, no. 10, pp. 771–775, 2008.
- [63] L. Berthier and W. Kob, “Static point-to-set correlations in glass-forming liquids,” *Physical Review E*, vol. 85, no. 1, p. 011102, 2012.
- [64] W. Kob, S. Roldán-Vargas, and L. Berthier, “Non-monotonic temperature evolution of dynamic correlations in glass-forming liquids,” *Nature Physics*, vol. 8, no. 2, pp. 164–167, 2012.

-
- [65] B. Hanson, V. Pryamitsyn, and V. Ganesan, "Molecular mass dependence of point-to-set correlation length scale in polymers," *The Journal of Chemical Physics*, vol. 137, p. 084904, 2012.
- [66] P. E. Rouse, "A theory of the linear viscoelastic properties of dilute solutions of coiling polymers," *The Journal of Chemical Physics*, vol. 21, p. 1273, 1953.
- [67] P. G. de Gennes, "Reptation of a polymer chain in the presence of fixed obstacles," *The Journal of Chemical Physics*, vol. 55, pp. 572–579, 1971.
- [68] M. Doi and S. F. Edwards, *The Theory of Polymer Dynamics*. Oxford University Press, 1988.
- [69] G. Strobl, *The Physics of Polymers*. Springer, 1996.
- [70] Science NET. http://www.sciencenet.cn/m/user_content.aspx?id=348452, 2014.
- [71] B. H. Zimm, "Dynamics of Polymer Molecules in Dilute Solution: Viscoelasticity, Flow Birefringence and Dielectric Loss," *The Journal of Chemical Physics*, vol. 24, p. 269, 1956.
- [72] R. H. Boyd and G. Smith, *Polymer Dynamics and Relaxation*. Cambridge University Press, 2007.
- [73] S. Pahl, G. Fleischer, F. Fujara, and B. Geil, "Anomalous segment diffusion in polydimethylsiloxane melts," *Macromolecules*, vol. 30, no. 5, pp. 1414–1418, 1997.
- [74] D. Kruk, A. Herrmann, and E. Rössler, "Field-cycling NMR relaxometry of viscous liquids and polymers," *Progress in Nuclear Magnetic Resonance Spectroscopy*, vol. 63, no. 0, pp. 33–64, 2012.
- [75] R. Kimmich and N. Fatkullin, "Polymer chain dynamics and nmr," *Advances in Polymer Science.*, vol. 170, pp. 1–114, 2004.
- [76] R. Kimmich and E. Anzardo, "Field-cycling nmr relaxometry," *Progress in Nuclear Magnetic Resonance Spectroscopy*, vol. 44, no. 3-4, pp. 257 – 320, 2004.
- [77] E. Vaca Chávez and K. Saalwächter, "Time-domain nmr observation of entangled polymer dynamics: Universal behavior of flexible homopolymers and applicability of the tube model," *Macromolecules*, vol. 44, no. 6, pp. 1549–1559, 2011.

-
- [78] F. V. Chávez and K. Saalwächter, “NMR Observation of entangled polymer dynamics: tube model predictions and constraint release,” *Physical Review Letters*, vol. 104, no. 19, p. 198305, 2010.
- [79] A. Herrmann, B. Kresse, J. Gmeiner, A. F. Privalov, D. Kruk, F. Fajara, and E. A. Rössler, “Protracted Crossover to Reptation Dynamics: A Field Cycling 1H NMR Study Including Extremely Low Frequencies,” *Macromolecules*, vol. 45, no. 3, pp. 1408–1416, 2012.
- [80] A. Bormuth, P. Henritzi, and M. Vogel, “Chain-Length Dependence of the Segmental Relaxation in Polymer Melts: Molecular Dynamics Simulation Studies on Poly(propylene oxide),” *Macromolecules*, vol. 43, no. 21, pp. 8985–8992, 2010.
- [81] W. Paul, G. Smith, D. Y. Yoon, B. Farago, S. Rathgeber, A. Zirkel, L. Willner, and D. Richter, “Chain motion in an unentangled polyethylene melt: A critical test of the rouse model by molecular dynamics simulations and neutron spin echo spectroscopy,” *Physical Review Letters*, vol. 80, no. 11, p. 2346, 1998.
- [82] S. Kariyo, A. Brodin, C. Gainaru, A. Herrmann, J. Hintermeyer, H. Schick, V. N. Novikov, and E. A. Rössler, “From Simple Liquid to Polymer Melt. Glassy and Polymer Dynamics Studied by Fast Field Cycling NMR Relaxometry: Rouse Regime,” *Macromolecules*, vol. 41, no. 14, pp. 5322–5332, 2008.
- [83] M. Hofmann, A. Herrmann, A. Abou Elfadl, D. Kruk, M. Wohlfahrt, and E. A. Rössler, “Glassy, Rouse, and Entanglement Dynamics As Revealed by Field Cycling 1H NMR Relaxometry,” *Macromolecules*, vol. 45, no. 5, pp. 2390–2401, 2012.
- [84] P. Henritzi, “A molecular dynamics simulation study of polymers under pressure,” Master’s thesis, TU Darmstadt, Germany, 2011.
- [85] P. Henritzi, D. Bedrov, G. Smith, and M. Vogel, “Influence of pressure on deviations of chain dynamics from the rouse model: A molecular dynamics simulation study of poly(dimethylsiloxane) and polybutadiene melts,” Poster session presented at: CPP 23.8: Poster, DPG Frühjahrstagung, 28th March, 2012.
- [86] A. Arbe, M. Monkebusch, and J. Stellbrink, “Origin of Internal Viskosity Effects in Flexible Polymers: A Comparative Neutron Spin-Echo and Light scattering Study on Poly(dimethylsiloxane) and Poly(isobutylene),” *Macromolecules*, vol. 34, pp. 1281–1290, 2001.

-
- [87] A. Bormuth, *Untersuchung der Polymerdynamik in Abhängigkeit von Kettenlänge, Temperatur und Druck mit Hilfe von Molekulardynamik Simulationen*. PhD thesis, Technische Universität Darmstadt, Darmstadt, Germany, 2012.
- [88] J. Farago, H. Meyer, J. Baschnagel, and A. Semenov, “Hydrodynamic and viscoelastic effects in polymer diffusion,” *Journal of Physics: Condensed Matter*, vol. 24, no. 28, p. 284105, 2012.
- [89] P. Henritzi, A. Bormuth, and M. Vogel, “Interpretation of 1H and 2H spin–lattice relaxation dispersions: Insights from molecular dynamics simulations of polymer melts,” *Solid State Nuclear Magnetic Resonance*, vol. 54, no. 0, pp. 32–40, 2013.
- [90] U. Tracht, M. Wilhelm, A. Heuer, and H. W. Spiess, “Combined Reduced 4D 13C Exchange and 1H Spin Diffusion Experiment for Determining the Length Scale of Dynamic Heterogeneities,” *Journal of Magnetic Resonance*, vol. 140, no. 2, pp. 460–470, 1999.
- [91] M. Parrinello and A. Rahman, “Polymorphic transitions in single crystals: A new molecular dynamics method,” *Journal of Applied Physics*, vol. 52, no. 12, pp. 7182–7190, 1981.
- [92] S. Nose and M. Klein, “Constant pressure molecular dynamics for molecular systems,” *Molecular Physics*, vol. 50, pp. 1055–1076(22), 10 December 1983.
- [93] H. J. Berendsen, D. van der Spoel, and R. van Drunen, “GROMACS: A message-passing parallel molecular dynamics implementation,” *Computer Physics Communications*, vol. 91, no. 1, pp. 43–56, 1995.
- [94] S. Nosé, “A unified formulation of the constant temperature molecular dynamics methods,” *The Journal of Chemical Physics*, vol. 81, p. 511, 1984.
- [95] W. G. Hoover, “Canonical dynamics: Equilibrium phase-space distributions,” *Physical Review A*, vol. 31, pp. 1695–1697, 1985.
- [96] T. Darden, D. York, and L. Pederson, “Particle mesh Ewald: An N log (N) method for Ewald sums in large systems,” *The Journal of Chemical Physics*, vol. 98, p. 10089, 1993.
- [97] P. E. Ewald, “Die Berechnung optischer und elektrostatischer Gitterpotentiale,” *Annals of Physics*, vol. 369, pp. 253–287, 1921.

-
- [98] H. J. C. Berendsen, D. van der Spoel, and R. van Drunen, "GROMACS: A message-passing parallel molecular dynamics implementation," *Computer Physics Communications*, vol. 91, no. 1-3, pp. 43–56, 1995.
- [99] E. Lindahl, B. Hess, and D. van der Spoel, "GROMACS 3.0: a package for molecular simulation and trajectory analysis," *Journal of Molecular Modeling*, vol. 7, pp. 306–317, 2001.
- [100] D. Van Der Spoel, E. Lindahl, B. Hess, G. Groenhof, A. E. Mark, and H. J. C. Berendsen, "GROMACS: Fast, flexible, and free," *Journal of Computational Chemistry*, vol. 26, no. 16, pp. 1701–1718, 2005.
- [101] B. Hess, C. Kutzner, D. van der Spoel, and E. Lindahl, "GROMACS 4: Algorithms for Highly Efficient, Load-Balanced, and Scalable Molecular Simulation," *Journal of Chemical Theory and Computation*, vol. 4, pp. 435–447, 2008.
- [102] J. E. Jones, "On the Determination of Molecular Fields. II. From the Equation of State of a Gas," *Proceedings of the Royal Society of London. Series A. Mathematical and Physical Sciences*, vol. 106, pp. 463–477, 1924.
- [103] R. A. Buckingham, "The Classical Equation of State of Gaseous Helium, Neon and Argon," *Proceedings of the Royal Society of London. Series A. Mathematical and Physical Sciences*, vol. 168, no. 933, pp. 264–283, 1938.
- [104] M. O. Courseware. http://ocw.mit.edu/ans7870/8/8.02T/f04/visualizations/electrostatics/images/19-Molecule_f100_320.jpg.
- [105] See EPAPS Document No. E-JCPSA6-130-039907 for a full description of the force field. <http://www.aip.org/pubservs/epaps.html>.
- [106] G. D. Smith and W. Paul, "United Atom Force Field for Molecular Dynamics Simulations of 1,4-Polybutadiene Based on Quantum Chemistry Calculations on Model Molecules," *The Journal of Physical Chemistry A*, vol. 102, no. 7, pp. 1200–1208, 1998.
- [107] G. D. Smith, O. Borodin, and D. Bedrov, "Quantum Chemistry Based Force Field for Simulations of Poly(propylene oxide) and Its

-
- Oligomers,” *The Journal of Physical Chemistry A*, vol. 102, no. 50, pp. 10318–10323, 1998.
- [108] O. Borodin and G. D. Smith, “Development of Quantum Chemistry-Based Force Fields for Poly(ethylene oxide) with Many-Body Polarization Interactions,” *The Journal of Physical Chemistry B*, vol. 107, no. 28, pp. 6801–6812, 2003.
- [109] W. Zhao, F. Leroy, S. Balasubramanian, and F. Müller-Plathe, “Shear viscosity of the ionic liquid 1-n-butyl 3-methylimidazolium hexafluorophosphate [bmim][PF6] computed by reverse nonequilibrium molecular dynamics,” *The Journal of Physical Chemistry B*, vol. 112, no. 27, pp. 8129–8133, 2008.
- [110] B. Bhargava and S. Balasubramanian, “Refined potential model for atomistic simulations of ionic liquid [bmim][pf6],” *The Journal of Chemical Physics*, vol. 127, no. 11, p. 114510, 2007.
- [111] J. N. Canongia Lopes, J. Deschamps, and A. A. Pádua, “Modeling ionic liquids using a systematic all-atom force field,” *The Journal of Physical Chemistry B*, vol. 108, no. 6, pp. 2038–2047, 2004.
- [112] O. Borodin, G. D. Smith, and R. L. Jaffe, “Ab initio quantum chemistry and molecular dynamics simulations studies of LiPF6/poly(ethylene oxide) interactions,” *Journal of Computational Chemistry*, vol. 22, no. 6, pp. 641–654, 2001.
- [113] F. Klameth and M. Vogel, “Structure and dynamics of supercooled water in neutral confinements,” *The Journal of Chemical Physics*, vol. 138, p. 134503, 2013.
- [114] H. Berendsen, J. Grigera, and T. Straatsma, “The missing term in effective pair potentials,” *Journal of Physical Chemistry*, vol. 91, no. 24, pp. 6269–6271, 1987.
- [115] M. M. Somoza, M. I. Sluch, and M. A. Berg, “Torsional Relaxation and Friction on the Nanometer Length Scale: Comparison of Small-Molecule Rotation in Poly(dimethylsiloxane) and Poly(isobutylene),” *Macromolecules*, vol. 36, pp. 2721–2732, 2003.
- [116] J. Bandrup and E. H. Immergut, *Polymer Handbook*. John Wiley and Sons, New York, 3rd ed., 1989.
- [117] K. S. C. Agency, “Siloxanes.” http://apps.kemi.se/flodessok/floden/kemamne_Eng/siloxaner_eng.htm, 2011.

-
-
- [118] Common Chemistry, "Polydimethylsiloxane." <http://www.commonchemistry.org/ChemicalDetail.aspx?ref=63148-62-9>, 2014.
- [119] Avogadro open molecule. <http://avogadro.openmolecules.net>, 2011.
- [120] D. C. Company, "CARBOWAX PEGs and MPEGs." <http://www.dow.com/polyglycols/carbowax/index.htm>, 2011.
- [121] G. D. Smith and W. Paul, "Molecular Dynamics of a 1,4-Polybutadiene Melt. Comparison of Experiment and Simulation," *Macromolecules*, vol. 32, pp. 8857–8865, 1999.
- [122] Dr. G. D. Smith's group, "LUCRETIUS Homepage." <http://www.eng.utah.edu/~gsmith/lucretius.html>, 2011.
- [123] N. A. Müller, "Molekularodynamik-Simulationen der ionischen Flüssigkeit 1-Butyl-3methyl-imidazolium-phosphor-hexafluorid (bmim-PF6), TU Darmstadt, Germany," 2013.
- [124] T. Brückel, G. Heger, D. Richter, and R. Zorn, *Neutron Scattering*, vol. 28. Forschungszentrum Jülich, 2005.
- [125] R. J. Composto, E. J. Kramer, and D. M. White, "Fast macromolecules control mutual diffusion in polymer blends," 1987.
- [126] R. Kimmich, F. Klammler, V. Skirda, I. Serebrennikova, A. Maklakov, and N. Fatkullin, "Geometrical restrictions of water diffusion in aqueous protein systems. a study using nmr field-gradient techniques," *Applied Magnetic Resonance*, vol. 4, no. 4, pp. 425–440, 1993.
- [127] M. Rosenstihl and M. Vogel, "Static and pulsed field gradient nuclear magnetic resonance studies of water diffusion in protein matrices," *The Journal of Chemical Physics*, vol. 135, no. 16, pp. –, 2011.
- [128] S.-H. Chen, L. Liu, E. Fratini, P. Baglioni, A. Faraone, and E. Mamonov, "Observation of fragile-to-strong dynamic crossover in protein hydration water," *Proceedings of the National Academy of Sciences*, vol. 103, no. 24, pp. 9012–9016, 2006.
- [129] M. Schwab and B. Stühn, "Relaxation phenomena and development of structure in a physically crosslinked nonionic microemulsion studied by photon correlation spectroscopy and small angle

-
- x-ray scattering,” *The Journal of Chemical Physics*, vol. 112, no. 14, pp. 6461–6471, 2000.
- [130] R. Kimmich, N. Fatkullin, R.-O. Seitter, and K. Gille, “Chain dynamics in entangled polymers: Power laws of the proton and deuteron spin-lattice relaxation dispersions,” *The Journal of Chemical Physics*, vol. 108, no. 5, pp. 2173–2177, 1998.
- [131] M. Kehr, N. Fatkullin, and R. Kimmich, “Molecular diffusion on a time scale between nano- and milliseconds probed by field-cycling NMR relaxometry of intermolecular dipolar interactions: Application to polymer melts,” *The Journal of Chemical Physics*, vol. 126, no. 9, p. 094903, 2007.
- [132] D. Kruk, R. Meier, and E. A. Rössler, “Translational and Rotational Diffusion of Glycerol by Means of Field Cycling ^1H NMR Relaxometry,” *The Journal of Physical Chemistry B*, vol. 115, no. 5, pp. 951–957, 2011.
- [133] D. Kruk, R. Meier, and E. A. Rössler, “Nuclear magnetic resonance relaxometry as a method of measuring translational diffusion coefficients in liquids,” *Physical Review E*, vol. 85, p. 020201, Feb 2012.
- [134] L. Xu, F. Mallamace, Z. Yan, F. W. Starr, S. V. Buldyrev, and H. E. Stanley, “Appearance of a fractional Stokes–Einstein relation in water and a structural interpretation of its onset,” *Nature Physics*, vol. 5, no. 8, pp. 565–569, 2009.
- [135] S. R. Becker, P. H. Poole, and F. W. Starr, “Fractional Stokes-Einstein and Debye-Stokes-Einstein relations in a network-forming liquid,” *Physical Review Letters*, vol. 97, no. 5, p. 055901, 2006.
- [136] F. Mallamace, C. Branca, C. Corsaro, N. Leone, J. Spooren, H. E. Stanley, and S.-H. Chen, “Dynamical Crossover and Breakdown of the Stokes- Einstein Relation in Confined Water and in Methanol-Diluted Bulk Water,” *The Journal of Physical Chemistry B*, vol. 114, no. 5, pp. 1870–1878, 2010.
- [137] A. Turberfield, S. Haynes, P. Wright, R. Ford, R. Clark, J. Ryan, J. Harris, and C. Foxon, “Optical detection of the integer and fractional quantum Hall effects in GaAs,” *Physical Review Letters*, vol. 65, no. 5, pp. 637–640, 1990.

-
- [138] F. Fernandez-Alonso, F. Bermejo, S. McLain, J. Turner, J. Molaison, and K. Herwig, "Observation of fractional Stokes-Einstein behavior in the simplest hydrogen-bonded liquid," *Physical Review Letters*, vol. 98, no. 7, p. 077801, 2007.
- [139] S. H. Lee and T. Chang, "Viscosity and diffusion constants calculation of n-alkanes by molecular dynamics simulations," *Bulletin-Korean Chemical Society*, vol. 24, no. 11, pp. 1590–1598, 2003.
- [140] M. Aichele, Y. Gebremichael, F. W. Starr, J. Baschnagel, and S. C. Glotzer, "Polymer-specific effects of bulk relaxation and stringlike correlated motion in the dynamics of a supercooled polymer melt," *The Journal of Chemical Physics*, vol. 119, no. 10, pp. 5290–5304, 2003.
- [141] C. Donati, S. Franz, S. C. Glotzer, and G. Parisi, "Theory of non-linear susceptibility and correlation length in glasses and liquids," *Journal of Non-Crystalline Solids*, vol. 307-310, pp. 215–224, 2002.
- [142] S. C. Glotzer, V. N. Novikov, and T. B. Schröder, "Time-dependent, four-point density correlation function description of dynamical heterogeneity and decoupling in supercooled liquids," *The Journal of Chemical Physics*, vol. 112, no. 2, pp. 509–512, 2000.
- [143] N. Lačević, F. W. Starr, T. B. Schröder, and S. C. Glotzer, "Spatially heterogeneous dynamics investigated via a time-dependent four-point density correlation function," *The Journal of Chemical Physics*, vol. 119, no. 14, pp. 7372–7387, 2003.
- [144] N. Lačević, F. W. Starr, T. B. Schröder, V. N. Novikov, and S. C. Glotzer, "Growing correlation length on cooling below the onset of caging in a simulated glass-forming liquid," *Physical Review E*, vol. 66, p. 030101, Sep 2002.
- [145] W. Humphrey, A. Dalke, and K. Schulten, "VMD – Visual Molecular Dynamics," *Journal of Molecular Graphics*, vol. 14, pp. 33–38, 1996.
- [146] R. Casalini and C. Roland, "Thermodynamical scaling of the glass transition dynamics," *Physical Review E*, vol. 69, no. 6, p. 062501, 2004.
- [147] C. M. Roland, S. Hensel-Bielowka, M. Paluch, and R. Casalini, "Supercooled dynamics of glass-forming liquids and polymers under hydrostatic pressure," *Reports on Progress in Physics.*, vol. 68, p. 1405, 2005.

-
-
- [148] M. Paluch, S. Pawlus, and C. M. Roland, "Pressure and Temperature Dependence of the α -Relaxation in Poly(methyltolylsiloxane)," *Macromolecules*, vol. 35, no. 19, pp. 7338–7342, 2002.
- [149] M. Paluch, C. M. Roland, and S. Pawlus, "Temperature and pressure dependence of the alpha-relaxation in polymethylphenylsiloxane," *The Journal of Chemical Physics*, vol. 116, no. 24, pp. 10932–10937, 2002.
- [150] A. Tölle, H. Schober, J. Wuttke, O. Randl, and F. Fujara, "Fast relaxation in a fragile liquid under pressure," *Physical Review Letters*, vol. 80, no. 11, p. 2374, 1998.
- [151] C. Dreyfus, A. Aouadi, J. Gapinski, M. Matos-Lopes, W. Steffen, A. Patkowski, and R. Pick, "Temperature and pressure study of Brillouin transverse modes in the organic glass-forming liquid orthoterphenyl," *Physical Review E*, vol. 68, no. 1, p. 011204, 2003.
- [152] R. Casalini, S. Capaccioli, M. Lucchesi, P. A. Rolla, M. Paluch, S. Corezzi, and D. Fioretto, "Effect of pressure on the dynamics of glass formers," *Physical Review E*, vol. 64, p. 041504, Sep 2001.
- [153] E. Rössler, K.-U. Hess, and V. Novikov, "Universal representation of viscosity in glass forming liquids," *Journal of non-crystalline solids*, vol. 223, no. 3, pp. 207–222, 1998.
- [154] Y. S. Elmatad, D. Chandler, and J. P. Garrahan, "Corresponding states of structural glass formers," *The Journal of Physical Chemistry B*, vol. 113, no. 16, pp. 5563–5567, 2009.
- [155] N. B. Olsen, T. Christensen, and J. C. Dyre, "Time-Temperature Superposition in Viscous Liquids," *Physical Review Letters*, vol. 86, pp. 1271–1274, Feb 2001.
- [156] N. P. Bailey, U. R. Pedersen, N. Gnan, T. B. Schrø, and J. C. Dyre, "Pressure-energy correlations in liquids. I. Results from computer simulations," *The Journal of Chemical Physics*, vol. 129, no. 18, p. 184507, 2008.
- [157] N. P. Bailey, U. R. Pedersen, N. Gnan, T. B. Schrø, and J. C. Dyre, "Pressure-energy correlations in liquids. II. Analysis and consequences," *The Journal of Chemical Physics*, vol. 129, no. 18, p. 184508, 2008.

-
- [158] T. B. Schrø, N. P. Bailey, U. R. Pedersen, N. Gnan, and J. C. Dyre, “Pressure-energy correlations in liquids. III. Statistical mechanics and thermodynamics of liquids with hidden scale invariance,” *The Journal of Chemical Physics*, vol. 131, no. 23, p. 234503, 2009.
- [159] N. Gnan, T. B. Schrø, U. R. Pedersen, N. P. Bailey, and J. C. Dyre, “Pressure-energy correlations in liquids. IV. “Isomorphs” in liquid phase diagrams,” *The Journal of Chemical Physics*, vol. 131, no. 23, p. 234504, 2009.
- [160] S. Karmakar, C. Dasgupta, and S. Sastry, “Growing length and time scales in glass-forming liquids,” *Proceedings of the National Academy of Sciences*, vol. 106, no. 10, pp. 3675–3679, 2009.
- [161] S. Sastry, “Liquid limits: Glass transition and liquid-gas spinodal boundaries of metastable liquids,” *Physical Review Letters*, vol. 85, no. 3, p. 590, 2000.
- [162] S. Sastry, “The relationship between fragility, configurational entropy and the potential energy landscape of glass-forming liquids,” *Nature*, vol. 409, no. 6817, pp. 164–167, 2001.
- [163] H. Green, *The Molecular Theory of Fluids*. North-Holland, Amsterdam, 1952.
- [164] F. W. Starr, J. F. Douglas, and S. Sastry, “The relationship of dynamical heterogeneity to the adam-gibbs and random first-order transition theories of glass formation,” *The Journal of chemical physics*, vol. 138, no. 12, p. 12A541, 2013.
- [165] M. T. Cicerone and M. Ediger, “Enhanced translation of probe molecules in supercooled o-terphenyl: Signature of spatially heterogeneous dynamics?,” *The Journal of Chemical Physics*, vol. 104, p. 7210, 1996.
- [166] T. B. Schrøder, *Hopping in disordered media: A model glass former and a hopping model*. PhD thesis, Roskilde University, Denmark, 1999.
- [167] W. Kob and H. C. Andersen, “Testing mode-coupling theory for a supercooled binary Lennard-Jones mixture I: The van Hove correlation function,” *Physical Review E*, vol. 51, no. 5, p. 4626, 1995.

-
- [168] K. Vollmayr-Lee, W. Kob, K. Binder, and A. Zippelius, “Dynamical heterogeneities below the glass transition,” *The Journal of Chemical Physics*, vol. 116, p. 5158, 2002.
- [169] Y. Gebremichael, *Spatially heterogeneous dynamics and string-like correlated motion in supercooled liquids and polymers*. PhD thesis, University of Maryland (College Park, Md.), 2004.
- [170] C. M. Roland, M. Paluch, and R. Casalini, “Effects of the volume and temperature on the global and segmental dynamics in poly(propylene glycol) and 1,4-polyisoprene,” *Journal of Polymer Science Part B: Polymer Physics*, vol. 42, no. 23, pp. 4313–4319, 2004.
- [171] C. Alba-Simionesco, A. Cailliaux, A. Alegría, and G. Tarjus, “Scaling out the density dependence of the $\hat{\lambda}$ relaxation in glass-forming polymers,” *EPL (Europhysics Letters)*, vol. 68, no. 1, p. 58, 2004.
- [172] B. Frick, C. Alba-Simionesco, K. Andersen, and L. Willner, “Influence of density and temperature on the microscopic structure and the segmental relaxation of polybutadiene,” *Physical Review E*, vol. 67, no. 5, p. 051801, 2003.
- [173] M. Vogel, C. Brinkmann, H. Eckert, and A. Heuer, “Silver dynamics in silver iodide/silver phosphate glasses studied by multi-dimensional ^{109}Ag nmr,” *Phys. Chem. Chem. Phys.*, vol. 4, pp. 3237–3245, 2002.
- [174] M. Aichele, *Simulation studies of correlation functions and relaxation in polymeric systems*. PhD thesis, Johannes Gutenberg Universität, Mainz, 2003.
- [175] M. Aichele, Y. Gebremichael, F. Starr, J. Baschnagel, and S. Glotzer, “Stringlike correlated motion in the dynamics of supercooled polymer melts,” *Journal of Chemical Physics*, vol. 119, pp. 5290–5304, 2003.
- [176] Next bead neighbor in FENE $q=7.15$, the SE exponent was extracted via a numerical evaluation of the in above Refs. given scalings $D^{-1} \propto ((T - T_c)/T)^{1.84}$ and $\tau \propto ((T - T_c)/T)^{-2.08}$.
- [177] L. Berthier, “Dynamic heterogeneity in amorphous materials,” *Physics*, vol. 4, p. 42, 2011.

-
-
- [178] E. Flenner and G. Szamel, “Dynamic heterogeneities above and below the mode-coupling temperature: Evidence of a dynamic crossover,” *The Journal of Chemical Physics*, vol. 138, p. 12A523, 2013.
- [179] M. Alcoutlabi and G. B. McKenna, “Effects of confinement on material behaviour at the nanometre size scale,” *Journal of Physics: Condensed Matter*, vol. 17, no. 15, p. R461, 2005.
- [180] R. Richert, “Dynamics of nanoconfined supercooled liquids,” *Annual review of physical chemistry*, vol. 62, pp. 65–84, 2011.
- [181] K. Watanabe, T. Kawasaki, and H. Tanaka, “Structural origin of enhanced slow dynamics near a wall in glass-forming systems,” *Nature materials*, vol. 10, no. 7, pp. 512–520, 2011.
- [182] A. Cavagna, T. S. Grigera, and P. Verrocchio, “Dynamic relaxation of a liquid cavity under amorphous boundary conditions,” *The Journal of Chemical Physics*, vol. 136, p. 204502, 2012.
- [183] G. Szamel and E. Flenner, “Glassy dynamics of partially pinned fluids: An alternative mode-coupling approach,” *EPL (Europhysics Letters)*, vol. 101, no. 6, p. 66005, 2013.
- [184] C. Cammarota and G. Biroli, “Ideal glass transitions by random pinning,” *Proceedings of the National Academy of Sciences*, vol. 109, no. 23, pp. 8850–8855, 2012.
- [185] C. Cammarota, G. Gradenigo, and G. Biroli, “Confinement as a Tool to Probe Amorphous Order,” *Physical Review Letters*, vol. 111, p. 107801, Sep 2013.
- [186] P. Scheidler, W. Kob, and K. Binder, “The relaxation dynamics of a simple glass former confined in a pore,” *EPL (Europhysics Letters)*, vol. 52, no. 3, p. 277, 2000.
- [187] P. Scheidler, W. Kob, and K. Binder, “Cooperative motion and growing length scales in supercooled confined liquids,” *EPL (Europhysics Letters)*, vol. 59, no. 5, p. 701, 2002.
- [188] P. Scheidler, W. Kob, and K. Binder, “The relaxation dynamics of a confined glassy simple liquid,” *The European Physical Journal E*, vol. 12, no. 1, pp. 5–9, 2003.

-
-
- [189] P. Scheidler, W. Kob, and K. Binder, "The relaxation dynamics of a supercooled liquid confined by rough walls," *The Journal of Physical Chemistry B*, vol. 108, no. 21, pp. 6673–6686, 2004.
- [190] R. L. Jack and C. J. Fullerton, "Dynamical correlations in a glass former with randomly pinned particles," *Physical Review E*, vol. 88, no. 4, p. 042304, 2013.
- [191] A. Abragam, *The Principles of Nuclear Magnetism*. Oxford at the Clarendon Press, 1961.
- [192] M. Odelius, A. Laaksonen, M. Levitt, and J. Kowalewski, "Intermolecular Dipole-Dipole Relaxation. A Molecular Dynamics Simulation," *Journal of Magnetic Resonance, Series A*, vol. 105, no. 3, pp. 289–294, 1993.
- [193] N. Bloembergen, E. M. Purcell, and R. V. Pound, "Relaxation Effects in Nuclear Magnetic Resonance Absorption," *Phys. Rev.*, vol. 73, pp. 679–712, Apr 1948.
- [194] C. Gainaru and R. Böhmer, "Oligomer-to-Polymer Transition of Poly(propylene glycol) Revealed by Dielectric Normal Modes," *Macromolecules*, vol. 42, no. 20, pp. 7616–7618, 2009.
- [195] R. Kimmich and E. Anzardo *Progress in Nuclear Magnetic Resonance Spectroscopy*, vol. 44, p. 257, 2007.
- [196] L. P. Hwang and J. H. Freed, "Dynamic effects of pair correlation functions on spin relaxation by translational diffusion in liquids," *The Journal of Chemical Physics*, vol. 63, no. 9, pp. 4017–4025, 1975.
- [197] K. Schmidt-Rohr and H. Spiess, *Multidimensional Solid-State NMR and Polymers*. Academic Press, London, 1994.
- [198] S. Kariyo, C. Gainaru, H. Schick, A. Brodin, V. N. Novikov, and E. A. Rössler, "From a Simple Liquid to a Polymer Melt: NMR Relaxometry Study of Polybutadiene," *Physical Review Letters*, vol. 97, p. 207803, Nov 2006.
- [199] A. Herrmann, V. N. Novikov, and E. A. Rössler, "Dipolar and Bond Vector Correlation Function of Linear Polymers Revealed by Field Cycling ¹H NMR: Crossover from Rouse to Entanglement Regime," *Macromolecules*, vol. 42, no. 6, pp. 2063–2068, 2009.

-
-
- [200] R. Böhmer, G. Diezemann, G. Hinze, and E. Rössler, "Dynamics of supercooled liquids and glassy solids," *Progress in Nuclear Magnetic Resonance Spectroscopy*, vol. 39, no. 3, pp. 191–267, 2001.
- [201] C. P. Lindsey and G. D. Patterson, "Detailed comparison of the Williams–Watts and Cole–Davidson functions," *The Journal of Chemical Physics*, vol. 73, no. 7, pp. 3348–3357, 1980.
- [202] M. Vogel and T. Torbrugge, "Ion and polymer dynamics in polymer electrolytes PPO-LiClO₄. I. Insights from NMR line-shape analysis," *The Journal of Chemical Physics*, vol. 125, no. 5, p. 054905, 2006.
- [203] M. Vogel and T. Torbrugge, "Ion and polymer dynamics in polymer electrolytes PPO-LiClO₄. II. ²H and ⁷Li NMR stimulated-echo experiments," *The Journal of Chemical Physics*, vol. 125, no. 16, p. 164910, 2006.
- [204] M. Vogel and T. Torbrugge, "Nonexponential polymer segmental motion in the presence and absence of ions: ²H NMR multi-time correlation functions for polymer electrolytes poly(propylene glycol)-LiClO₄," *The Journal of Chemical Physics*, vol. 126, no. 20, p. 204902, 2007.
- [205] S. Kariyo, A. Herrmann, C. Gainaru, H. Schick, A. Brodin, V. N. Novikov, and E. A. Rössler, "Erratum: From a Simple Liquid to a Polymer Melt: NMR Relaxometry Study of Polybutadiene [Physical Review Letters 97, 207803 (2006)]," *Physical Review Letters*, vol. 100, p. 109901, Mar 2008.
- [206] G. Smith, W. Paul, M. Monkenbusch, and D. Richter, "A comparison of neutron scattering studies and computer simulations of polymer melts," *Chemical Physics*, vol. 261, no. 1, pp. 61–74, 2000.
- [207] A. Abou Elfadl, R. Kahlau, A. Herrmann, V. Novikov, and E. Rössler, "From rouse to fully established entanglement dynamics: a study of polyisoprene by dielectric spectroscopy," *Macromolecules*, vol. 43, no. 7, pp. 3340–3351, 2010.

List of Abbreviations

| | |
|------------------|---|
| MD | molecular dynamics |
| PPO | poly(propyleneoxide) |
| PPG | poly(propyleneglycol) |
| PEO | poly(ethyleneoxide) |
| IL | ionic liquid |
| bmimPF6 | 1-Butyl-3-methylimidazolium hexafluorophosphate |
| KWW | Kohlrausch-Williams-Watts |
| MSD | mean-squared displacement |
| FWHM | full width at half maximum |
| SE | Stokes-Einstein |
| PME | Particle-Mesh Ewald |
| GROMACS | Groningen Machine for Chemical Simulations |
| LJ | Lennard-Jones |
| HS | hard sphere |
| BK | Buckingham |
| EA | Explicit-Atom |
| UA | United-Atom |
| NMR | nuclear magnetic resonance |
| SLR | spin-lattice relaxation |
| CD | Cole-Davidson |
| BPP model | Bloembergen-Purcell-Pound model [193] |
| DD | dipole-dipole |
| QP | quadrupolar |
| RACF | rotational auto-correlation function |
| SD | spectral density |
| FC | field-cycling |
| SFG | static-field gradient |
| PFG | pulsed-field gradient |
| NS | neutron scattering |

| | |
|-------------|----------------------------------|
| QENS | quasi-elastic neutron scattering |
| PCS | photon-correlation spectroscopy |
| TTS | time-temperature superposition |
| BPP | Bloembergen-Purcell-Pound |
| VFT | Vogel-Fulcher-Tammann |
| MCT | Mode-Coupling Theory |
| AG | Adam-Gibbs |
| RFOT | Random First Order Transition |
| DF | Dynamic Facilitation |
| SHD | spatially heterogeneous dynamics |
| FA | Frederickson-Anderson |
| DS | Dielectric Spectroscopy |
| CRR | cooperatively rearranging region |
| PES | potential energy surface |

List of Symbols

| | |
|-------------------------|--|
| $F_s(q, t)$ | incoherent scattering function |
| $S(q, t)$ | coherent scattering function |
| τ_α | structural α -relaxation time defined via $F_s(q, t)$ |
| β | stretching parameter of $F_s(q, t)$ |
| D | diffusion coefficient |
| N | chain-length of a polymer measured in monomers |
| j | index variable |
| k | index variable |
| $\langle \dots \rangle$ | indicator for the ensemble average |
| T_K | Kauzmann temperature |
| $\alpha_2(t)$ | non-Gaussian parameter |
| τ_{α_2} | characteristic time of the non-Gaussian parameter ($\alpha_2(t)$) peak |
| $\alpha_{2,max}$ | maximum value of the $\alpha_2(t)$ peak |
| $\chi_4(t)$ | 4-point density correlation function |
| τ_{χ_4} | characteristic time of the 4-point density correlation function ($\chi_4(t)$) peak |
| $\chi_{4,max}$ | maximum value of the $\chi_4(t)$ peak |
| $S_w(t)$ | weight-averaged dynamic cluster size |
| τ_S | characteristic time of the weight-averaged dynamic cluster size ($S_w(t)$) peak |
| $S_{w,max}$ | maximum value of the $S_w(t)$ peak |
| $L_w(t)$ | weight-averaged dynamic string length |
| τ_L | characteristic time of the weight-averaged dynamic string length ($L_w(t)$) peak |
| $L_{w,max}$ | maximum value of the $L_w(t)$ peak |
| $p_s(n, t)$ | probability distribution to finding a cluster of size n at time t |

| | |
|----------------------|--|
| $p_l(n, t)$ | probability distribution to finding a string of length n at time t |
| S_{conf} | configuration entropy |
| ρ | particle density |
| ξ_{SE} | fractional Stokes-Einstein exponent |
| $F_c(t)$ | indicator for significant contribution of dynamic facilitation |
| τ_F | characteristic peak time of $F_c(t)$ of enhanced mobility transfer within DF |
| ξ_d | dynamic correlation length |
| ξ_s | static correlation length |
| ξ_{SHD} | SHD correlation length from FWHM(α_2) long-time plateau of the overlap correlation $Q(t)$ |
| ^1H | proton |
| ^2H | deuteron |
| $1/T_1$ | spin-lattice relaxation (SLR) rate |
| $C(t)$ | any basic correlation function in time |
| I | nuclear spin |
| γ_G | gyromagnetic ratio |
| $\mathbf{r}_{jk}(t)$ | connection vector between atom j and atom k |
| Y_{lm} | normalized spherical harmonics |
| $G^{(m)}(t)$ | random functions |
| $J^{(m)}(\omega)$ | spectral density of $G^{(m)}(t)$ |
| τ_R | relaxation time of the longest Rouse mode |
| $G(t)$ | ^1H - ^1H correlation function $G^{(0)}(t)$ |
| $J(\omega)$ | spectral density (SD) |
| G_{inter} | intermolecular contribution to the ^1H - ^1H correlation function |
| G_{intra} | intramolecular contribution to the ^1H - ^1H correlation function |

| | |
|------------------------------------|---|
| J_{intra} | intramolecular contribution to the ^1H - ^1H spectral density |
| J_{inter} | intermolecular contribution to the ^1H - ^1H spectral density |
| N_E | entanglement length of a polymer in no. of monomers |
| τ_T | translation relaxation time in the hard sphere model [196] |
| N_H | spin number density |
| $\langle r^2(t) \rangle$ | mean-squared displacement (MSD) |
| $\langle r_H^2(t) \rangle$ | mean-squared displacement (MSD) for protons only |
| $G_0(\vec{r}_i(t) - \vec{r}_i(0))$ | distribution of bead displacements |
| Q | nuclear electric quadrupole moment |
| $P_2(x)$ | 2. Legendre polynomial, or Y_{lm} with $m=0, l=2$ |
| $J_2(\omega)$ | spectral density of deuteron (^2H) nuclear magnetic resonance (NMR) |
| T_1 | spin-lattice relaxation times |
| ω_L | Lamor frequency of the SLR |



Date and Place of Birth

13.04.1985 Frankfurt am Main

University Education

May 2011 - June 2014 Doctorate Physics
(TU Darmstadt)

March 2011 - June 2014 B.Sc. Industrial
Engineering
(TU Darmstadt)

May 2009 - April 2011 M.Sc. Engineering Physics
(TU Darmstadt)

April 2006 - January 2009 B.Sc. Physics
(TU Darmstadt)

Military Service

July 2005 - March 2006 Bundeswehr

School Education

2005 Abitur
1996-2005 Christian-Wirth-Schule, Usingen



List of Publications

- [1] A. Bormuth, P. Henritzi, and M. Vogel. “Chain-length dependence of the segmental relaxation in polymer melts: Molecular dynamics simulation studies on poly(propylene oxide).” *Macromolecules*, 43 (21):8985–8992, 2010.
- [2] P. Henritzi, A. Bormuth, and M. Vogel. “Interpretation of ^1H and ^2H spin-lattice relaxation dispersions: Insights from molecular dynamics simulations of polymer melts.” *Solid State Nuclear Magnetic Resonance*, 54(0):32 – 40, 2013.
- [3] A. Bormuth, M. Hofmann, P. Henritzi, M. Vogel, and E. A. Rössler. “Chain-length dependence of polymer dynamics: A comparison of results from molecular dynamics simulations and field-cycling ^1H nmr.” *Macromolecules*, 46(19):7805–7811, 2013.
- [4] F. Klameth, P. Henritzi, and M. Vogel, “Static and dynamic length scales in supercooled liquids: Insights from molecular dynamics simulations of water and tri-propylene oxide,” *The Journal of Chemical Physics*, vol. 140, no. 14, 2014.
- [5] P. Henritzi, D. Bedrov, G. Smith, and M. Vogel, “Influence of pressure on deviations of chain dynamics from the Rouse model: A molecular dynamics simulation study of poly(dimethylsiloxane) and polybutadiene melts.” Poster session presented at: CPP 23.8: Poster, DPG Frühjahrstagung 2012 28. March 2012 Berlin, Germany
- [6] P. Henritzi, and M. Vogel, “A molecular dynamics simulation study on pressure-temperature scaling of polymer segmental motion.” Poster session presented at: 6th International Conference on Times of Polymers (Top) and Composites, June 2012 Ischia, Italy
- [7] P. Henritzi, A. Bormuth and M. Vogel, “Dynamics in Polymeric Systems: A Molecular Dynamics Simulation Study.” Oral presentation at: 18th AK-Treffen der NMR Gruppen Burg Hohenberg 2013, 18. March 2013, Hohenberg, Germany
- [8] P. Henritzi, M. Rosenstihl and M. Vogel, “Berechnung von ^1H und ^2H Spin-Gitter-Relaxationszeiten aus Molekulardynamiksimulationen von Polymeren verschiedener Kettenlänge.” Oral presentation at 14th

AK-Treffen der NMR Gruppen Heidelberg 2009, 6. March 2009, Heidelberg, Germany

Danksagung

Zunächst geht mein Dank an Alle, die mich in den vergangenen acht Jahren an der TU Darmstadt, sei es im Studium, privat oder bei der Promotion, begleitet haben.

Im speziellen bedanke ich mich bei Michael Vogel für die schöne Zeit vom Bachelor bis hin zur Promotion. Wer hätte gedacht, dass aus einem dreimonatigen Engagement fünf Jahre werden. Vielen Dank auch an Bernd Stühn für die Übernahme der Zweitkorrektur.

Für eine produktive und zuweilen lustige Atmosphäre danke ich André Bor-muth, Felix Klameth and Patrick Wieth, die mir einige theoretische Überlegungen nahe gebracht haben und mich in die Geheimnisse des frühen Mittagstisches eingeweiht haben.

Ein grosses Dankeschön geht auch an Markus Rosenstihl für seine nicht enden wollende Hilfsbereitschaft bei IT Problemen.

Für offene Türen und Ohren zu jeder Zeit danke ich meiner Familie und meinen Freunden, die mich abseits des Büros immer auf andere Ideen gebracht haben.

Mein ganz spezieller Dank geht an meine Freundin, die den gemeinsamen Stress immer wunderbar mit ausgehalten hat und bei Urlauben nicht auf ihre Kosten kam. Diesen Sommer klappt's!